UNIVERSITAT POLITÈCNICA DE CATALUNYA

Hydrogen production from bioethanol using cobalt hydrotalcites

Doctoral Thesis

Raúl Uziel Espinal Bustos

Universitat Politècnica de Catalunya

BarcelonaTECH

Institut de Tècniques Energètiques

Hydrogen production from bioethanol using cobalt hydrotalcites

Presented by

Raúl Uziel Espinal Bustos

In order to obtain the Doctor degree from the Technical University of Catalonia, BarcelonaTECH.

Supervised by

Dr. Jordi Llorca Piqué

Acknowledgments

First of all I want to thank my advisor Jordi Llorca, who has taught me a lot and always been there for me with patience and a helpful piece of advice. Elena Taboada also shared a lot of tips, knowledge and ideas, thank you so much. I really appreciate your time and dedication, learnt a lot from both of you.

Thanks to CONACYT México for the scholarship.

The laboratories I got to work at, Institut de Tècniques Energètiques (INTE) and Centre de Recerca en Nanoenginyeria (CRNE), all the staff, thanks to all of you for your continuous support and shared moments over the course of my PhD.

To my family, friends and girlfriend, for believing in me and supporting me all this time.

Summary

Hydrogen constitutes a promising alternative to manage our energy supply more efficiently. Hydrogen can be stored and used in fuel cells to produce electricity, where it combines with the oxygen present in the air and generates solely water as by-product. Of the different methods available to produce hydrogen, the catalytic reaction of ethanol and water (reforming) is one of the most advantageous alternatives, since ethanol can be produced easily from biomass (bioethanol), is liquid and simple to manipulate. This doctoral thesis studies the behavior of a family of cobalt catalysts to produce hydrogen from ethanol and water; to be more precise, catalysts based on cobalt hydrotalcites. The same process could be triggered by other types of catalyst, but many of them are far more expensive due to the noble metals they contain, and others - those based on nickel and cobalt - desactivate after a short amount of time because their surface accumulate carbon. This thesis demonstrates that with the help of a precise method of preparation, one can create inexpensive catalysts from cobalt hydrotalcites, which remain quite stable under realistic operating conditions.

Chapter 1 introduces the reader to the key aspects of this doctoral thesis. It explains the objectives pursued and gives an overview of the state of art and the groundwork on which the experimental work is based. Besides explaining the general characteristics of the catalysts and the reactions that will be studied, chapter 1 also informs about cordierite monoliths: what exactly are they and why are they used in this work to physically stabilize the catalysts and catalytic membrane reactors. In this way, the aim of this doctoral thesis is to acquire new scientific knowledge on the one hand and on the other, to apply this knowledge in the development of devices that can be applied in practice.

The four chapters following thereafter form a compound of papers that have been published in notable international journals (three of them) and one article in process of revision.

Chapter 2 describes the preparation of a family of cobalt hydrotalcites with different ratios of cobalt, magnesia and aluminum, and how these cobalt hydrotalcites behave

in the ethanol steam reforming reaction to produce hydrogen. Starting from a detailed characterization using different techniques like TEM, XRD, IR, TGA, In situ XPS, magnetism, etc., the different chemical elements present are identified, and their structure in the catalysts before, during, and after reaction is analyzed. It becomes evident that the best formula (with the greatest yield of hydrogen and the least amount of coke residual) is a hydrotalcite with a relation of Co:Mg:Al=1:2:1. It is concluded that during the reaction, the hydrotalcite-based catalyst transforms itself to a mix of cobalt spinel, strongly interacting with MgO on a nanometric scale. Nevertheless, if the reaction is repeated using only cobalt spinel (synthesized specifically for this purpose), the outcome is a smaller amount of hydrogen. This shows that cobalt hydrotalcite used as a catalyst precursor plays a crucial part in the final structure of the catalyst.

Hydrotalcite Co:Mg:Al=1:2:1 doped with Pt and Rh is studied in chapter 3. For this, two families of catalysts with different ratios of Pt and Rh were prepared. They were analyzed under the same conditions as explained in chapter 2 and were tested in the reaction. The objective of doping the cobalt hydrotalcite with noble metals was to facilitate the reaction of cobalt, given the fact that metallic cobalt is the active element in ethanol steam reforming. Besides this key function of metallic cobalt, chapter 2 also reveals, however, that metallic cobalt speeds up the catalyst deactivation by causing severe coke accumulation. On the other hand, under the same reaction conditions as in the spinel experiment, Co(II) also serves as an active species in the reforming, differentiating itself by the fact that it leads to hardly any coke accumulation. In absence of noble metals, Co(II) remains unaltered and the catalyst is very stable; once Pt or Rh are present, Co(II) reduces to cobalt metal and the catalyst gets deactivated due to accumulation of coke.

Chapter 4 studies the effects of adding alkaline additives, specifically K^+. Ethanol can be dehydrated in the acid centers of the catalysts to form ethylene, which triggers coke accumulation. Hydrotalcites Co:Mg:Al=1:2:1 with different K^+ ratios were synthesized and characterized with the techniques previously mentioned, and additionally with NH_3 TPD tests. They were then tested in the ethanol reforming and also directly using commercial bioethanol. The experiments showed that the best catalyst was the one

with a percentage of 1% of K^+ in relation to Co. It showed stable behavior during more than 300 hours of experiments. The same catalyst was used to study the oxidative ethanol steam reforming for greater energetic efficiency of the process.

As it is found that hydrotalcite Co:Mg:Al=1:2:1 with 1% of K^+ showed the best results, in chapter 5 it is applied in a membrane reactor. For this, a commercial membrane of Pd-Ag was used in the same ethanol steam reforming conditions, varying temperature, pressure, ethanol-water ratio and the catalyst loads. The influence of the catalyst position inside the membrane reactor was also studied (staged membrane reactor and fixed bed reactor). It is concluded that the catalyst is suitable to be used in a catalytic membrane reactor working under pressure and without nitrogen sweep gas in order to obtain a pure flow of hydrogen which can be used to directly feed a low temperature fuel cell. In addition to the separation of the hydrogen by the membrane, the net production of hydrogen in the catalytic membrane reactor is clearly higher whenever equilibrium displacement takes place.

Resum

L'hidrogen es perfila com un vector energètic que pot ajudar-nos a gestionar l'energia d'una manera més eficient. L'hidrogen es pot emmagatzemar i utilitzar per produir electricitat a les piles de combustible, en què es combina amb l'oxigen de l' aire i genera únicament aigua com a subproducte. De les diferents maneres que existeixen per produir hidrogen, la reacció catalítica entre l'etanol i l'aigua (reformat) constitueix una de les millors opcions, ja que l'etanol es produeix fàcilment a partir de la biomassa (bioetanol) i és un substrat líquid i fàcilment manipulable. En aquesta tesi doctoral s'ha estudiat el comportament d'una família de catalitzadors de cobalt per dur a terme la producció d'hidrogen a partir d'etanol i aigua, concretament catalitzadors basats en hidrotalcites de cobalt. Hi ha altres catalitzadors per dur a terme aquest mateix procés, però molts d'ells tenen un cost elevat perquè contenen metalls nobles i altres es desactiven amb facilitat per deposició de carbó en la seva superfície (els basats en níquel i cobalt). En aquesta tesi es demostra que mitjançant un mètode precís de preparació a partir d' hidrotalcites de cobalt s'aconsegueixen catalitzadors de baix cost i molt estables sota condicions reals d'operació.

El capítol 1 és una introducció als aspectes més destacables de la tesi doctoral, en què es plantegen els objectius que es volen abordar i s'inclouen l' estat de l'art i els fonaments en què es basa el treball experimental realitzat. A més de la naturalesa dels catalitzadors i de les reaccions que es van a estudiar, en la introducció també s'explica què són i per què s'utilitzen en aquesta tesi monòlits de cordierita com suports físics dels catalitzadors i reactors catalítics de membrana. I és que aquesta tesi doctoral persegueix, d'una banda, l'adquisició de nou coneixement científic i, d'altra banda, l'aplicació d'aquest coneixement en el desenvolupament de dispositius útils en aplicacions reals.

En els capítols següents, la tesi doctoral constitueix un compendi d'articles publicats en revistes internacionals de prestigi (3 articles publicats i 1 article en procés de revisió).

En el capítol 2 es descriu la preparació d'una família de hidrotalcites de cobalt amb diferent contingut de cobalt, magnesi i alumini i el seu comportament catalític en la reacció de reformat d'etanol amb vapor per a la producció d'hidrogen. A partir d'una

caracterització detallada mitjançant diferents tècniques instrumentals, entre les que s'inclouen la microscòpia electrònica de rastreig, microscòpia electrònica de transmissió, difracció de raigs X, mesures de magnetisme a temperatura variable, espectroscòpia infraroja, anàlisis termogravimètriques, i experiments in-situ amb espectroscòpia fotoelectrònica de raigs X, s'identifiquen les espècies químiques presents i la seva estructura en els catalitzadors abans, durant, i després de la reacció, posant de manifest que la millor formulació (la que ofereix un rendiment a hidrogen més elevat i sobre la qual amb prou feines es dipositen residus carbonosos) correspon a una hidrotalcita amb una relació Co:Mg:Al de 1:2:1. Així mateix es conclou que el catalitzador preparat a partir d'aquesta hidrotalcita es transforma a una barreja de espinel de cobalt interaccionant fortament amb MgO a escala nanomètrica sota les condicions de reacció. No obstant això, en realitzar la reacció exclusivament amb l'espinela de cobalt (preparada per separat a aquest efecte) s'obté una producció d'hidrogen menor, cosa que demostra que la hidrotalcita de cobalt usada com a precursor del catalitzador exerceix un control decisiu en l'estructura del mateix .

En el capítol 3 s'estudia la influència del dopatge de la hidrotalcita Co: Mg : Al = 1:2:1 amb Pt i Rh. Per a això s'han preparat dues famílies de catalitzadors amb diferent contingut de Pt i Rh, s'han caracteritzat de manera similar al capítol anterior i s'han provat en la reacció. La intenció de dopar la hidrotalcita de cobalt amb metalls nobles ha estat la de facilitar la reducció del cobalt, ja que està descrit que el cobalt metall és l'espècie activa en el reformat d'etanol amb vapor. No obstant això, en aquest capítol de la tesi s'ha posat clarament de manifest que, tot i que el cobalt metall és una espècie activa en la reacció, també és la responsable de la ràpida desactivació del catalitzador per acumulació severa de carbó. En canvi , el Co (II) , en l'entorn definit per la transformació de la hidrotalcita a una barreja de espinela de cobalt i MgO sota les condicions de reacció, és una espècie també activa en el reformat sobre la qual no es dipositen gairebé residus carbonosos. En absència de metalls nobles, el Co (II) es manté inalterat i el catalitzador és molt estable, en canvi, en presència de Pt o Rh el Co (II) es redueix a Co metall i el catalitzador es desactiva per acumulació de carbó.

En el capítol 4 s'estudia l'efecte de l'addició d'un additiu alcalí, concretament K^+. Se sap que l'etanol pot deshidratar en els centres àcids dels catalitzadors donant lloc a etilè,

que fàcilment origina residus carbonosos. S'han preparat hidrotalcites Co:Mg:Al=1:2:1 amb diferent contingut de K^+, s'han caracteritzat (a més de les tècniques utilitzades en els capítols anteriors també s'ha determinat l'acidesa mitjançant desorció tèrmica programada de NH_3) i s'han provat en el reformat d'etanol amb vapor i també directament en el reformat de bioetanol comercial. S'ha trobat que el catalitzador òptim és aquell que conté al voltant d'un 1% de K^+ respecte al Co. Aquest catalitzador s'ha mostrat totalment estable en les proves realitzades durant més de 300 h. Aquest mateix catalitzador s'ha emprat per estudiar el reformat oxidatiu d'etanol amb vapor per tal de millorar l'eficiència energètica del procés.

En el capítol 5 s'ha utilitzat el millor catalitzador trobat, és a dir el catalitzador preparat a partir de la hidrotalcita Co: Mg : Al = 1:2:1 amb 1% K^+, en un reactor catalític de membrana. S'ha utilitzat una membrana comercial de Pd - Ag i s'ha estudiat el procés variant la temperatura, pressió, relació etanol : aigua i càrrega de reactius. També s'ha estudiat la influència de la geometria entre el catalitzador i la membrana (membrana en sèrie vs. membrana integrada al llit del catalitzador). Es dedueix que el catalitzador és apte per a ser usat en un reactor catalític de membrana operant a pressió i sense gas de rastreig per obtenir un corrent pur d'hidrogen que pot ser utilitzada per alimentar directament una pila de combustible de baixa temperatura. A més de la separació de l'hidrogen per la membrana, la producció neta d'hidrogen al reactor catalític de membrana és clarament superior pel desplaçament de la reacció.

Resumen

El hidrógeno se perfila como un vector energético que puede ayudarnos a gestionar la energía de una manera más eficiente. El hidrógeno se puede almacenar y usar para producir electricidad en las pilas de combustible, en las que se combina con el oxígeno del aire y genera únicamente agua como subproducto. De las distintas maneras que existen para producir hidrógeno, la reacción catalítica entre el etanol y el agua (reformado) constituye una de las mejores opciones, ya que el etanol se produce fácilmente a partir de la biomasa (bioetanol) y es un substrato líquido y fácilmente manipulable. En esta tesis doctoral se ha estudiado el comportamiento de una familia de catalizadores de cobalto para llevar a cabo la producción de hidrógeno a partir de etanol y agua; concretamente, catalizadores basados en hidrotalcitas de cobalto. Existen otros catalizadores para llevar a cabo este mismo proceso, pero muchos de ellos tienen un coste elevado porque contienen metales nobles y otros se desactivan con facilidad por deposición de carbón en su superficie (los basados en níquel y cobalto). En esta tesis se demuestra que mediante un método preciso de preparación a partir de hidrotalcitas de cobalto se consiguen catalizadores de bajo coste y muy estables bajo condiciones reales de operación.

El capítulo 1 es una introducción a los aspectos más destacables de la tesis doctoral, en el que se plantean los objetivos que se quieren abordar y se incluyen el estado del arte y los fundamentos en los que se basa el trabajo experimental realizado. Además de la naturaleza de los catalizadores y de las reacciones que se van a estudiar, en la introducción también se explica qué son y por qué se utilizan en esta tesis monolitos de cordierita como soportes físicos de los catalizadores y reactores catalíticos de membrana. Y es que esta tesis doctoral persigue, por un lado, la adquisición de nuevo conocimiento científico y, por otro lado, la aplicación de este conocimiento en el desarrollo de dispositivos útiles en aplicaciones reales.

En los capítulos siguientes, la tesis doctoral constituye un compendio de artículos publicados en revistas internacionales de prestigio (3 artículos publicados y 1 artículo en proceso de revisión).

En el capítulo 2 se describe la preparación de una familia de hidrotalcitas de cobalto con distinto contenido de cobalto, magnesio y aluminio y su comportamiento catalítico en la reacción de reformado de etanol con vapor para la producción de hidrógeno. A partir de una caracterización pormenorizada mediante distintas técnicas instrumentales, entre las que se incluyen la microscopía electrónica de barrido, microscopía electrónica de transmisión, difracción de rayos X, medidas de magnetismo a temperatura variable, espectroscopia infrarroja, análisis termogravimétricos, y experimentos in-situ con espectroscopía fotoelectrónica de rayos X, se identifican las especies químicas presentes y su estructura en los catalizadores antes, durante, y después de la reacción, poniéndose de manifiesto que la mejor formulación (la que ofrece un rendimiento a hidrógeno más elevado y sobre la que apenas se depositan residuos carbonosos) corresponde a una hidrotalcita con una relación Co:Mg:Al de 1:2:1. Asimismo se concluye que el catalizador preparado a partir de esta hidrotalcita se transforma a una mezcla de espinela de cobalto interaccionando fuertemente con MgO a escala nanométrica bajo las condiciones de reacción. Sin embargo, al realizar la reacción exclusivamente con la espinela de cobalto (preparada por separado a tal efecto) se obtiene una producción de hidrógeno menor, lo que demuestra que la hidrotalcita de cobalto usada como precursor del catalizador ejerce un control decisivo en la estructura del mismo.

En el capítulo 3 se estudia la influencia del dopaje de la hidrotalcita Co:Mg:Al=1:2:1 con Pt y Rh. Para ello se han preparado dos familias de catalizadores con distinto contenido de Pt y Rh, se han caracterizado de manera similar al capítulo anterior y se han probado en la reacción. La intención de dopar la hidrotalcita de cobalto con metales nobles ha sido la de facilitar la reducción del cobalto, puesto que está descrito que el cobalto metal es la especie activa en el reformado de etanol con vapor. Sin embargo, en este capítulo de la tesis se ha puesto claramente de manifiesto que, a pesar que el cobalto metal es una especie activa en la reacción, también es la responsable de la rápida desactivación del catalizador por acumulación severa de carbón. En cambio, el Co(II), en el entorno definido por la transformación de la hidrotalcita a una mezcla de espinela de cobalto y MgO bajo las condiciones de reacción, es una especie también activa en el reformado sobre la que no se depositan

apenas residuos carbonosos. En ausencia de metales nobles, el Co(II) se mantiene inalterado y el catalizador es muy estable; en cambio, en presencia de Pt o Rh el Co(II) se reduce a Co metal y el catalizador se desactiva por acumulación de carbón.

En el capítulo 4 se estudia el efecto de la adición de un aditivo alcalino, concretamente K^+. Se sabe que el etanol puede deshidratarse en los centros ácidos de los catalizadores dando lugar a etileno, que fácilmente origina residuos carbonosos. Se han preparado hidrotalcitas Co:Mg:Al=1:2:1 con distinto contenido de K^+, se han caracterizado (además de las técnicas utilizadas en los capítulos anteriores también se ha determinado la acidez mediante desorción térmica programada de NH_3) y se han probado en el reformado de etanol con vapor y también directamente en el reformado de bioetanol comercial. Se ha encontrado que el catalizador óptimo es aquel que contiene alrededor de un 1% de K^+ con respecto al Co. Este catalizador se ha mostrado totalmente estable en las pruebas realizadas durante más de 300 h. Este mismo catalizador se ha empleado para estudiar el reformado oxidativo de etanol con vapor con el fin de mejorar la eficiencia energética del proceso.

En el capítulo 5 se ha utilizado el mejor catalizador encontrado, es decir el catalizador preparado a partir de la hidrotalcita Co:Mg:Al=1:2:1 con 1% K^+, en un reactor catalítico de membrana. Se ha utilizado una membrana comercial de Pd-Ag y se ha estudiado el proceso variando la temperatura, presión, relación etanol:agua y carga de reactivos. También se ha estudiado la influencia de la geometría entre el catalizador y la membrana (membrana en serie vs. membrana integrada en el lecho del catalizador). Se deduce que el catalizador es apto para ser usado en un reactor catalítico de membrana operando a presión y sin gas de barrido para obtener una corriente pura de hidrógeno que puede ser utilizada para alimentar directamente una pila de combustible de baja temperatura. Además de la separación del hidrógeno por la membrana, la producción neta de hidrógeno en el reactor catalítico de membrana es claramente superior por el desplazamiento de la reacción.

INDEX

CHAPTER 1

Introduction

1.1 Society and energy

Energy and infrastructure are linked to technological development. Over time, the growing world population has increased its energy demand. Mankind has used many different sources of energy, according to their needs for this development: from the kinetic energy of big animals, over the use of firewood, steam and coal to the fossil fuels we currently use as the basis of global energy. Fuels such as gasoline, diesel and gas contain a high level of energy and – at least for the moment – satisfy the need for energy that today´s society has. Around 80% of the energy used today comes from these primary energy sources [1], which are fossil, therefore are finite resources. So over time the cost of their extraction will increase and it will be necessary to look for alternative sources of energy.

Besides the monetary issue, there is also an environmental cost of fossil energy: Among other indicators, it is reflected nowadays in the air pollution of urban areas, reaching sometimes very unhealthy levels [2].

The increasing concentration of carbon dioxide (CO_2) in the atmosphere brings with it many changes in the global balance of gases and temperature in our atmosphere [1]. In the last 20 years, accumulation of toxic gases in the earth's atmosphere has risen despite the continuous technological improvement to minimize these emissions [2]. Moreover, in the last 200 years the concentration of some gases like NOx and SOx in the atmosphere has increased to unacceptable limits with disastrous results for the environment: smog, acid rain, greenhouse effect and climate change [3]. According to the Intergovernmental Panel on Climate Change (IPCC) [4], since 1900 the atmospheric warming has been accelerating and the number of record temperatures reached in the last 25 years is a tangible proof of this effect. The Earth has warmed by an average of 0.3 to 0.6 °C, due to the intensification of a natural phenomenon essential for survival on earth: The greenhouse effect. The dependence on fossil fuels leads to emissions of greenhouse gases, most notably CO_2 (80% contribution), a product of combustion [4]. As global energy demand continues to grow, it is expected that global emissions of carbon dioxide increase by 1.7% each year [5]. In that way the use of fossil fuels for energy needs will quickly result in environmental critical problems in ecosystems of all regions

of the world [9]. The IPCC estimates that temperatures may reach between 1.4 and 5.8 °C at the end of this century if no action is taken in this regard [3].

With regard to the EU, the annual energy demand has increased since 1986 by 1 to 2% on a yearly basis. As shown in Table 1.1, the energy consumption of the European Union in 2009 was covered mainly by oil (40.4%) and natural gas (24.4%), and only 4.3% by renewable sources of energy. If this development continues without a change, by 2030 the energy balance will still be based on fossil fuels: 38% gained from oil, 29% from natural gas, 19% from coal, 6% nuclear and 8% renewable energy [4]. When looking at the energy consumption by economic sector, private households and the service sector are the biggest consumers of final energy in absolute terms, with households being the major consumers of natural gas (one third of all gas consumed) and about 18% of all oil consumed.

Area	Oil	Gas	Carbon	Nuclear	Renewable	Total
	toe	toe	toe	toe	toe	toe
North America	1122.4	705.9	603.8	210.4	141.9	2784.4
Latin America	221.7	106.2	18.7	4.4	132.1	483.1
European Union	694.5	420.2	307.0	223.4	73.7	1718.8
Middle Orient	250.9	218.0	9.1	-	4.0	482.0
Former USSR	186.0	531.0	175.0	56.0	56.3	1004.3
Africa	124.3	61.8	102.8	3.4	19.8	312.1
Asia	1090.5	330.9	1506.6	118.9	152.0	3198.9
TOTAL	3690.3	2374.0	2723.0	616.5	579.8	9983.6

Table 1.1 World energy consumption in 2009 [4].

In Spain, the energy consumption in 2007 was 145.9 toe (tone of oil equivalent), which represents an increase of 2.6% compared to 2006, as shown in Table 1.2. There is high oil consumption, about 50%, although a slight decrease in favour of natural gas can be observed.

Energy	2005		2006		2007	
	toe	%	toe	%	toe	%
Carbon	20.4	15.0	20.9	14.7	21.1	14.5
Oil	69.3	50.8	71.0	50.0	71.7	49.2
Gas	21.2	15.6	24.6	17.4	29.1	20.0
Nuclear	16.1	11.8	16.5	11.7	14.9	10.3
Renewable	9.2	6.8	9.1	6.4	8.8	6.1

Table 1.2 Spain's Energy Consumption [6].

Table 1.3 shows that in 2007, the European Union consumed 1157.6 toe of all different kinds of energies, but only produced 859 toe. The degree of energy self-sufficiency decreased from 57% in 1990 to 51% in 2007 due to the increasing import of all primary energy sources, especially coal, gas and oil (77%) [6]. If this trend continues, gas imports will increase to 80% over the next 20 years and, if we fail to provide more competitive domestic energy over the next 20 to 30 years, around 70% of energy needs for European Union will be supplied by imported products [7].

Toe	1990	2007	Toe	1990	2007
Total energy produced	936.0	859.4	**Total energy consumed**	1067.5	1157.6
Carbon	366.4	187.7	**Carbon**	125.0	53.8
Oil	129.5	121.6	**Oil**	444.4	484.6
Gas	162.4	167.3	**Gas**	227.9	268.7
Nuclear	202.5	243.2	**Nuclear**	184.1	244.4
Renewables	72.7	138.8	**Renewables**	37.2	63.1
Industrial waste	2.2	2.6	**Industrial waste**	48.8	42.8

Table 1.3 Comparative production and consumption of energy in 1990 and 2007 for the European Union [4].

In Spain, the power system is principally based on the import of coal, natural gas, and particularly oil (Table 1.4). However, the main energy sources that are locally available are nuclear and renewable, used for local consumption [8]. This shows that the dependence of Spain and the rest of Europe on imports is increasing and, if we do not stop the growth consumption in key sectors, which include transport, private households and services, energy dependence for EU will continue to increase [4].

Energy	primary energy consumption		Energy Production		Self sufficiency
	toe	%	toe	%	%
Carbon	21.1	14.5	6.6	21.5	31.3
Oil	71.7	49.2	1.6	0.5	0.2
Gas	29.1	20.0	1.4	0.5	0.5
Nuclear	14.9	10.3	14.9	48.7	100.0
Renewable	8.8	6.1	8.8	28.7	100.0
TOTAL	145.9	100	30.7	100	21.1

Table 1.4 Consumption, production and supply of energy in Spain (2007) [6].

Furthermore, as the geographical location of global energy supplies is not where the major part of energy is consumed, energy supply will increasingly be subject to regional political instability. The reserves of oil and natural gas are concentrated in few countries. Over 70% of global oil reserves are located in countries of the Organization of Petroleum Exporting Countries (OPEC). It is expected that in 2020 OPEC will cover only 50% of the oil energy needs of the European Union, even though producing about 55 million barrels per day, compared to 32 million barrels per day in 2000. On the other hand, about half of the gas consumption for EU is satisfied with gas from only three countries: Russia, Norway and Algeria. In geopolitical terms, 45% of European oil imports originate in the Middle East, and 40% of natural gas imports come from Russia [4,7]. Therefore, the geopolitical conditions threaten the smooth operation of the European fossil fuel market.

1.2 Renewable energies

The increasing growing awareness of the great climate damaging effect in combination with the instabilities present in some countries in the fossil fuel market are leading to increasing political drive to reduce emissions of greenhouse gases and to stimulate renewable energy. In 1997, the first international steps in this direction were made in the Kyoto Protocol. This protocol, signed by more than 160 countries and covering over 55% of the global greenhouse gas emissions, obligates the participating industrialized countries to reduce their greenhouse gas emissions by 5% (with respect to 1990) in the

period 2008 to 2012. Unfortunately, the Kyoto Protocol was not ratified by the United States, the world's largest emitter of greenhouse gases. Still, the Kyoto Protocol has created a worldwide awareness and many new developments in the field of renewable energy have taken place since then. For example, in March 2007 the European Union committed itself to a 20% renewable energy target and a minimum target of 10% for transport biofuels by 2020. Although these measures are important steps in the right direction, much more of these steps will be required before society is completely based on renewable energy.

The sun radiates more than 170000 TW to our planet [9], whereas the total world energy consumption in 2001 was around 13.5 TW and is expected to increase to between 27 and 40.8 TW in the year 2050 [10]. This means that the total amount of solar energy reaching the earth in one hour is in the same order as the total world energy consumption in one year [10]. However, a society that is completely based on solar energy is not considered to be a realistic option on a short term due to technological and economic obstacles. Therefore, other renewable energy technologies are being developed in parallel to solar energy. About 2000 TW of the 170000 TW solar radiation flux is continuously transformed into wind power, 100 TW is continuously stored as biomass through photosynthesis [11], and 6 TW is continuously transformed into hydropower through the water cycle. Nowadays, these indirect forms of solar energy are exploited to some extent for electricity production through wind turbines, biomass gasification/combustion and hydroelectric dams. Although these indirect forms of solar energy can be exploited for electricity production on a much larger scale in the future, a renewable society will also require large amounts of renewably produced chemicals and fuels.

1.3 Ethanol

Ethanol is probably the first product ever obtained by a catalytic (enzymatic) process in mankind history; as a beverage it has been produced since almost 5000 years in the Ancient Egypt. Since then, most human cultures and societies have been producing it, using practically any natural resource suitable for fermentation. Apart from its use as a beverage, ethanol is one of most versatile organic chemicals because of its unique

properties as a solvent, an antifreezing agent, a germicide, a fuel and especially as a chemical intermediate for other organic chemicals. Under ordinary conditions, it is a volatile, flammable, transparent and colourless liquid with a pleasant and characteristic odour. The physical and chemical properties of ethanol are primarily dependent upon the reactivity of the hydroxyl group, which makes it a polar compound and gives rise to intermolecular hydrogen bonding. A very peculiar property of ethanol is the volume shrinkage that occurs when mixed with water and the volume expansion when mixed with gasoline [12]. As a fuel, ethanol has a high octane rating: 109 RON (Research Octane Number), 90 MON (Motor Octane Number), and it is currently used in fuel blends for spark ignition engines.

The term *bioethanol* is currently used to refer the ethanol produced from biomass resources by biological processes (fermentation, enzymatic catalysis). The term is also applied, in a broader sense, to all alcoholic liquors produced by fermentation of sugars from plants, where the alcohol-to-water ratio on a molar basis is between 1:7 and 1:12. Ethanol is therefore considered a renewable resource, due to its easy and broadly implemented production from a variety of plants. Ethanol has high hydrogen-to carbon ratio of 3, and high hydrogen content per unit volume in the liquid state. In addition, ethanol distribution networks are already available in many countries. All these factors make it a very attractive raw material for hydrogen production, especially for mobile applications.

There has been considerable discussion on the global energy efficiency obtained when fuel bioethanol is produced from agriculture products (for instance, from corn), because of the energy used in planting and harvesting, fertilizer, transportation, and processing into ethanol. It has been reported that the energy output in the fuel ethanol is at least 1.34 times (1.53 under a best-case scenario) the energy used in its production from corn [13,14]. Most of this energy consumed in processing is used to remove all water after fermentation. Then, the global energy balance would be considerably improved when bioethanol is used in processes using water as reactant (such as reforming) to produce hydrogen for fuel cells, instead of using it as a fuel mixed with gasoline [15].

1.3.1 Bioethanol manufacture

Though industrial ethanol can be produced synthetically by hydration of ethylene or as a by-product of certain industrial operations, most of it is produced by fermentation of sugar, starch or cellulose. For instance, fermentation processes share of total production in US, Western Europe and Japan increased from 83% in 1997 to 90% in 2001 [14]. Bioethanol is produced by anaerobic fermentation of sugars in aqueous solution by yeasts, which produces beverage-grade alcohol containing about 14% ethanol. However, to obtain pure ethanol to use as a gasoline additive, the aqueous ethanol obtained from fermentation process needs to be distilled. This is an energy-intensive process and contributes over 50% to the total cost of ethanol production [16]. Due to the first oil crisis of 1973, Brazil started in 1975 the ProAlcohol program to produce fermentation alcohol from sugar cane for its use as fuel in gasohols. Since then, the increasing demand of ethanol as fuel component, and as a substitute for MTBE, has rocketed the world production. Thus, in spite of the economical crisis, it increased from 40164 million litres in 2004 to 86714 million litres in 2011 [17]. The United States, where most fuel alcohol is currently made mainly from grains, mostly corn, is currently the first world producer of ethanol, followed by Brazil; together, they represent near 86 % of the world total production.

The use of edible plants (especially corn) and as a source of fuel ethanol has increased their price in such a way that has opened a conflict of interests between its use as a source of food vs. a source of fuel. This has generated the need of researching the use of non-edible natural resources (grasses, straw, etc.) to produce bioethanol. This biomass is lignocellulosic and accounts for about half of the world biomass. The use of lignocellulosics increases greatly the availability of raw materials for ethanol production and reduces the production price markedly. However, the complex molecular structures of lignocellulosics make production of ethanol from them more difficult than from sugar cane or starch-rich materials [18]. All processes for ethanol production from lignocellulosics consist of two main steps: hydrolysis of cellulose and hemicellulose to monomeric sugars, and subsequent fermentation to produce bioethanol. A more detailed description can be found in reference [19].

1.4 Catalytic routes to hydrogen production from ethanol and bioethanol

Hydrogen is considered as one of the future energy vectors. Considered a third generation fuel, it does not pollute air, water or underground, it provides energy in a fuel cell and in this electrochemical process we only get water and heat as waste. It seems difficult to find a better clean energy source and most environmentally friendly [20].

There are three main reaction pathways for producing hydrogen directly from ethanol, all of them catalytic, that differ by the co-reactant used, the process chemistry and the maximum hydrogen yield reachable, namely: steam reforming, partial oxidation, and its combination, autothermal reforming.

The highest hydrogen production can be obtained by ethanol steam reforming (ESR) where ethanol reacts with water steam to give carbon dioxide and hydrogen. The overall reaction can be formally written as:

$CH_3CH_2OH\ (g) + 3\ H_2O\ (g) \rightarrow 2\ CO_2\ (g) + 6\ H_2\ (g)$ $\quad \Delta H^{o}_{298\ K} = 173.3$ kJ/mol (1.1)

Though reaction stoichiometry determines a steam-to-ethanol molar ratio S/E = 3, rather higher ratios can be used. This is advantageous, as it allows using directly bioethanol produced by fermentation, where the S/E ratio is about 13, without any need of distillation.

Its main disadvantage is its high endothermicity, which brings along two drawbacks: a) a high energy input is needed to run the reaction, in addition to the energy needed to evaporate both liquid reactants and to heat the steam; and b) hydrogen formation is limited by thermodynamic equilibrium. The latter can be improved by increasing the steam-to-ethanol ratio [21].

Another important issue is that reaction conditions may lead to formation of carbon monoxide:

$CH_3CH_2OH\ (g) + H_2O\ (g) \rightarrow 2\ CO\ (g) + 4\ H_2\ (g)$ $\quad \Delta H^{o}_{298\ K} = 255.5$ kJ/mol (1.2)

thus reducing the hydrogen yield to 4 mol/ mol of ethanol. This reaction introduces another problem, because carbon monoxide is a poison for polymer electrolyte membrane fuel cell (PEMFC) electrocatalysts: a high CO content in the ESR product current makes unavoidable a further purification step to reduce it to levels below few ppm in the feed to the fuel cell [22]. In this case, the water gas shift (WGS) reaction can be used to recover additional hydrogen:

$$CO\ (g) + H_2O\ (g) \rightarrow H_2\ (g) + CO_2\ (g) \quad \Delta H^{o}_{298\ K} = -40.4\ kJ/mol \qquad (1.3)$$

(in fact, reaction 1.1 is the result of reaction 1.2 followed by reaction 1.3).

Partial oxidation of ethanol (POE), the reaction of ethanol with oxygen to produce hydrogen and carbon dioxide, overcomes these drawbacks, but the maximum hydrogen yield is 3 mol/mol of ethanol:

$$CH_3CH_2OH\ (g) + 3/2\ O_2\ (g) \rightarrow 3\ H_2\ (g) + 2\ CO_2\ (g) \qquad \Delta H^{o}_{298\ K} = -552\ kJ/mol \qquad (1.4)$$

However, for low oxygen-to-ethanol (O/E) molar ratios, carbon monoxide can be also produced, but the reaction is thermodynamically unfavoured:

$$CH_3CH_2OH\ (g) + 1/2\ O_2\ (g) \rightarrow 3\ H_2\ (g) + 2\ CO\ (g) \qquad \Delta H^{o}_{298\ K} = 14.0\ kJ/mol \qquad (1.5)$$

Though the maximum hydrogen yield is lower than in ESR, POE presents the advantages brought by its exothermicity: a) there is no need of external energy input, simplifying the process scheme by avoiding the heating units; b) there are no equilibrium limitations, allowing to operate at temperatures markedly lower than those used for ESR, say, between 473-873 K; and c) reaction is much faster, and then, the reactor needed is smaller than for ESR. All these factors contribute to make the process setup much more compact. Moreover, the co-reactant (oxygen) is a gas (no need to evaporate it), which can be substituted by air directly taken from the atmosphere. Both features are of great interest for on board hydrogen production for mobile applications of fuel cells. The presence of oxygen can also contribute to decrease the formation of carbonaceous residues on the catalyst surface, thus keeping the catalytic activity for longer periods.

The main drawback of POE is common to all selective or partial oxidation processes in the gas phase: the competing total oxidation (combustion) reaction is much more favoured thermodynamically:

$CH_3CH_2OH\ (g) + 3\ O_2\ (g) \rightarrow 2\ CO_2\ (g) + 3\ H_2O\ (g) \qquad \Delta H^o_{298\ K} = -1293\ kJ/mol \qquad (1.6)$

The oxidation of hydrogen is also very exothermic (and hence thermodiynamically favoured):

$H_2\ (g) + 1/2\ O_2\ (g) \rightarrow H_2O\ (g) \qquad \Delta H^o_{298\ K} = -241.0\ kJ/mol \qquad (1.7)$

As a result, hydrogen selectivity is usually low. Moreover, the mixture of a fuel (ethanol) with oxygen entails the risks of explosion and the need to operate outside the explosion (flammability) range, i.e., from 3.5 (lower) to 19 (upper) % v/v in air [23].

The autothermal reforming (ATR), also known as oxidative steam reforming (OSR), seeks to contribute the heat released by the partial oxidation reaction to the steam reforming reaction. The feed consists of a mixture of water, ethanol and oxygen whose concentrations should be adjusted correctly to ensure that the net enthalpy of the reaction is close to thermal neutrality, producing predominantly hydrogen and carbon dioxide:

$$CH_3CH_2OH\ (l) + (3-2x)\ H_2O\ (l) + x\ O_2\ (g) \rightarrow 2\ CO_2\ (g) + (6-2x)\ H_2\ (g)$$
$$\Delta H^o_{298\ K} = (173.3 - 483.6\ x)\ kJ/mol \qquad (1.8)$$

where x stands for the ethanol-to-oxygen molar ratio. Due to this thermal near-neutrality, ATR avoids the drawbacks of ESR, because it does not need an external supply of heat, if the concentrations of water, ethanol and oxygen are properly adjusted, and may be operated at much lower temperatures than ESR. For instance, by using x = 0.6, the reaction (1.8) becomes thermally near-neutral: $\Delta H^o_{298\ K}$ = +4.4 kJ/mol, with $\Delta G^o_{298\ K}$ = -187.2 kJ/mol [24]. But adjustment can be made in various ways. If one keeps S/E = 3 at 973 K, 0.482 mol of oxygen per mol of ethanol are required to achieve zero enthalpy. Moreover, the presence of water in the feed inhibits the flammability and explosion risks of the oxygen-ethanol mixtures, decreases combustion selectivity and retards the carbonaceous residue deposition on the catalyst surface. However, it is

difficult to control the working conditions for a steady state operation, and to optimize catalysts with the needed functionalities in the adequate proportion. As an alternative, the coupling of both ESR and POE reactions in separate but integrated reactors has been investigated [25]. In this case, the complexity of the control of the reaction conditions to keep thermal neutrality remains, but catalysts for each reaction can be optimized separately.

Thermodynamic equilibrium of ESR, POE and ATR was studied by Gibbs free energy minimization including the possibility of solid coke formation for the ranges of S/E = 0-10, O/E = 0-3 and reaction temperatures (T_R) of 473-1273 K [26]. The main conclusions were:

a) Ethanol processed with steam and/or air will yield to the decomposition of ethanol over the whole T_R range studied, to methane and CO_2 at low T_R, but at T_R > 673 K methane is reduced, hydrogen content rises strongly and CO also evolves;

b) A higher hydrogen yield is possible in ESR than in POE; in the favourable operation window, i.e., T_R = 823-923 K and S/E > 4, a hydrogen yield of 4 mole/mole of ethanol, with CO mole fraction < 0.1 and without danger of coke formation is possible.

c) In POE high hydrogen contents appears jointly with high CO content, and reasonable hydrogen yields can be achieved at O/E < 1.5 and T_R > 873 K but avoiding coke formation requires O/E> 0.8; this makes POE an unfavourable choice for hydrogen-rich feeds for fuel cells due to high CO content, but useful for synthesis gas production.

d) The main advantage of ATR, besides reducing the energy demand for ESR, is to reduce coke formation rate; over the whole S/E-ratio range, increasing O/E-ratio from 0 to 0.75 in ATR shows no strong effect on the hydrogen and carbon monoxide formation at T_R < 873 K.

The total energy demand per mole of hydrogen produced follows the order POE < ATR < ESR. Nevertheless, the higher hydrogen yield attainable by ESR and the technological maturity of other steam reforming processes make that, in practice, most research is devoted to ESR.

The hydrogen production from ethanol have been the aim of several reviews in the literature, but most of them are devoted to ESR [27,28,29], fewer review and compare the three alternative routes [16,18] and just one is devoted to partial oxidation of ethanol (and methanol) [30].

It should be noted that the apparent simplicity of equations 1.1, 1.4 and 1.7 represent just overall stoichiometric reactions, respectively, for ESR, POE and ATR, but the real reactive systems are very complex. Due to the high intrinsic reactivity of ethanol, and that of the reaction intermediates and products among them and with the water and/or oxygen in the feed, there are many reactions occurring simultaneously. They result in a lower hydrogen yield [16] and processes leading to catalyst deactivation. For these reasons, they are described in detail in the next Section.

1.4.1 Reaction pathways and thermodynamics

As explained in [31], in the absence of any other reactant, the main reactions of ethanol itself, as a typical alcohol, are dehydrogenation to acetaldehyde (reaction 1.9) and dehydration to ethylene (reaction 1.10):

$CH_3CH_2OH\ (g) \rightarrow CH_3CHO\ (g) + H_2\ (g)$ $\quad \Delta H^o_{298\ K} = 68.4\ kJ/mol$ (1.9)

$CH_3CH_2OH\ (g) \rightarrow CH_2{=}CH_2\ (g) + H_2O\ (g)$ $\quad \Delta H^o_{298\ K} = 45\ kJ/mol$ (1.10)

Ethanol may also decompose to methane and carbon oxides:

$CH_3CH_2OH\ (g) \rightarrow 1/2\ CO_2\ (g) + 3/2\ CH_4\ (g)$ $\quad \Delta H^o_{298\ K} = -74\ kJ\ /\ mol$ (1.11)

$CH_3CH_2OH\ (g) \rightarrow CO\ (g) + CH_4\ (g) + H_2\ (g)$ $\quad \Delta H^o_{298\ K} = 49\ kJ\ /\ mol$ (1.12)

Both acetaldehyde and ethylene are important intermediates that might be formed even at low temperatures, before the formation of hydrogen and carbon oxides through ESR reactions 1.1 and 1.2. While ethylene is a precursor of coke formation, acetaldehyde plays an important role in the pathways leading to hydrogen formation. Acetaldehyde may decompose into methane and CO o condensate to produce acetone:

$CH_3CHO\ (g) \rightarrow CO\ (g) + CH_4\ (g)$ $\quad \Delta H^o_{298\ K} = -18.8\ kJ\ /\ mol$ (1.13)

$2\ CH_3CHO\ (g) \rightarrow CH_3COCH_3\ (g) + CO\ (g) + H_2\ (g)$ $\Delta H^o_{298\ K} = 5.1$ kJ/mol (1.14)

This condensation can be very favoured by the presence of water:

$2\ CH_3CHO\ (g) + H_2O\ (g) \rightarrow CH_3COCH_3\ (g) + 2\ H_2\ (g) + CO_2\ (g)$

$\Delta H^o_{298\ K} = -35.9$ kJ/mol (1.15)

When water in present, either introduced in the feed for ESR or as a reaction product in POE, it may react with ethanol (reactions 1.1 and 1.2), but also with the products evolved from ethanol in reforming reactions:

$CH_3CHO\ (g) + 3\ H_2O\ (g) \rightarrow 2\ CO_2\ (g) + 5\ H_2\ (g)$ $\Delta H^o_{298\ K} = 104.8$ kJ/mol (1.16)

$CH_3CHO\ (g) + H_2O\ (g) \rightarrow 2\ CO\ (g) + 3\ H_2\ (g)$ $\Delta H^o_{298\ K} = 187.1$ kJ/mol (1.17)

$CH_2{=}CH_2\ (g) + 4\ H_2O\ (g) \rightarrow 6\ H_2\ (g) + 2\ CO_2\ (g)$ $\Delta H^o_{298\ K} = 127.6$ kJ/mol (1.18)

$CH_4 + 2H_2O \rightarrow CO_2\ (g) + 4\ H_2\ (g)$ $\Delta H^o_{298\ K} = 164.4$ kJ/mol (1.19)

and the water gas shift (WGS) reaction:

$CO\ (g) + H_2O\ (g) \rightarrow H_2\ (g) + CO_2\ (g)$ $\Delta H^o_{298\ K} = -40.4$ kJ/mol (1.20)

The final result is a higher yield to CO, CO_2 and hydrogen than in absence of water. Note that all reactions that give methane are exothermic and favoured at low temperatures and tend to reduce hydrogen production. Then, the formation of methane should be avoided in the ESR [32]. Furthermore, the hydrogen formed may, in turn, produce other hydrogenation reactions:

$CH_3CH_2OH\ (g) + 2\ H_2\ (g) \rightarrow 2\ CH_4\ (g) + H_2O\ (g)$ $\Delta H^o_{298\ K} = -157$ kJ/mol (1.21)

$CH_2{=}CH_2\ (g) + H_2\ (g) \rightarrow CH_3CH_3\ (g)$ $\Delta H^o_{298\ K} = -136.5$ kJ/mol (1.22)

$CO\ (g) + 3\ H_2\ (g) \rightarrow CH_4\ (g) + H_2O\ (g)$ $\Delta H^o_{298\ K} = -205.5$ kJ/mol (1.23)

$CO_2\ (g) + 4\ H_2\ (g) \rightarrow CH_4\ (g) + 2\ H_2O\ (g)$ $\Delta H^o_{298\ K} = -164.4$ kJ/mol (1.24)

These reactions are all exothermic and attention should be paid in the catalyst design to limit the hydrogenation function to minimize the hydrogen consumption by these reactions.

Coke formation on the catalysts surface is very often observed in the ethanol processing reactions. The mechanism of deposit formation seems to be common to both ESR and POE, and include several reactions:

$2\ CO\ (g) \rightarrow C\ (s) + CO_2\ (g)$ $\quad \Delta H^{o}_{298\ K} = -171.5\ kJ/mol$ (1.25)

$CH_4\ (g) \rightarrow C(s) + 2\ H_2\ (g)$ $\quad \Delta H^{o}_{298\ K} = 75\ kJ/mol$ (1.26)

$CH_2{=}CH_2\ (g) \rightarrow [polymers] \rightarrow 2\ C\ (s) + 2H_2\ (g)$ $\quad \Delta H^{o}_{298\ K} = -52.1\ kJ/mol$ (1.27)

$CO\ (g) + H_2\ (g) \rightarrow C\ (s) + H_2O\ (g)$ $\quad \Delta H^{o}_{298\ K} = -131.0\ kJ/mol$ (1.28)

$CO_2\ (g) + 2\ H_2\ (g) \rightarrow C\ (s) + 2\ H_2O\ (g)$ $\quad \Delta H^{o}_{298\ K} = -89.8\ kJ/mol$ (1.29)

All these reactions form a fairly complex reactive network that is outlined in Figure 1.1.

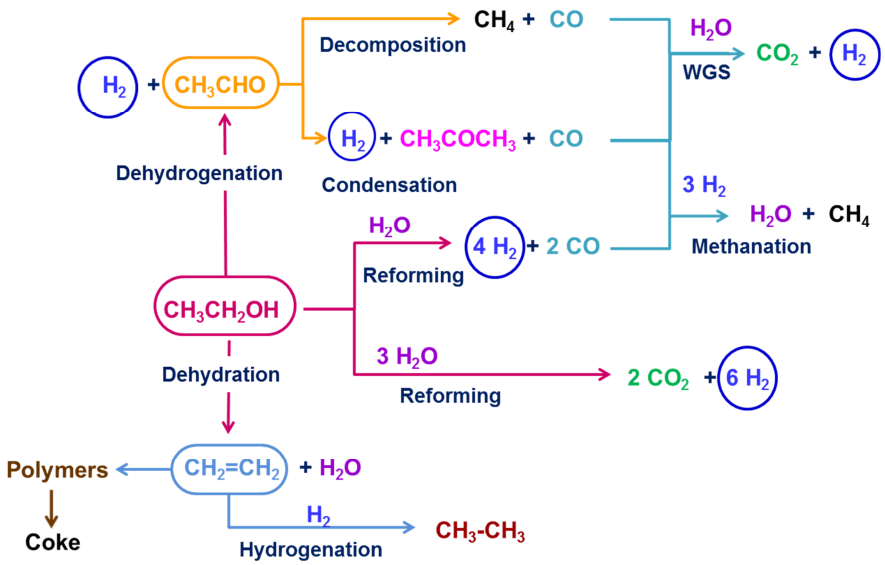

Fig. 1.1 Reaction scheme of the steam reforming of ethanol (ESR)

Taken from "Renewable Hydrogen Technologies" [31]

Thermodynamic equilibrium calculations performed at different S/E ratios and different pressures indicate that formation of undesirable by products, such as methane and CO, could be minimized by using higher S/E ratios and low pressure, preferably at 1 atm [16,33]. On increasing the total pressure the H_2 and CO_2 yields decrease, while the methane equilibrium concentration increases.

When oxygen is present its high oxidizing power causes the oxidation reactions to become predominant. In the POE process, besides the main reactions, namely, ethanol partial oxidations (reactions 1.4 and 1.5) and combustion (reaction 1.6), ethanol may undergo oxidehydrogenation to acetaldehyde:

$CH_3CH_2OH\ (g) + 1/2\ O_2\ (g) \rightarrow CH_3CHO\ (g) + H_2O\ (g)$ $\Delta H^{o}_{298\ K} = -153$ kJ/mol (1.30)

and, depending on the oxygen concentration, all intermediate products can be either partially oxidized:

$CH_3CHO\ (g) + 3/2\ O_2\ (g) \rightarrow 2\ H_2\ (g) + 2\ CO_2\ (g)$ $\Delta H^{o}_{298\ K} = -620.7$ kJ/mol (1.31)

$CH_3CHO\ (g) + 1/2\ O_2\ (g) \rightarrow 2\ H_2\ (g) + 2\ CO\ (g)$ $\Delta H^{o}_{298\ K} = -54.7$ kJ/mol (1.32)

$CH_4\ (g) + 1/2\ O_2\ (g) \rightarrow 2\ H_2\ (g) + CO\ (g)$ $\Delta H^{o}_{298\ K} = -35.9$ kJ/mol (1.33)

or totally oxidized (combustion reactions):

$CH_3CHO\ (g) + 5/2\ O_2\ (g) \rightarrow 2\ H_2O\ (g) + 2\ CO_2\ (g)$ $\Delta H^{o}_{298\ K} = -1167$ kJ/mol (1.34)

$CH_4\ (g) + 2\ O_2\ (g) \rightarrow 2\ H_2O\ (g) + CO_2\ (g)$ $\Delta H^{o}_{298\ K} = -799.6$ kJ/mol (1.35)

$CO\ (g) + 1/2\ O_2\ (g) \rightarrow CO_2\ (g)$ $\Delta H^{o}_{298\ K} = -283.0$ kJ/mol (1.36)

As water is the main byproduct in all oxidation reactions, it becomes the main co-reactant when oxygen is consumed, and all the reforming reactions indicated for ESR are also involved in POE, increasing the complexity of the overall reaction network. The simplified reaction network in the POE process is outlined in Figure 1.2, where reforming secondary reactions have been omitted for clarity.

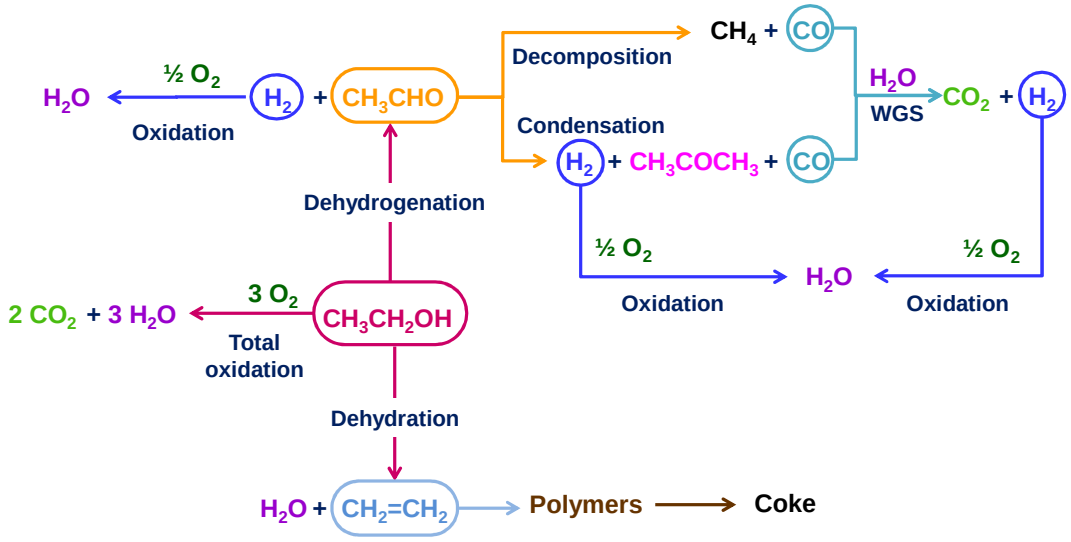

Fig. 1.2 Reaction scheme of the partial oxidation of ethanol (POE). For clarity, the reforming reactions with the water produced (equivalent to those in ESR in Fig. 1.1) are not shown. Taken from "Renewable Hydrogen Technologies" [31]

A comparison of the equilibrium compositions calculated for ESR with those for POE shows that the absence of steam in the feed decreases the H_2 concentration from >70% in the ESR reaction to ~50% in the POE reaction, and that to achieve a maximum H_2 yield temperatures above 873 K would be required for either ESR or POE, as long as CH_4 is considered in the calculation as one of the present species. If it is excluded, a high H_2 yield could be obtained at lower temperatures. This means that catalysts with low selectivity to decomposition into CH_4 could produce high yields of H_2 at temperatures around 573 K [16].

Autothermal refoming reaction network is equivalent to the one depicted for POE, but including all the reforming reactions depicted for ESR. The main difference lies on the different contribution of each reaction involved, due to the simultaneous presence of oxygen and steam in the feed.

Summarizing, the reaction networks for the three processes that convert ethanol into hydrogen are extremely complex, both from the mechanistic and the thermodynamic points of view. The intermediate steps involved include a variety of reaction types (dehydration, dehydrogenation, reforming, total and selective oxidation, WGS, etc.). They show different dependency relationships on reaction conditions and their

promotion depends on different functionalities of the catalyst. In addition, formation of coke precursors from several of the compounds involved makes deactivation an important issue for the practical application of these processes. All these factors explain the need for extensive research of catalysts, as well as of reactor and process engineering, to optimize hydrogen production and process performance. This PhD is mainly focused on the steam reforming process.

1.5 Catalyst for the steam reforming of ethanol

1.5.1 Noble metal catalysts

Many studies have been focused on the ethanol steam reforming using supported nickel, cobalt and noble metal catalysts. An efficient catalyst for hydrogen production from ethanol has to dissociate the C-C bond (at reasonably low temperatures), maintain low the CO concentration and be stable under catalytic operation. Deactivation, related to coke and carbonaceous compounds deposition, is the major drawback of the catalytic systems based on transition metals. Among transition metals, noble metals, and in particular Rh and Ru [34], are known to successfully break the C-C bond leading to less coke deposition and thus to more stable catalysts.

As explained above, the ethanol steam reforming (ESR) reaction mechanism over noble metals involves a complex set of reactions. In an early work by [35], the performance of different Rh-containing catalysts supported on Al_2O_3 for the ESR under steam-to-carbon ratio S/C = 4.2 was explored. At a preliminary stage, it was found that the reaction mechanism starts with the dehydrogenation and/or dehydration of the ethanol which are assisted by the acid support, followed by the rapid conversion of the products into CH_4, CO and CO_2, catalyzed by Rh. It was noticed that the presence of Rh at high temperatures (T = 923 K) prevents coke formation and the catalyst maintains its activity for several hours. [36] and [37] tested a wide range of catalysts in order to elucidate the best catalytic system. The former studied different active phases (Rh, Pt, Pd, Ru, Ni, Cu, Zn, Fe) as well as supports (Al_2O_3, CeO_2-Al_2O_3, CeO_2, CeO_2, CeO_2-ZrO_2, ZrO_2) in order to obtain highly active catalysts for the ESR rendering high H_2 yields and selective towards the formation of CO_2 both in the ESR and the WGSR. They found that the most active

and selective catalysts were the Rh and Ni-based ones, achieving the highest H_2 yield with the $Rh/CeZrO_2$ catalyst. [37] studied Rh, Pt, Pd and Ni catalysts supported over Al_2O_3 and CeO_2-ZrO_2 and obtained that Rh and Pt exhibited better performance and were more active when supported over ceria-zirconia mixed oxides.

Since these initial works, considerable effort has been done in the research of the ESR over noble metals, and Rh, Pt, Pd, Ru, Ir and Ag-based catalysts have been investigated. In more than 40% of the published works, Rh-based catalysts have been used as this metal is the most effective with respect to ethanol conversion and hydrogen selectivity, due to its strong capacity to successfully dissociate the C-C bond of the ethanol molecule [38,39]. Nearly 30% correspond to Pt-based catalysts taking advantage of the strong oxidation activity and the WGSR promotion of Pt and its high activity and selectivity towards H_2 production [40]. To a lesser extent, Pd-based catalysts have been used due to its known dehydrogenation and steam reforming of methane catalytic activity. Also, some works report on the use of Ru-based catalysts because their H_2 production is comparable to that of Rh only at high Ru loading. Whereas Rh catalysts are stable, Ru induces dehydration of ethanol to form ethylene, leading to coke formation via polymerization [41,42]. Iridium has been tested in few works [43,44] and it was found that Ir particles are responsible for the C-C bond cleavage in acetaldehyde which mainly decomposes to CO and CH_4, at temperatures above 673 K or is converted to acetone at lower temperatures. Finally, [42] also tested Ag/CeO_2 for the ESR obtaining poor activity of the catalyst being the main products H_2 and acetaldehyde between 373 and 873 K.

Bimetallic catalysts have synergetic effects; they show higher activity than the metals alone in bond dissociation, dehydrogenation and oxidation processes but few authors have studied them [45]. [46,47] studied $Rh\text{-}Pd/CeO_2$, obtaining that the direct oxidation route to acetate over CeO_2 is suppressed by the presence of the metals and the dehydrogenation reaction temperature is lowered by about 100 K in comparison with CeO_2 alone. Additionally, by in-situ IR studies, they inferred that the bimetallic catalysts break the C-C bond of ethanol at temperatures below 400 K. Rh-Pt and Pt-Pd supported over CeO_2 were studied by [47]. Rh-Pt was also tested by [48] for SR of 85% pure ethanol and 15% gasoline (E85).

Noble metals supported over alumina are often used because of its chemical and mechanical resistance under reaction conditions, although it is known that acid supports assist ethanol dehydration to ethylene at low temperatures, which in turn facilitates the formation of C deposits [35,49,50]. [51] carried out temperature programmed desorption (TPD) experiments concluding that under reaction conditions Al_2O_3 is not able to promote the desorption of the secondary reaction products, poisoning the surface catalyst and hindering the decomposition process which finally leads to a marked decay in H_2 and CO_2 selectivity. TPO studies allowed them to investigate the C formation; they found stable carbonaceous species and coke residues on both Al_2O_3 and Pt/Al_2O_3.

Although CeO_2 and Al_2O_3 oxides are the most used ones, other supports have been explored. ZrO_2, SiO_2, Y_2O_3, C, Nb_2O_5, $MgAl_2O_4$, MgO, TiO_2 and also zeolites have been tested as noble metal supports. Among these, ZrO_2 is the most frequently used due to its large oxygen storage capacity (OSC), high oxygen mobility and steam activation. Ce-Zr solid solutions have been widely used because the addition of ZrO_2 to the ceria lattice results in enhancing ceria redox properties, its basicity is reduced as the ZrO_2 content increases, its thermal resistance is improved and it also helps to increase metal dispersion [52,53,54].

To improve the performance of the catalysts and block coking different dopants have been tested. Dömök et al. [55] incorporated K (up to 0.4 wt.%) into Pt/Al_2O_3 which was found to destabilize surface acetate groups; the ESR activity and stability were improved in proportion with the K content. De Lima et al. [56] incorporated Sn into Pt/CeO_2 achieving improved stability. Yaseneva et al. [57] modified the support by introducing La, Pr and Sm into Ru and Pt supported catalysts: $Ce_xZr_{1-x}(La,Pr,Sm)_{1-2x}O_2/Al_2O_3$, as it is expected that the incorporation of low-valence cations (such as La, Gd, Pr) into the lattice of ceria-zirconia solutions stabilizes it and improves the lattice oxygen mobility [58]. Their results showed that Ru-containing catalysts doped by Sm were the most effective while among the Pt-based ones, La-doping led to the most active catalyst. Can et al. [59] and Le Valant et al. [60] added 10 wt.% of Sc, Y, La, Er and Gd to 1 wt.% Rh/Al_2O_3 catalysts. On these modified supports, the dehydration reaction, leading to olefins which are coke precursors, is disfavoured and consequently the ethanol

conversion and the hydrogen yield are increased. Duprez's group [60,61] has done extensive research on the addition of impurities to pure ethanol-water mixtures in order to simulate raw bioethanol, which is of major importance for a cost effective industrial application. Raw bioethanol contains higher alcohols and also aldehydes, amines, acids and esters.

1.5.2 Nickel catalysts

Nickel-based catalysts are the most frequently used in reforming reactions due to C-C bond rupture capability. Nickel has been generally supported onto alumina, because of its ability to withstand reaction conditions [62]. However, due to the alumina acid sites, this support tends to favour carbon deposition, for what other supports have been also tested. On the contrary to noble metals, ESR over nickel catalysts takes place at moderate temperatures. It has been generally observed that the selectivity to hydrogen is increased with the increase in temperature, water to ethanol molar ratio and nickel loading [63,64,65]. The reaction mechanism over nickel-based catalysts follows the same steps than over noble metal-based catalysts [66,67].

In contrast to noble metals, the particles of nickel species tend to sinter under ESR reaction conditions. Besides, acid sites on alumina favour the dehydration of ethanol to ethylene, competing with the dehydrogenation to acetaldehyde. Both facts, nickel particle sintering and alumina acidity generate carbon deposits, which deactivate the catalyst. To avoid these inconveniences, different promoters have been added to nickel-based catalysts. Copper is the most efficient promoter for the production of hydrogen [62]. Copper species are active in the WGS reaction to produce hydrogen and avoid the growth of nickel particles [68]. Youn et al. [68] also studied the effects of adding molybdenum to Ni/Al_2O_3. They observed that Mo reduces the interaction between Ni and alumina, increasing the reducibility of nickel species, and also prevents the growth of nickel particles [69]. Calcium, as well as Mg, is an efficient promoter to neutralize aluminium acid sites. Vizcaino et al. [70] modified Ni/Al_2O_3 catalysts with Mg, obtaining an increase in the catalytic activity due to lower ethylene formation. They also modified Cu-Ni/SBA-15 catalysts with magnesium and calcium. The dispersion of the Cu-Ni phase

was improved and its interaction with the support was strengthened [71]. The same group of authors studied the effect of Mg and Ca addition on coke deposition over Cu-Ni/SiO_2. They observed reduction of the metallic Cu-Ni particle size and strengthening of the metal-support interaction. Moreover, Mg- and Ca-promoted catalysts favoured the formation of defective carbon, which is more reactive and thermodynamically easier to be removed during ESR [72]. Magnesium produces less carbon deposition when added to Ni/CeO_2 catalysts, too. In [73] OSC and oxygen mobility of CeO_2 supports increased by adding magnesium into the lattice of Ni/CeO_2. The insertion of Mg into CeO_2 lattice efficiently promotes the reduction of Ce^{4+}. Mg-modified Ni/CeO_2 catalysts have larger OSC and smaller Ni crystallite size compared with bare Ni/CeO_2. Choong et al. [74] also observed that the addition of calcium on Ni/Al_2O_3 greatly reduces the acidity of Al_2O_3. Calcium also increased water adsorption, providing nickel catalyst the proximity and abundance of adsorbed OH groups.

1.5.3 Cobalt catalysts

Low-cost cobalt-based catalysts are less active for ESR than catalysts that contain noble metals, but they are very selective to H_2 and CO_2 because the reforming temperature can be as low as 623 K in such a way that the WGS occurs simultaneously with steam reforming and consequently CO concentration is kept low. In addition, methane is not an intermediate of the reforming process over cobalt-based catalysts and, consequently, high hydrogen yields are easy to achieve. The first work on ESR over cobalt catalyst was reported by [75], where the catalytic performance of cobalt supported over Al_2O_3, SiO_2, MgO, ZrO_2 and C was described. This pioneering work was followed by those of [76,77]. Cavallaro et al. [76] reported on the ESR over Co/Al_2O_3 and Co/MgO under S/C~4.2 aimed to simulate the composition of biomass-derived ethanol/water mixtures. They noticed that Co/Al_2O_3 decayed in short time because of coke deposition, whereas Co/MgO was found more stable. Llorca et al. (2002) [75] studied cobalt supported over a great variety of supports with different acidity and redox properties (MgO, Al_2O_3, SiO_2, TiO_2, V_2O_5, ZnO, La_2O_3, CeO_2 and Sm_2O_3) under S/C=6.5 to simulate bio-ethanol steam reforming. Supports with strongly acidic properties favoured the dehydration of ethanol

into ethylene whereas supports with basic properties favoured dehydrogenation of ethanol into acetaldehyde, which was recognized to be the first step of the reforming process over cobalt. The same conclusion was reached by [78,79] on Co/SiO_2 and Co/Al_2O_3 catalysts. On the other hand, supports with redox properties showed better properties for ESR because they favoured suppression of coke and reduction of cobalt. ZnO-supported cobalt showed the best catalytic performance. In-situ magnetic measurements coupled to ESR over the above cobalt catalysts allowed [80,81] to demonstrate that metallic cobalt is a highly active species for the reforming of ethanol. Under reaction conditions, the Co/ZnO catalyst showed 92% of reduced cobalt, mainly as small superparamagnetic nanoparticles. On the other hand, in-situ FTIR with CO as a probe molecule revealed that, in addition to metallic cobalt, oxidized Co species were also present at the surface, thus suggesting that the redox pair $Co^0 \leftrightarrows Co^{2+}$ is responsible for the activity of cobalt in ESR [82]. This has been recently supported by the combined XPS-TPD work of [83] over model Co/ZnO(0001) catalysts. The catalytic role of Co^0 and Co^{2+} during ESR has also been investigated by [84] over Co/MgO, who concluded that Co^0 is much more active for C-C cleavage and WGS, and by [85] over metallic and oxidized cobalt model surfaces. Over cobalt-based catalysts, ethanol is first adsorbed to yield ethoxy species, which undergo dehydrogenation and transform into acyl species (rate determined step; [86] which, in turn, react with activated water to yield hydrogen and carbon oxides. CH_4 is a secondary product formed through the methanation reaction [87]. Carbonates are formed at the surface of the catalyst and carboxylates are detected, which are believed to be spectator species. Dimethyl ketone can be also formed via condensation of acetaldehyde. A complete network of reactions can be found in [88]. The mechanism of the ethanol reforming reaction is accompanied by a simultaneous transformation of the cobalt phase. HRTEM, X-ray diffraction, Raman spectroscopy and in-situ magnetic measurements show that Co_3O_4 is active for ethanol dehydrogenation and, subsequently, is progressively reduced by the hydrogen generated during this first step of the reaction into CoO and metallic [89]. The same transformation has shown to occur over Co/CeO_2 by using in-situ XRD, controlled-atmosphere XAFS and XPS [89]. Lin et al. [90] reported by in-situ XRD that hcp Co possess higher activity than fcc Co for ESR. Once metallic cobalt is formed, the catalyst becomes very active for the ESR and the hydrogen yield increases sharply. However, a

consequence of this reaction scheme is that extensive carbon deposition occurs under reaction conditions upon formation of metallic cobalt nanoparticles [91] which certainly constitutes the major drawback of cobalt-based catalysts for ESR, although [87] claimed that catalysts can be regenerated with mild oxidation. It is important to highlight that most of the work reported in the literature concerning ESR over Co-based catalysts has been conducted at high S/C ratio or under diluted conditions (i.e. using inert gas as carrier), and only a few studies have been carried out directly with ethanol-water mixtures under realistic conditions, which obviously have a great impact on coke formation. Carbon deposition occurs in various geometries, including carbon nanotubes, fibers, platelets and onion shell-type [93].

Several strategies have been attempted to minimize coke formation over Co-based catalysts under ESR conditions. Llorca et al [94] incorporated Na^+ promoter into Co/ZnO (up to 1% w/w) and obtained an important decrease of coke deposition during ESR, as evidenced by XPS and HRTEM, due to blocking of strong acidic sites of the support, which leads to the formation of ethylene, a well-known coke precursor. The same catalysts were studied by [95] by EXAFS and concluded that Na^+ promoter enhanced the reducibility of Co phase on ZnO, thus resulting in a stable and active catalyst for ESR. Galetti [96] used a similar approach adding K^+ to a CuCoZnAl oxide, which resulted in a stable catalyst for ESR at 873 K. On the other hand, it has been demonstrated that alloying of cobalt with more electronegative elements such as Ni or Cu results in worse catalytic performance, whereas alloying of cobalt with the less electronegative elements Fe [97] and Mn [98,99] promotes the redox pair $Co^0 \leftrightarrows Co^{2+}$, both in terms of lower cobalt reduction temperature as well as fast re-oxidation, which in turn results in a better catalytic stability. The promoter, low coke deposition effect of Fe has also been pointed out by [100,101] with cobalt catalysts supported over Al_2O_3 and $SrTiO_3$.

Considerable efforts have been addressed towards the Co/CeO_2 and Co/ZrO_2 systems for ESR due to the large oxygen storage capacity and high oxygen mobility exhibited by ceria and ceria-zirconia solid solutions that are able to oxidize carbon residues and prevent extensive carbon deposition. Song and Ozkan and Song et al [102,103] used DRIFT and isotopic labelling to show the mechanism of carbon removal and the involvement of water in the reaction network over these catalysts during ESR. Lima et al [104] showed

that high S/C ratios and the presence of oxygen promoted cleaning of the Co surface under ESR for Co/CeO_2, as expected. Avila-Neto [105] have used in-situ temperature and spatial resolved XANES to show that the Co^{2+}/Co^0 ratio in Co/Al_2O_3 modified with La_2O_3 and CeO_2 can be tuned by choosing appropriate water and oxygen partial pressures to obtain stable catalysts for ESR operation. Rybak et al [106] pointed out that the ZrO_2/CeO_2 ratio exerts significant influence on the coke formation. Lebarbier et al [107] studied the effect of Zn promotion in Co/ZrO_2 catalysts and noted that addition of Zn inhibited the oxidation of metallic cobalt particles under ESR. Enhanced oxygen mobility in CeO_2 was achieved by Ca^{2+} incorporation, which originated unit cell expansion in the ceria lattice and improved catalytic performance in ESR as well [87]. The influence of the preparation method on the reducibility of Co/Ce-Zr-O catalysts was reported by [102,108]. A proper metal-support interaction allows only partial reduction of cobalt and leads to a superior catalytic performance for the production of hydrogen through ESR. Long-term catalytic runs exceeding 750 h were reported by [109].

Noble metal (Pt, Pd, Rh, Ru, Ir)-promoted cobalt catalysts have been also investigated for ESR [110]. The effects of the noble metals include a marked lowering of the reduction temperature of the cobalt surface species interacting with the support due to hydrogen spillover and the stabilization of Co sites in the reduced state throughout the reaction. This causes an enhancement of catalytic activity, but in most cases causes rapid deactivation by coke deposition. The best catalytic performance for ESR was obtained for the CoRu formulation.

1.6 Hydrotalcites

As explained in [111], layered double hydoxides (LDHs), also known as anionic clays or hydrotalcite (HT)-like materials, have anionic exchanged capacity. The ability to capture and exchange organic and inorganic anions makes the compounds almost unique as inorganic materials. Hydrotalcites have been used in large number of practical applications such as neutralizers (antiacids), anion exchangers, polymer stabilizers, anion scavengers, catalysts and catalyst supports, adsorbents, filtration, electroactive, photoactive materials and pharmaceutics [112-118]. HTs are usually chosen over other compounds due to the versatility, simplicity, easily tailored properties and low cost of

the materials. HTs consist of a brucite-like [Mg(OH)2] network wherein an isomorphous substitution of Mg^{2+} ion by a trivalent cation M^{3+} occurs and the excess positive charge is compensated by anions, like carbonate, which are located in the interlayer along with water molecules [119-121]. Mg^{2+} may be accommodated in the octahedral sites of the close packed hydroxide ions in the brucite-like layers to form LDH structures [122]. Cations which are too small, such as Be^{2+}, or too large, such as Cd^{2+}, give rise to other types of compounds [123]. Hydrotalcites can be synthesized by various techniques depending on the specific requirement and properties of the compounds. The widely acceptable methods to prepare hydrotalcites include: salt-oxide method [124], hydrolysis reaction [113,115,125], deposition/precipitation reactions, structure reconstruction [126], hydrothermal synthesis, anion exchange [127], electrochemical methods, precipitation at constant pH (also called co-precipitation to indicate that all cations precipitate simultaneously), precipitation at variable pH, precipitation at different levels of supersaturation [110], combustion, sol–gel [124,125], microwave irradiation [111], steam activation and solvothermal method [111].

1.6.1 Hydrotalcites as catalysts

Since these materials have a well-defined layered structure with nanometer (0.3–3 nm) interlayer distances and contain important functional groups, they are widely used as adsorbents for liquid ions [130-132] and gas molecules [133,134]. They also find use as catalysts for oxidation [135-137], reduction [138] and other catalytic reactions [139,140]. LDH compounds are used in membrane CO_2 separation [141,142] and reactive separation applications, where the conversion of catalytic reactions can be increased by directly removing one of the products from the reactor [143,144]. This process is possible due to the permanent anion-exchange and adsorption capacity, the mobility of the interlayer anions and water molecules, the large surface areas and the stability and homogeneity of the HT materials [145].

The ability of HT to adsorb inorganic as well as organic anions makes these materials very attractive for many applications. HT has been used in the plastics industry [146,147], as an antacid substance and as a carrier for drugs [149-150]. HT-based metal oxides also have the potential to be used as new bifunctional catalysts with a unique

combination of acid–base and redox properties [151]. The great interest for the LDH materials is related to the fact that the acid–base properties of LDH-based catalysts, as well as the redox properties, may be easily tailored by isomorphous substitution of Mg and Al cations with various other di- and trivalent cations. The effects of isomorphous substitution on the surface and catalytic properties have been investigated by various methods, namely FTIR, XPS, TPR, TPD and microcalorimetry in many test reactions, such as cyclohexanol conversion [150,152,153], 2-octanol conversion [154], Knoevenagel condensation and aldol condensation [155,156] and the isomerisation of bisophorone to α-isophorone [157].

Hydrotalcites are commercially available and cheap solid bases. Calcined HTs are highly active and selective, and they can play an important role in many base-catalyzed reactions. Their reactive surface base sites were actively researched and characterized using temperature programmed desorption (TPD) [158,159], FTIR spectroscopy [160,161] and gas-phase microcalorimetry [153,162]. Their basicity is mainly related to the amount and nature of divalent cations present. Controlled thermal decomposition of hydrotalcites gives high surface area of mixed oxides that have the potentials in numerous catalytic applications such as the removal of SO*x* and NO*x*, aldol condensations, phenol alkylations, epoxidation of olefines, and partial oxidation, hydrodehalogenation or hydrogenation reactions [163-165]. HTs show a memory effect, a property by which they can recover the original lamellar structure if they come into contact with water vapor or are immersed in liquid water. These rehydrated materials have been applied to a number of base-catalyzed reactions on account of their Brønsted basic character [164,165,166]. In addition, acid sites or acid–base pairs on these materials may also influence the catalytic performance. Acid–base sites can be active sites for many reactions including Meerwein–Ponndorf–Verley reactions [167,168], cycloadditions of carbon dioxide to epoxides [169], and aldol condensations [170]. The acid–base properties of Mg–Al mixed oxides are governed by the Mg:Al molar ratio [159-161], calcination temperature [171] and preparation conditions [155,158,160]. They can be easily separated and recycled, while pollutant salts and by-products are not formed in the processes [172]. The rehydration of the Mg–Al mixed oxides gives rise to a

meixnerite Mg–Al hydroxide in which the original layered structure is restored by compensating the lost anions.

1.7 Catalytic wall reactors

Most ESR studies for hydrogen production have used conventional packed bed reactors, but the use of structured catalytic wall reactors offers important advantages in terms of efficiency, such rapid mass and heat transport, low pressure drop and no reactor blocking, good structural and thermal stability, and precise control of process conditions with higher hydrogen yields. In addition, they are robust, easy to scale up on an industrial basis and replace, and offer homogeneous flow distribution patterns. Regarding ESR over Co-based catalytic walls, [25] reported the preparation of cordierite honeycombs coated with Co/ZnO catalysts and their catalytic performance for ESR. Monoliths loaded with cobalt talc in SiO_2 aerogel host were prepared under supercritical conditions by [173]; they exhibited fast start-up and were about four times more active for hydrogen generation under ESR at 623 K than monoliths loaded with Co/SiO_2, which was related to the better mass transfer characteristics of the aerogel support. Metal plates coated with CoFe/ZnO and CoMn/ZnO catalysts by electrophoretic deposition were described by [174].

1.8 Ethanol reforming in catalytic membrane reactors

As discussed previously, the reaction temperature is an important operational parameter when conducting ethanol reforming reactions. High temperatures are necessary for C-C bond cleavage, but moderate temperatures are preferred for the WGS equilibrium to favour the formation of hydrogen and CO_2 at the expense of CO and water, thus maximizing the production of H_2 and avoiding the requirement of bulky WGS units at the reactor outlet. This condition considerably simplifies the fuel processor design, both in terms of number of catalytic stages required as well as heat transfer management. In this context, the use of catalytic membrane reactors (CMR), where the

generation and separation of hydrogen take place simultaneously, appears as an attractive approach to further simplify on-site/on-demand reformers (Figure 1.3). In addition, the shift effect that occurs in CMR results in even higher hydrogen yields because the presence of a membrane selective to the hydrogen permits attaining very high conversion values in comparison with the traditional reactors operating under the same conditions [175]. In fact, the continuous removal of one of the reaction products, the hydrogen, promotes the reaction conversion beyond the equilibrium values. With respect to a classical configuration consisting of a reactor unit in series with a separation unit, CMR represent a modern configuration in which an integrated reaction/separation unit has many potential advantages: reduced capital costs, improved yields and selectivities and drastically reduced downstream separation costs [176,177].

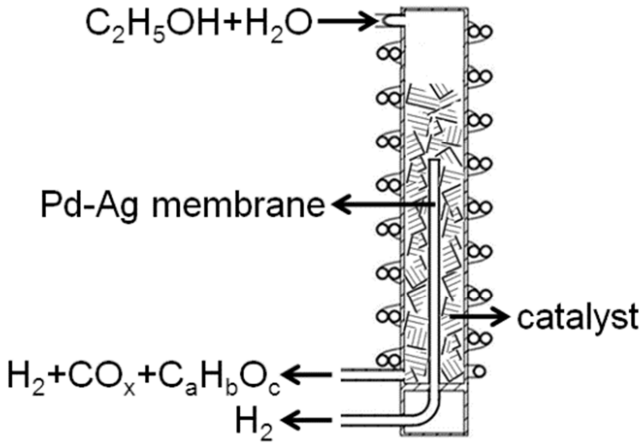

Fig. 1.3 Scheme of a catalytic membrane reactor for generating PEMFC-grade hydrogen from ethanol steam reforming. Taken from [31]

Among CMR, palladium-based membrane reactors fulfil the requirements to obtain an ultra pure hydrogen stream suitable for PEMFC feeding. Via innovative techniques, such as cold-rolling and diffusion welding developed at several laboratories and companies, robust Pd-based thin wall tubes less than 0.05 mm wall thickness have been produced [178] and their complete hydrogen selectivity and durability have been demonstrated in long term tests [179]. The hydrogen flux through the membrane increases with decreasing membrane thickness, and the overall cost decreases. Also, submicron-thick Pd-based membranes have been manufactured using microfabrication technology [180].

Today, numerous catalytic membrane reactors designs are available containing a bundle of Pd-based tubes or fingers [181,182]. These devices are capable for producing higher hydrogen throughputs than single tube membrane modules and can be used in compact reforming systems. In addition, the reject gas from the membrane can be used as a fuel source for a catalytic combustor to provide a self-sustainable operation [183]. Autothermal ESR operation in a fluidized membrane bed reactor with intrinsic CO_2 capture has also been proposed [184].

Commercial applications of Pd-based permeators for producing very pure hydrogen have been studied for more than fifty years (i.e. in the fuel cycle of the fusion reactors). In fact, palladium membranes are among the oldest membranes studied for gas permeation and separation applications and are still the membranes with the highest hydrogen permeability and selectivity [185]. They are receiving renewed attention because of the prospect of the hydrogen economy. The most critical issue for practical applications of Pd membranes in CMR for hydrogen production is the chemical stability of the metal membranes (poisoning effects of the reaction mixture on hydrogen permeation, carbon deposition on the membrane, etc.). For a better chemical stability (poisoning) and physical stability (mechanical stress, hydrogen embrittlement), membrane reactors do not use pure Pd but various different types of Pd alloyed with other metals such as silver, copper, nickel, iron and platinum. Most Pd alloy membranes studied are of binary components, with a few of multicomponents. Pd-Ag (23 wt% Ag) and Pd-Cu (38-42 wt% Cu) alloy membranes are nowadays widely employed in CMR for hydrogen production. The Pd-Ag is a plastic alloy with a specific hydrogen permeability of 3.4 Nm^3 mm m^{-2} h^{-1} $MPa^{-0.5}$ at 873 K [182]. The hydrogen permeated depends not only on the membrane properties, but it is also a linear function of the driving force, which in the case of Pd-based membranes generally is given by the difference of the square root of the H_2 partial pressure on both side of the membrane (Sieverts' law). The hydrogen permeation through dense Pd-based membranes follows a solution-diffusion transport mechanism, separation depending on the difference in diffusivity and solubility of hydrogen in the membrane. The membrane thickness plays an important role: as thin the membrane as high the hydrogen permeance, even affecting the membrane mechanical resistance. Therefore, for real applications to ensure the

mechanical resistance and strength of the membrane, thicker membranes are necessary. They are generally deposited onto porous supports such as SiO_2, Al_2O_3, B_2O_3 and porous stainless steel (PSS).

Pd alloy membranes have been used in catalytic membrane reactors mainly for WGS and steam reforming reactions of methane and methanol [186], but their use in the steam reforming of ethanol is relatively new [187,188]. The main aim of the scientists and engineers involved in this field is oriented to emphasizing the role of the membrane by analyzing the performances of the reaction system in terms of ethanol conversion, hydrogen yield and hydrogen recovery, that is, the amount of hydrogen collected in the permeate side vs. the total hydrogen produced during the reaction. A large piece of work on ESR with Pd-Ag membranes (wall thickness of 50 μm) using sweep-gas has been carried out at the University of Calabria, Italy. [189] studied both methanol and ethanol steam reforming over Ru/Al_2O_3 catalyst in three different Pd-Ag membrane reactors. For ESR, the highest conversion attained at 723 K was about 50% in counter-current mode, which was significantly higher than that attained in a traditional reactor. However, in the CMR coke deposition occurred to a large extent with consequent deactivation of the catalyst. [176] used the same catalyst for performing ESR in a dense Pd-Ag CMR by varying the water:ethanol molar ratio between 3:1 and 9:1 at 573-673 K and 1.3 bar in counter current mode. Hydrogen recovery values of 22% were reached as well as ethanol conversion higher than 99% with a 56% hydrogen yield, which represent a significant improvement over the performance obtained with conventional catalytic reactors according to the shift effect. Over the same catalyst, [181] reached hydrogen yields as high as 80% working at 723 K and 2 bar using a dense thin wall Pd-Ag tube. The same device was used by [190] for studying Pt- and Ni-based catalysts, which showed a poor performance in terms of hydrogen yield with respect to the Ru-based catalyst (Ru>Ni>Pt at low feed, while for higher feed flow ratios the sequence was Ru>Ni=Pt). [191] also obtained kinetic expressions and modelled the CMR operation with the Ru-, Ni- and Pt-based catalysts in order to optimize the membrane reformer by assessing the ratio between the reaction and permeation kinetics. The effect of pressure was studied by [192] in a Pd-Ag tube of 150 mm wall thickness in the range 1-8 bar. At 723 K and 4 bar and a feed flow rate of 5 g h^{-1}, hydrogen recovery values close to 100% were

measured. The Ru/Al_2O_3 catalyst was also studied for the oxidative steam reforming of ethanol in the CMR at 673 K, S/C=5.5, GHSV=2000 h^{-1} and by using a sweep gas into the permeate side of the reactor [193], being the maximum hydrogen recovery (ca. 30%) achieved at O/C=1.2. The oxidative steam reforming of ethanol was studied by [194] over a Pt/Al_2O_3 catalyst in a membrane module with a finger-like configuration. The addition of oxygen had a positive effect on the performance of the CMR operating under pure ESR conditions. The behaviour of the CMR for the partial oxidation of ethanol over Rh/Al_2O_3 catalyst was studied by [195] at 723 K, 1-3 bar, GHSV=1300 h^{-1} and O/C=0.7-1.2. No carbon formation was detected and more than 40% hydrogen recovery was achieved. ESR over Co/Al_2O_3 catalyst was conducted by [196,197]. Several operational parameters such as temperature, pressure, sweep-gas flow (SF) and load were evaluated and hydrogen yield and recovery values as high as 60% and 95%, respectively, were reached at 673 K, 3 bar, SF=25.2 (countercurrent flow) and WHSV=0.2 h^{-1}. The same catalyst was tested at 673 K in a porous stainless steel (PSS) supported Pd membrane reactor with the aim of investigating the influence of the membrane characteristics as well as of the reaction pressure from 3 to 8 bar by [187]. Hydrogen recovery of about 50% was reached under complete ethanol conversion. Co/Al_2O_3 and Ni/ZrO_2 catalysts have been recently used in the PSS membrane reactor at 673 and 8-12 bar for simulating bio-ethanol steam reforming by using a mixture of water-ethanol-acetic acid and glycerol with 1:13:0.18:0.04 molar ratio [198]. About 94% of bio-ethanol conversion was obtained at 12 bar and GHSV=800 h^{-1} over the Co/Al_2O_3 catalyst, with 40% hydrogen yield and 40% hydrogen recovery.

Lin et al. from Chienkuo Technology University, Taiwan, studied the oxidative steam reforming of ethanol in a Pd-Ag/PSS membrane reactor (membrane thickness of 20 μm) loaded with $CuZn/Al_2O_3$ catalyst at 593-723 K and 3-10 bar [199]. The same study was conducted in a Ni-Pd-Ag ternary alloy membrane reactor with similar results [200]. [201] at Argonne National Laboratory, USA, explored the benefits of high-pressure ESR for the production of hydrogen needed to refuel the high-pressure tanks of PEMFC vehicles. The experiments were conducted at 7-70 bar, 873-1023 K, S/C=3-12 and GHSV=8500-83000 h^{-1} in a Pd-Ag (30 μm) CMR loaded with Rh/La_2O_3-Al_2O_3 catalyst. As expected from thermodynamics, higher pressures showed inhibition of the hydrogen yield in favour of

methane. In a recent work from the Technical University of Catalonia, the ESR was studied in a CMR over cobalt talc at 598-673 K and 5-15 bar [202]. In addition to an improvement of the hydrogen yield, the CMR showed a rapid response to changes in the ethanol-water mixture load; a constant hydrogen flow was obtained after 2s following variations of ±10%. The experiments of [201,202] were performed without sweep gas, therefore, pure hydrogen was obtained in the permeate side of the membrane, ready to feed a PEMFC. In a similar configuration, [203] studied recently the ESR using a Pd-Rh/CeO_2 catalyst over cordierite monoliths in-series into a stainless-steel membrane reactor. Reaction yields of 3.1 mol hydrogen generated per mol ethanol in feed and total yields of 1.4 mol H_2 permeated per mol ethanol in feed were measured, with maximum hydrogen recuperation of 70%.

Although most of the ESR work in CMR has been done with Pd-Ag selective membranes, there are also some examples of ESR in different types of membrane reactors with the scope of reducing the cost. Yu et al. from the Korea Research Institute of Chemical Technology used Pt-impregnated Knudsen membranes to carry out simultaneously the ESR reaction and WGS [204]. The ethanol reforming-membrane reactor showed ethanol conversion improvement up to ca. 15% in comparison with a conventional reactor, with an improvement of hydrogen yield up to 10.5%. A similar experiment was performed with a CMR loaded with Pt/TiO_2 catalyst, which showed hydrogen recovery values of 78-87% in the temperature range 573-873 K [205]. From the Virginia Polytechnic Institute & State University, USA, employed silica-alumina composite membranes with moderate hydrogen permeance for ESR over Na-Co/ZnO catalyst, more recently, Pd-Cu composite membranes over Al_2O_3 [206]. High-effective hydrogen production from ethanol and water has been recently reported in a tubular dense mixed-conducting oxygen permeable membrane reactor, in which the water splitting takes place at the tube side of the membrane and the oxidative steam reforming of ethanol occurs at the shell side simultaneously [207].

POE over Rh/Al_2O_3 in a dense Pd-Ag membrane reactor was evaluated working at 723 K, GHSV=1300 h^{-1}, O/E = 0.33-0.62 and reaction pressure range 1-3 bar [196]. Complete ethanol conversion was achieved in all the experimental tests, and in the best result more than 40.0% COx-free hydrogen recovery was achieved. The comparison between

the performances of Rh/CeO_2 catalyst in in this reactor and in a fixed bed reactor (FBR) highlights the benefits of using CMRs: using O/E = 0.5, full ethanol conversion and S_{H2} = 34% were achieved at 723 K in CMR, compared to 85 % ethanol conversion and S_{H2} = 60 % at much higher T_R = 973 K in FBR [208]. The activity of the Pd-Ag MR without catalyst was also tested. At stoichiometric O/ethanol ratio, the CMR presented around 85% ethanol conversion and around 11% H_2 selectivity (vs. 100 % and 33%, respectively, in the presence of Rh catalyst). However, the main drawback was carbon deposition (not observed with catalyst), which covered the Pd-Ag membrane surface and lowered its hydrogen permeation capacity.

1.9 Objectives

This PhD is devoted to the study of ethanol steam reforming processes aimed to produce hydrogen in catalytic wall reactors and catalytic membrane reactors over catalyst derived from cobalt hydrotalcites. The specific objectives are:

1. To determine the best catalytic formulation for ethanol steam reforming and oxidative steam reforming processes in terms of hydrogen yield and catalyst stability under practical conditions.

    1.1 To study the catalytic performance of several hydrotalcites with different Co:Mg:Al ratios loaded onto cordierite honeycombs.

    1.2 To study the catalytic performance of cobalt hydrotalcites promoted by noble metals, namely Pt and Rh, loaded onto cordierite honeycombs.

    1.3 To study the catalytic performance of cobalt hydrotalcites promoted by alkaline additives, namely K^+, loaded onto cordierite honeycombs.

    1.4 To conduct long stability tests with commercial bioethanol over catalytic honeycombs.

2. To characterize the catalysts before and after reaction as well as under reaction conditions by in-situ techniques to obtain valuable information about catalytic active sites for hydrogen evolution and catalyst deactivation.

    2.1 To determine the influence of the phases present in the catalyst and their structure.

    2.2 To determine the presence and influence of Co(0) vs. Co(II) in the reaction.

    2.3 To determine the influence of acidity and basicity.

3. To use dense metallic membranes with no sweep gas for the simultaneous generation and separation of hydrogen with fuel cell grade.

3.1 To study the influence of operational parameters, such as temperature, retentate pressure, steam to carbon ratio and reactants load.

3.2. To determine the best configuration in terms of hydrogen production between a staged disposition of the catalyst and membrane and an integrated disposition of the catalyst around the membrane.

1.10 References

[1] B. E. Logan, B. Hamelers, R. Rozendal, U. Schröder, J. Keller, S. Freguia, P. Aelterman, W. Verstraete, K. Rabaey, Environ. Sci. Technol., 40, (2006), 5181-5192.

[2] V. A. Goltsov, T. N. Veziroglu, L. F. Goltsova, Int. J. Hydrogen Energy. 31, (2005), 153-159.

[3] Spiro Thomas G. y Stigliani William M. Química Medioambiental. Capítulo 1. pp 3-18, Pearson. Educación, S.A. Madrid, España, (2004).

[4] European Commission (EU). Green Paper: Towards a European strategy for the security of energy supply. COM, 769 final, 2000. Office for Official Publications of the European Communities, Luxemburgo, (2012).

[5] International Energy Agency. World Energy Outlook (2004).

[6] Secretaría General de la Energía. La energía en España 2007. Ministerio de Industria, Turismo y Comercio, Madrid, (2006).

[7] European Commission (EU). Green Paper: A European Strategy for Sustainable, Competitive and Secure Energy. COM, 105 final, (2006).

[8] J.J. Brey, R. Brey, A.F. Carazo, I. Contreras, A.G. Hernández-Díaz, V. Gallardo, J. of Power Sources 159, (2006), 1231-1240.

[9] H. Liu, S. A. Cheng, B. E. Logan, Environ. Sci. Technol. 39, (2005), 658-662.

[10] J. Heilmann, B. E. Logan, Water Environ. Res., 78, (2006), 531-537.

[11] Paques bv http://en.paques.nl/, accesed March 2013.

[12] J.E. Logsdon, Ethanol, In Kirk-Othmer Encyclopedia of Chemical Engineering, 5th edition, A Seidel (ed.), Vol.10, (2004), 527-567. Wiley-Interscience, New York.

[13] H. Shapouri, J.A. Duffield, M. Wang, The Energy Balance of Corn Ethanol: An Update. AER-814. Washington, D.C.: USDA Office of the Chief Economist, (2002).

[14] H. Shapouri, J.A. Duffield, M. Wang, The Energy Balance of Corn Ethanol Revisited. Trans. of the ASAE, 46, (2003), 959-968.

[15] G. A. Deluga, J. R. Salge, L. D. Schmidt, X. E. Verykios, Renewable Hydrogen from Ethanol by Autothermal Reforming. Science, 303, (2004), 993-997.

[16] V. Subramani, C. Song, Advances in catalysis and process for hydrogen production from ethanol reforming, Catalysis, 20, (2007), 65-106.

[17] Renewable Fuels Asociation, World Fuel Ethanol Production, http://ethanolrfa.org/pages/World-Fuel-Ethanol-Production, accessed july 2012.

[18] M. Ni, D.Y.C. Leung, M.K.H. Leung, Int. J. Hydrogen Energy 32, (2007), 3238-3247

[19] M. Galbe, G.A. Zacchi, Appl. Microbiol. Biotechnol., 59, (2002), 618-628.

[20] J. Nowotny, C.C. Sorrell, L.R. Sheppard and T. Bak, Int. J. Hydrogen Energy. 30, (2004), 521–524.

[21] K. Vasudeva, N. Mitra, P. Umasankar, S.C. Dhingra, Steam reforming of ethanol for hydrogen production: Thermodynamic analysis, Int., (1996).

[22] L. F. Brown, Int. J. Hydrogen Energy, 26, (2001), 381–397.

[23] Murtagh & Associates 2012, Material Safety Sheet Ethanol, http://www.distill.com/materialsafety/msds-eu.html, accessed June 2012.

[24] S. Velu, N. Satoh, C.S. Gopinath, K. Suzuki, Catal. Lett. 82, (2002), 145-152.

[25] A. Casanovas, M. Saint-Gerons, F. Griffon, J. Llorca, Int. J. Hydrogen Energy, 33, (2008), 1827–1833.

[26] G. Rabenstein, V. Hacker, J. Power Sources, 185, (2008), 1293–1304.

[27] M. Benito, J.L. Sanz, R. Isabel, R. Padilla, R. Arjona, L. Daza, J Power Sources, 151, (2005), 11–17.

[28] A. Haryanto, S. Fernando, N. Murali, S. Adhikari, Energy Fuels, 19, (2005), 2098-2106.

[29] P.D. Vaidya, A.E. Rodrigues, Chem. Eng. J., 117, (2006), 39-49.

[30] K.L. Hohn, Y.C. Lin, ChemSusChem, 2, (2009), 927- 940.

[31] J. Llorca, V. Cortés, N.J. Divins, R. Olivera, E. Taboada, Hydrogen from Bioethanol. Renewable Hydrogen Technologies. Ed. L.M. Gandía, G. Arzamendi and P.M. Diéguez. Elsevier, (2013), chapter 7, 135-169.

[32] N. Bion, D. Duprez, F. Epron, ChemSusChem, 5, (2012), 76–84.

[33] F. Auprêtre, C. Descorme, D. Duprez, D. Casanave, D. Uzio, J. Catal., 233, (2005), 464-477.

[34] H. Idriss, M. Scott, J. Llorca, S. Chan, W. Chiu, P. Sheng, A. Yee, M. Blackford, S. Pas, A. Hill, F. Alamgir, R. Rettew, C. Petersburg, S. Senanayake, M. Barteau, ChemSusChem, 1, (2008), 905-910.

[35] S. Cavallaro, Energy F., 14, (2000), 1195-1199.

[36] F. Auprêtre, C. Descorme, D. Duprez, Catal. Commun. 3, (2002), 263-267.

[37] J. Breen, R. Burch, H. Coleman, App. Catal. B: Env. 39, (2002), 65-74.

[38] C. Diagne, H. Idriss, A. Kiennemann, Catal. Commun. 3, (2002), 565-571.

[39] F. Romero-Sarria, J. C. Vargas, A-C. Roger, A. Kiennemann, Catal. Today, 133-135, (2008), 149-153.

[40] M. Dömök, A. Oszko, K. Baan, I. Sarusi, A. Erdohelyi, App. Catal. A: Gen. 383, (2010), 33-42.

[41] D.K. Liguras, D. I. Kondarides, X.E. Verykios, App. Catal. B: Env. 43, (2003), 345-354.

[42] I. A. Ramos, T. Montini, B. Lorenzut, H. Troiani, F. Gennari, M. Graziani, P. Fornasiero, Catal. Today, 180, (2012), 96-104.

[43] B. Zhang, W. Cai, Y. Li, Y. Xu, W. Shen, Int. J. Hydrogen Energy 33, (2008), 4377-4386.

[44] J.-Y. Siang, C.-C. Lee, C.-H. Wang, W.-T. Wang, C.-Y. Deng, C.-T. Yeh, C.-B. Wang, Int. J. Hydrogen Energy 35, (2010), 3456-3462.

[45] M.C. Sanchez-Sanchez, R. Navarro Yerga, D. Kondarides, X. Verykios, J.L.G. Fierro, J. Phys. Chem. A, 114, (2010), 3873-3882.

[46] M. Scott, M. Goeffrey, W. Chiu, M. A. Blackford, H. Idriss, Topics Catal. 51, (2008), 13-21.

[47] H. Idriss, Ethanol reactions over the surfaces of noble metal/cerium oxide catalysts. Platinum Metals Rev. 48, (2004), 105-115.

[48] A. Simson, R. Farrauto, M. Castaldi, App. Catal. B: Environ. 106, (2011), 295-303.

[49] S. Cavallaro, Energy F., 14, (2000), 1195-1199.

[50] M. S. Scott, H. Idriss, Heterogeneous catalysis for hydrogen production, Handbook of green chemistry, (2010), 223-246.

[51] P. Ciambelli, V. Palma, A. Ruggiero, App. Catal. B: Environ. 96, (2010), 190-197.

[52] A. Birot, F. Epron, C. Descorme, D. Duprez, App. Catal. B: Environ. 79, (2008), 17-25.

[53] H.-S. Roh, Y. Wang, D. L. King, A. Platon, Y.-H. Chin, Catal. Lett. 108, (2006), 15-19.

[54] A. Trovarelli, Catal. Rev. Sci. Eng., 38, (1996), 439-520

[55] M. Dömök, K. Baán, T. Kecskés, A. Erdohelyi, Catal. Lett. 126, (2008), 49-57.

[56] S. De Lima, A. M. da Silva, G. Jacobs, B. H. Davis, L. V. Mattos, F. B. Noronha, New approaches to improving catalyst stability over Pt/ceria during ethanol steam reforming: Sn addition and CO2 co-feeding. App. Catal. B: Env. 96, (2010), 387-398.

[57] P. Yaseneva, S. PAvlova, V. Sadykov, G. Alikina, A. Lykashevich, V. Rogov, Belochapkine, J. Ross, Combinatorial approach to the preparation and characterization of catalysts for biomass steam reforming into syngas. Catal. Today, 137, (2008), 23-28.

[58] J. Kaspar, P. Fornasiero, A. Trovarelli, Catalysis by ceria and related materials, in : (Ed.), Catalytic science series, vol. 2, Imperial College Press, London, UK, (2002), 217.

[59] F. Can, A. Le Valant, N. Bion, F. Epron, D. Duprez, J. Phys. Chem. C. 112, (2008), 14145-14153.

[60] A. Le Valant, F. Can, N. Bion, D. Duprez, F. Epron, Int. J. Hydrogen Energy. 35, (2010), 5015-5020.

[61] A. Le Valant, A. Garron, N. Bion, F. Epron, D. Duprez, Catal. Today, 138, (2008), 169-174.

[62] A. Bshish, Z. Yahkkob, B. Narayanan, R. Ramakrishnan, A. Ebshish, Review. Chem. Papers 65, (2011), 251-266.

[63] Li, M.S., Wang, X.D., Li, S.R., Wang, S.P., Ma, X.B., Int. J. Hydrogen Energy, 35, (2010), 6699-6708.

[64] W. Wang, Int. J. Green Energy, 6, (2009), 92-103.

[65] Y. Yang, J. Ma, F. Wu , Int. J. Hydrogen Energy, 31, (2006), 877-882.

[66] F. Frusteri, S. Freni, V. Chiodo, L. Spadaro, O.Di Blasi, G. Bonura, S. Cavallaro, Applied Catalysis A: General 270, (2004), 1-7.

[67] J. Kugai, S. Velu, C. Song, Catal. Lett. 101, (2005), 255-264.

[68] M.H. Youn, J.G. Seo, P. Kim, J.J. Kim, H. Lee, I.K. Song, J. Power Sources 162, (2006), 1270-1274.

[69] M.H. Youn, J.G. Seo, P. Kim, I.K. Song, J. Mol. Catal. A: Chem, 261, (2007), 276-281.

[70] A.J. Vizcaino, A. Carrero, J.A. Calles, Catal. Today 146, (2009), 63-70.

[71] A.J. Vizcaino, P. Arena, G. Baronetti, A. Carrero, J.A. Calles, M.A. Laborde, N. Amadeo, Int. J. Hydrogen Energy, 33, (2008), 3489-3492.

[72] A. Carrero, J.A. Calles, A.J. Vizcaino, Chem. Eng. J., 63, (2010), 395-402.

[73] C. Zhang, S. Li, M. Li, S. Wang, X. Ma, J. Gong, AlChE J., 58, (2012), 516-525.

[74] C.K.S. Choong, L. Huang, Z. Zhong, L. Jianyi, L. Hong, L. Chen, Applied Catal. A: General, 407, (2011), 155-162.

[75] F. Haga, T. Nakajima, H. Miya, S. Mishima, Catal. Lett. 48, (1997), 223-227.

[76] S. Cavallaro, N. Mondello, S. Freni, J. Power Sources 102, (2001), 198-204.

[77] J. Llorca, N. Homs, J. Sales, P. Ramírez de la Piscina, J. Catal. 209, (2002), 306-317.

[78] A. Kaddouri, C. Mazzocchia, Catal. Commun. 5, (2004), 339-345.

[79] M.S. Batista, R.K.S. Santos, E.M. Assaf, J.M. Assaf, , E.A. Ticianelli, High efficiency steam reforming of ethanol by cobalt-based catalysts. J. Power Sources 134, (2004), 27-32.

[80] J. Llorca, J. A. Dalmon, P. Ramírez de la Piscina, N. Homs, Appl. Catal. A:Gen. 243, (2003), 261-269.

[81] J. Llorca, P. Ramírez de la Piscina, J. A. Dalmon, J. Sales, N. Homs, Appl. Catal. B: Environ. 43, (2003), 355-369.

[82] J. Llorca, N. Homs, P. Ramírez de la Piscina, J. Catal. 227, (2004), 556-560.

[83] E. Martono, M.P. Hyman, J.M. Vohs, Phys. Chem. Chem. Phys. 13, (2011), 9880-9886.

[84] A.M. Karim, Y. Su, M.H. Engelhard, D.L. King, Y. Wang, ACS Catal. 1, (2011), 279-286.

[85] M.P. Hyman and J.M. Vohs, Surf. Sci. 605, (2011), 383-389.

[86] D.R.Sahoo, S. Vajpai, S. Patel, K.K. Pant, Chem. Eng. J., 125, (2007), 139-147.

[87] A.M. Karim, Y. Su , J. Sun, C. Yang, J.J. Strohm, D.L. King, Y. Wang, Appl. Catal. B: Environ. 96, (2010), 441-448.

[88] H. Song, U.S. Ozkan, J. Phys. Chem. A 114, (2010), 3796-3801.

[89] J. Llorca, P. Ramírez de la Piscina, J. A. Dalmon, N. Homs, Chem. Mater. 16, (2004), 3573-3578.

[90] B. Bayram, I.I. Soykal, D. von Deak, J.T. Miller, U.S. Ozkan, J. Catal. 284, (2011), 77-89.

[91] S.S.Y. Lin, D.H. Kim, S.Y. Ha, Appl. Catal. A:Gen. 355, (2009), 69-77.

[92] P. Bichon, G. Haugom, H.J. Venvik, A. Holmen, E.A. Blekkan, Topics Catal. 49, (2008), 38-45.

[93] H. Wang, Y. Liu, L. Wang, Y.N. Qin, Chem. Eng. J. 145, (2008), 25-31.

[94] J. Llorca, N. Homs, J. Sales, J. L. G. Fierro, P. Ramírez de la Piscina, J. Catal. 222, (2004), 470-480.

[95] K.S. Kim, H.R. Seo, S.Y. Lee, J.G. Ahn, W.C. Shin, Y.K. Lee, Topics Catal. 53, (2010), 615-620.

[96] A.E. Galetti, M.F. Gómez, L.A. Arrua, A.J. Marchi, M.C. Abelló, Catal. Commun. 9, (2008), 1201-1208

[97] J. A. Torres, J. Llorca, A. Casanovas, M. Domínguez, J. Salvadó, D. Montané, J. Power Sources 169, (2007), 158-166.

[98] A. Casanovas, C. de Leitenburg, A. Trovarelli, J. Llorca, Chem. Eng. J. 154, (2009), 267-273.

[99] A. Casanovas, M. Roig, C. de Leitenburg, A. Trovarelli, J. Llorca, Int. J. Hydrogen Energy 35, (2010), 7690-7698.

[100] Y. Sekine, A. Kazama, Y. Izutsu, M. Matsukata, E. Kikuchi, Catal. Lett. 132, (2009), 329-334.

[101] A. Kazama, Y. Sekine, K. Oyama, M. Matsukata, E. Kikuchi, Appl. Catal. A:Gen. 383, (2010), 96-101.

[102] H. Song, U.S. Ozkan, J. Catal. 261, (2009), 66-74.

[103] H. Song, X. Bao, C.M Hadad, U.S. Ozkan, Catal. Lett. 141, (2011), 43-54.

[104] S. De Lima, R. Colman, G. Jacobs, B.H. Davis, K. R. Souza, A. F. F. de Lima, L. G. Appel, L. V. Mattos, F. B. Noronha, Catal. Today, 146, (2009), 110-123.

[105] C.N. Avila-Neto, J.W.C. Liberatori, A.M. da Silva, D. Zanchet, C.E. Hori, F.B. Noronha, J.M.C. Bueno, J. Catal. 287, (2012), 124-137.

[106] P. Rybak, B. Tomaszewska, A. Machocki, W. Grzegorczyk, A. Denis, Catal. Today 176, (2011), 14-20.

[107] V.M. Lebarbier, A.M. Karim, M.H. Engelhard, Y. Wu, B.Q. Xu, E.J. Petersen, A.K. Datye, Y. Wang, ChemSusChem 4, (2011), 1679-1684.

[108] S.S.Y. Lin, H. Daimon, S.Y. Ha, Appl. Catal. A:Gen. 366, (2009), 252-261.

[109] M. Benito, R. Padilla, A. Serrano-Lotina, L. Rodríguez, J.J. Brey, L. Daza, J. Power Sources 192, (2009), 158-164.

[110] L.P.R. Profeti, E.A. Ticianelli, E.M. Assaf, Appl. Catal. A:Gen., 360, (2009), 17-25.

[111] M. R. Othmana, Z. Helwania, and W. J. N. Fernando, App. Organometallic Ch., 23, (2009), 335-346.

[112] H. H. Kung, E. I. Ko, Chem. Eng. J., 64 (1996), 203-214.

[113] F. Cavani, F. Trifiro, A. Vaccari, Catal. Today, 11, (1991), 173-301.

[114] A. de Roy, C. Forano, K. El Malki, J. P. Besse, Synthesis of Microporous Materials , Van Nostrand-Reinhold: New York, (1992), 108–169.

[115] F. Trifiro, A. Vaccari, Comprehensive Supramolecular Chemistry, Solid State Supramolecular Chemistry: Two and Three-dimensional Inorganic Networks, Pergamon: Oxford, (1996), 251–291.

[116] A. Vaccari, Catal. Today (1998), 41-53.

[117] V. Rives,M. A. Ulibarri, Coord. Chem. Rev., 9, (1999), 1033-1039.

[118] W. Kagunya, Z. Hassan,W. Jones, Inorg. Chem.,35, (1996), 5970-5974.

[119] V. Rives (Ed.), Layered Double Hydroxides: Present and Future, Nova Science: New York, (2001), 251–411.

[120] S. M. Auerbach, K. A. Carrado, P. K. Dutta, Handbook of Layered Materials, Marcel Dekker: New York, (2004).

[121] X. Duan, D. G. Evans (Ed.), Layered Double Hydroxides, Structure and Bonding Series, Springer: Berlin, (2006).

[122] A. De Roy, C. Forano, J. P. Besse, Layered Double Hydroxides: Present and Future (Ed.: V. Rives), Nova Science: NewYork, (2001), 1–37.

[123] J. He, M. Wei, Y. Kang, B. Li,D. G. Evans, X.Duan, Struct, Bond,119, (2006), 1-87.

[124] H. P. Boehm, J. Steinle, C. Vieweger, Angew. Chem. Int. Ed. Engl.,16 (1977), 265.

[125] R. M. Taylor, Clay Mineral,19, (1984), 591-603.

[126] M. A. Dredzon, Inorg. Chem., 27 (1988), 4628-4633.

[127] H. Nijs, A. Clearfield, E. F. Vansant, Microp. Mesop. Mater., 23, (1998), 97-108.

[128] M. A. Aramendia, V. Borau, C. Jimenez, J. M. Marinas, J. R. Ruiz, F. J. Urbano, J. Solid State Chemistry, 168, (2002), 156-161.

[129] Y. Zhao, F. Li, R. Zhang, D. G. Evans, X. Duan, Chem. Mater., 14, (2002), 4286-4291.

[130] R. L. Goswamee, P. Sengupta, K. G. Bhattacharyya, D. K. Dutta, Appl. Clay Sci., 13, (1998), 21-34.

[131] P. C. Pavan, G. A. Gomes, J. B. Valim, Micro. Meso. Mater., 21, (1998), 21, 4-6.

[132] H. S. Shin, M. J. Kim, S. Y. Nam, H. C. Moon, Water Sci. and Technology, 34, (1996), 161-168.

[133] Y. Ding, E. Alpay, Chem. Eng. Sci., 55, (2000), 3461-3474.

[134] Z. Yong, V. Mata, A. E. Rodrigues, Ind. Eng.Chem.Res., 40, (2001), 204-209.

[135] A. Alejandre, F. Medina, X. Rodriguez, P. Salagre, Y. Cesteros, J. E. Sueiras, Appl. Catal. B: Environ., 30, (2001), 195-207.

[136] K. Bahranowski, G. Bueno, V. C. Corberan, F. Kooli, E. M. Serwicka, R. X. Valenzuela, K. Wcislo, Appl. Catal. A: Gen., 185, (1999), 65-73.

[137] E. Gardner, T. J. Pinnavaia, Appl. Catal. A: Gen., 167, (1998), 65-74.

[138] S. M. Auer, J. D. Grunwaldt, R. A. Koppel, A. Baiker, J. Mol. Catal. A: Chem., 139, (1999), 305-313

[139] F. Malherbe, C. Depege, C. Forano, J. P. Besse, M. P. Atkins, B. Sharma, S. R. Wade, Appl. Clay Sci., 13, (1998), 451-466.

[140] J. Santhanalakshmi, T. Raja, Appl. Catal. A: Gen., 147, (1996), 69-80.

[141] K. T. Liu Paul, Gas Separation Using Membrane Organic. Media and Process Technology Inc.: 2002.

[142] W. J. Onstot, T. T. Tsotsis, R. G. Minot, Ind. Eng. Chem. Res., 40, (2001), 242-251.

[143] Y. Ding, E. Alpay, Chem. Eng. Sci., 55, (2000), 3929-3940.

[144] S. Sircar, M. B. Rao, AIChE J., 45, (1999), 2326-2332.

[145] J. W. Wang, A. G. Kalinichev, R. J. Kirkpatrick, X. Q. Hou, Chem. Mater., 13, (2001), 145-150.

[146] X. D. Wang, Q. Zhang, Polym. Int., 53, (2004), 698-707.

[147] G. Camino, A. Maffezzoli, M. Braglia,M. D. Lazzaro,M. Zammarano, Polym. Degrad. Stab., 74, (2001), 457-464.

[148] A. Ookubo, K. Ooi, H. Hayashi, J. Pharm. Sci., 81, (1992), 1139-1140.

[149] M. Del Arco, E. Cebadera, S. Gutiérrez, C. Martín, M. J. Montero, V. Rives, J. Rocha, M. A. Se villa, J. Pharm. Sci., 93, (2004), 1649-1658.

[150] D. Meloni, R. Monaci, V. Solinas, A. Auroux, E. Dumitriu, Appl. Catal A: Gen., 350, (2008), 86-95.

[151] A. Vaccari, Appl. Clay Sci., 14, (1999), 161-198.

[152] S. Casenave, H. Martinez, C. Guimon, A. Auroux, V. Hulea, E. Dumitriu, J. Therm. Anal. Cal., 72, (2003), 191-198.

[153] B. M. Nagaraja, V. Siva Kumar, V. Shashikala, A. H. Padmasri, S. S. Reddy, B. D. Raju, K. S. R. Rao, J. Mol. Catal. A: Chem., 223, (2004), 313-319.

[154] M. Crivello, C. Perez, E. Herrero, E. Ghione, S. Casuscelli, E. Rodrıguez-Castellon, Catal. Today, 107, (2005), 215-222.

[155] M. J. Climent, A. Corma, S. Iborra, A. Velty, J. Catal., 221, (2004), 316-326.

[156] M. J. Climent, A. Corma, S. Iborra, A. Velty, J. Mol. Catal. A: Chem., 327, (2002), 182-183.

[157] J. Sanchez Valente, F. Figueras, M. Gravelle, P. Kumbhar, J. Lopez, J. P. Besse, J. Catal., 189, (2000), 370-381.

[158] A. L. McKenzie, C. T. Fishel, R. J. Davis, J. Catal., 138, (1992), 547-561.

[159] J. I. Di Cosimo, V. K. Diez, M. Xu, E. Iglesia, C. R. Apesteguıa, J. Catal., 178, (1998), 499-510.

[160] F. Prinetto,G. Ghiotti,P. Graffin, D. Tichit, Micropor.Mesopor.Mater., 39, (2000), 229-233.

[161] V. K. Díez, C. R. Apesteguía, J. I. Di Cosimo, J. Catal., 215, (2003), 220-233.

[162] S. Casenave, H. Martinez, C. Guimon, A. Auroux, V. Hulea, A. Cordoneanu, E. Dumitriu, Thermochim. Acta., 379, (2001), 85-93.

[163] O. Bergada, I. Vicente, P. Salagre, Y. Cesteros, F. Medina, J. E. Sueras, Micro. Meso. Mater., 101, (2007), 363-373.

[164] C. N. Perez, C. A. Perez, C. A. Henriques, J. L. F. Monteiro, Appl. Catal. A: Gen., 272, (2004), 229-240.

[165] S. Abello, F. Medina, D. Tichit, J. Perez-Ramırez, Y. Cesteros, P. Salagre, J. E. Sueiras, Chem. Commun., 11, (2005), 1453-1455.

[166] S. Abello, F. Medina, D. Tichit, J. Perez-Ramırez, J. C. Groen, J. E. Sueiras, P. Salagre, Y. Cesteros, Chem. Eur. J., 11, (2005), 728-739.

[167] P. Kumbhar, J. Sanches Valente, J. Lopes, F. Figueras, J. Chem. Soc. Chem. Commun. (1998), 535-541.

[168] M. A. Aramendia, V. Borau, C. Jimenez, J. M. Marinas, J. R. Ruiz, F. J. Urbano, Appl. Catal. A: Gen., 206, (2001), 95-102.

[169] K. Yamaguchi, K. Ebitami, K. Kaneda, J. Org. Chem., 64, (1999), 4526-4527.

[170] D. Tichit, B. Coq, Cattech, 7, (2003), 206-217.

[171] J. Shen, M. Tu, C. Hu, J. Solid State Chem., 137, (1998), 295-301.

[172] C. O. Veloso, C. N. Perez, B. M. de Souza, E. C. Lima, A. G. Dias, A. J. F. Monteiro, C. A. Henriques, Micro Meso. Mater., 107, (2008), 23-29.

[173] M. Domínguez, E. Taboada , E. Molins , J. Llorca, Catal. Today, 138, (2008), 193-197.

[174] R. Nedyalkova, A. Casanovas, J. Llorca, D. Montané, Int. J. Hydrogen Energy, 34, (2009), 2591-2599.

[175] F. Gallucci, A. Basile, Int. J. Hydrogen Energy 33, (2008), 1671-1687.

[176] A. Basile, Top. Catal. 51, (2008), 107-122.

[177] D. Mendes, S. Tosti, F. Borgognoni, A. Mendes, L.M. Madeira, Catal. Today, 156, (2010), 107-117.

[178] S. Tosti And L. Bettinali, J. Mater. Sci. 39, (2004), 3041-3046.

[179] S. Tosti, A. Basile, L. Bettinali, F. Borgognoni, F. Chiaravalloti, F. Gallucci, J. Membrane Sci. 284, (2006), 393-397.

[180] H.D. Tong, F.C. Gielens, J.G.E. Gardeniers, H.V. Jansen, C.J.M. van Rijn, M.C. Elwenspoek, W. Nijdam, Ind. Eng. Chem. Res. 43, (2004), 4182-4187.

[181] S. Tosti, A. Basile, L. Bettinali, F. Borgognoni, F. Gallucci, C. Rizello, Int. J. Hydrogen Energy 33, (2008), 5098-5105.

[182] G.S. Burkhanov, N.B. Gorina, N.B. Kolchugina, N.R. Roshan, Platinum Metals Rev. 55, (2011), 3-12.

[183] D. Montané, E. Bolshak, S. Abelló, Chem. Eng. J. 175, (2011), 519-533.

[184] F. Gallucci, M. Van Sint Annaland, J.A.M. Kuipers, Int. J. Hydrogen Energy 35, (2010), 1659-1668.

[185] H. Gao, Y.S. Lin, Y. Li, B. Zhang, Ind. Eng. Chem. Res. 43, (2004), 6920-6930.

[186] A. Basile, F. Gallucci, A. Iulianelli, S. Tosti, Fuel Cells 8, (2008), 62-68.

[187] A. Basile, P. Pinacci, A. Iulianelli, M. Broglia, F. Drago, S. Liguori, T. Longo, V. Int. J. Hydrogen Energy 36, (2011), 2029-2037.

[188] A.Iulianelli, A. Basile, Catal. Sci. Technol. 1, (2011), 366-379.

[189] F. Gallucci, A. Basile, S. Tosti, A. Iulianelli, E. Drioli, Int. J. Hydrogen Energy 32, (2007), 1201-1210.

[190] S. Tosti, A. Basile, F. Borgognoni, V. Capaldo, S. Cordiner, S. Di Cave, F. Gallucci, C. Rizzello, A. Santucci, E. Traversa, J. Membrane Sci. 308, (2008), 250-257.

[191] S. Tosti, A. Basile, R. Borelli, F. Borgognoni, S. Castelli, M. Fabbricino, F. Gallucci, C. Licusati, Int. J. Hydrogen Energy 34, (2009), 4747-4754.

[192] S. Tosti, M. Fabbricino, A. Moriani, G. Agatiello, C. Scudieri, F. Borgognoni, A. Santucci, J. Membrane Sci. 377, (2011), 65-74.

[193] A. Iulianelli, T. Longo, S. Liguori, P.K. Seelam, R.L. Keiski, A. Basile, Int. J. Hydrogen Energy 34, (2009), 8558-8565.

[194] A. Santucci, M.C. Annesini, F. Borgognoni, L. Marrelli, M. Rega, S. Tosti, Int. J. Hydrogen Energy 36, (2011), 1503-1511.

[195] A. Iulianelli, S. Liguori, V. Calabrò, P. Pinacci, A. Basile, Int. J. Hydrogen Energy 35, (2010), 12626-12634.

[196] A. Iulianelli, A. Basile, Int. J. Hydrogen Energy 35, (2010), 3170-3177.

[197] A. Iulianelli, S. Liguori, T. Longo, S. Tosti, P. Pinacci, A. Basile, Int. J. Hydrogen Energy 35, (2010), 3159-3164.

[198] P.K. Seelam, S. Liguori, A. Iulianelli,P. Pinacci, V. Calabrà, M. Huuhtanen, R. Keiski, V. Piemonte, S. Tosti, M. de Falco, A. Basile, Catal. Today, 193, (2012), 42-48.

[199] W.H. Lin, C.S. Hsiao, H.F. Chang, J. Membrane Sci., 322, (2008), 360-367.

[200] W.H. Lin, Y.C. Liu, H.F. Chang, Int. J. Hydrogen Energy 35, (2010), 12961-12969.

[201] D.D. Papadias, S.H.D. Lee, M. Ferrandon, S. Ahmed, Int. J. Hydrogen Energy 35, (2010), 2004-2017.

[202] M. Domínguez, E. Taboada, E. Molins, J. Llorca, Catal. Today, 193, (2012), 101-106

[203] E. López, N.J. Divins, J. Llorca, Catal. Today, 193, (2012), 145-150.

[204] C.Y. Yu, D.W. Lee, S.J. Park, K.Y. Lee, K.H. Lee, Appl. Catal. B: Environ. 86, (2009),121-126.

[205] C.Y. Yu, D.W. Lee, S.J. Park, K.Y. Lee, K.H. Lee, Int. J. Hydrogen Energy 34, (2009), 2947-2954.

[206] H. Lim, Y. Gu, S.T. Oyama, J. Membrane Sci. 351, (2010), 149-159.

[207] N. Zhu, X. Dong, Z. Liu, G. Zhang, W. Jin, N. Xu, Chem. Comm., 48, (2012), 7137-7139.

[208] J.R. Salge, G.A. Deluga, L.D. Schmidt, J. Catal., 235, (2005), 69-78.

CHAPTER 2

Cobalt hydrotalcite for the steam reforming of ethanol with scarce carbon production

Partially published in:

"Cobalt hydrotalcite for the steam reforming of ethanol with scarce carbon production"

Raúl Espinal, Elena Taboada, Elies Molins, Ricardo J. Chimentao, Francesc Medina and Jordi Llorca

RSC Advances, 2, (2012), 2946–2956.

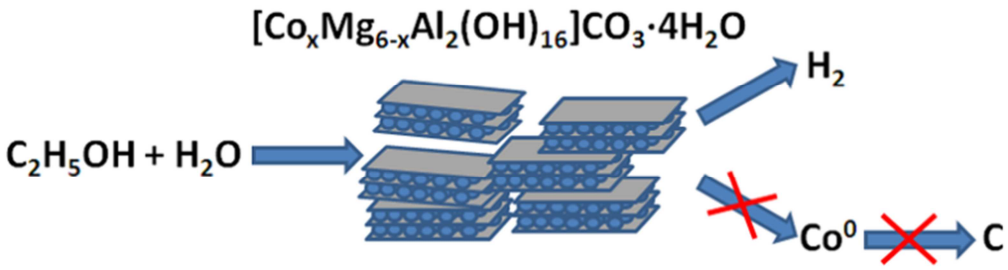

2.1 Introduction

Ethanol is nowadays a well-established source of hydrogen via catalytic steam reforming, oxidative reforming or partial oxidation processes. Numerous reviews have been published in the last years, covering both catalytic aspects and fuel reformer concepts [1-5]. Ethanol has the advantage over other conventional substrates such as natural gas, gasoline or liquefied petroleum gas (LPG) that it is readily available, easy to obtain from biomass, almost CO_2-neutral (bioethanol), safe to handle and can be processed at low temperature to obtain hydrogen. Among the different processes for hydrogen production, including those outlined above, as well as CO_2 sorption enhanced routes, ethanol steam reforming (ESR) is the simplest for implementation and yields more hydrogen, since part of it comes from water (eq. 2.1).

$$C_2H_5OH + 3\ H_2O \rightarrow 6\ H_2 + 2\ CO_2 \qquad (2.1)$$

The drawback of ESR, however, is thermal management. Steam reforming reactions are strongly endothermic and require a continuous supply of heat. In ethanol reformers, this can be provided by a combination of direct and catalytic combustion of ethanol and by burning the anode off-gas of a fuel cell [4, 6]. Therefore, it is desirable to develop catalysts for low-temperature ESR to optimize thermal management in addition to build long life and safe reformers that can be used for portable applications. A survey of the literature reveals that noble metal-based catalysts perform well for ESR [1-3, 7, 8]. They are stable and exhibit high activity, but only at high temperature (> 900 K). The reason is that the reaction mechanism involves the decomposition of ethanol at low temperature into a mixture of hydrogen, carbon monoxide and methane (eq. 2.2), followed by the water gas shift reaction (WGS) at intermediate temperature (eq. 2.3) and, finally, the steam reforming of methane at high temperature (eq. 2.4)[9].

$$C_2H_5OH \rightarrow H_2 + CO + CH_4 \qquad (2.2)$$

$$CO + H_2O \leftrightarrows H_2 + CO_2 \qquad (2.3)$$

$$CH_4 + 2\ H_2O \leftrightarrows 4\ H_2 + CO_2 \qquad (2.4)$$

In order to carry out ESR at low temperature, a different type of catalyst is required; in particular, a catalyst that does not yield methane as an intermediate species in the reaction mechanism, which can only be reformed at high temperature. Relatively inexpensive cobalt catalysts fulfill this requirement [10-32]. Over cobalt-based catalysts, ethanol is first dehydrogenated into a mixture of hydrogen and acetaldehyde (eq. 2.5), and acetaldehyde reacts with steam to yield mainly hydrogen and carbon oxides (eq. 2.6) [33, 34]. Given the lower temperature of the overall process, the WGS equilibrium (eq. 2.3) favors the hydrogen yield.

$$C_2H_5OH \rightarrow H_2 + CH_3CHO \quad (2.5)$$

$$CH_3CHO + H_2O \rightarrow 3\ H_2 + 2\ CO \quad (2.6)$$

However, and in contrast to noble metal-based systems, cobalt catalysts suffer from severe deactivation during ESR due to extensive carbon deposition. In situ infrared spectroscopy experiments [35], in situ magnetic measurements [33, 36] and in situ X-ray photoelectron spectroscopy experiments [13] have revealed that Co metal particles are formed under reaction conditions, which rapidly detach from the catalyst support and originate carbon nanotubes and carbon nanofibers. At the same time, methane selectivity increases at the expense of the reforming products (H_2 and CO_x) and the initial catalytic performance is not recovered after regeneration. In this work, we report the catalytic performance of ceramic honeycombs coated with Co/Mg/Al hydrotalcites for performing ESR at moderate temperature with scarce carbon formation. Hydrotalcite precursors have already been used for the synthesis of catalysts suitable for ethanol reforming reactions. In most cases nickel hydrotalcites have been used for ESR, and only a few examples of cobalt hydrotalcites exist, but no details about stability and coke formation have been reported under high ethanol loads [37-39].

A detailed characterization has been carried out by using X-ray diffraction (XRD), scanning electron microscopy (SEM-EDX), high resolution transmission electron microscopy (HRTEM), magnetic measurements and temperature-programmed techniques (TGA, DSC and TPR) as well as in situ X-ray photoelectron spectroscopy (XPS), which show that no metallic cobalt is detected under ESR conditions and, therefore, cobalt ions are catalytically active. We have used catalytic honeycombs instead of

conventional powdered or pelletized samples because they are robust, easy to scale up and replace, and offer homogeneous flow distribution patterns with low pressure drop, which constitute critical aspects for the development of fuel reformers [4, 11, 14, 40, 41].

2.2 Experimental

2.2.1 Catalyst preparation

Co/Mg/Al hydrotalcites with Co:Mg:Al molar ratios of 0.5:2.5:1, 1:2:1 and 2:1:1 were prepared by co-precipitation at constant pH (10±0.2) by adding an aqueous solution of $NaOH/Na_2CO_3$ (2 M) onto an aqueous solution of $CoCl_2{\cdot}6H_2O$, $Mg(NO_3)_2{\cdot}6H_2O$ and $Al(NO_3)_3{\cdot}9H_2O$. Both solutions were mixed dropwise under stirring at 298 K. The slurry was aged at 298 K for 15 h under vigorous stirring and the resulting precipitate was filtered and thoroughly washed with deionized water. The solids were dried at 373 K for 18 h to yield the as-synthesized samples. The co-precipitation method allows preparing hydrotalcites with a given metallic contain, since there is no loss of metallic salt during the process. In this sense, these hydrotalcites have the nominal formulae $[CoMg_5Al_2(OH)_{16}]CO_3{\cdot}4H_2O$, $[Co_2Mg_4Al_2(OH)_{16}]CO_3{\cdot}4H_2O$ and $[Co_4Mg_2Al_2(OH)_{16}]CO_3{\cdot}4H_2O$ and are named from now on as 0.5/2.5/1_as, 1/2/1_as and 2/1/1_as, respectively.

2.2.2 Catalytic honeycombs preparation

The as-synthesized hydrotalcites were deposited onto cordierite supports (400 cells per square inch) by the washcoating method. Two different commercial honeycombs were used from Rauschert and Corning companies, with similar chemical composition ($Al_3Mg_2AlSi_5O_{18}$). They were cut into cylindrical pieces of 1.8 cm in diameter and 2 cm long. Two different binding agents were tested for coating the honeycombs with the as-synthesized hydrotalcites: a 2:1 mixture of methoxyethanol and monoethanolamine [42] and a 5:1 mixture of polyvinyl alcohol (PVA) and acetic acid [43]. The resulting catalytic honeycombs were dried at 363 K for 2 hours and calcined at 823 K for 3 hours. The

adherence of the catalytic coatings onto the cordierite walls was checked by immersing the catalytic honeycombs in an ultrasonic bath and monitoring the weight loss for 5, 10, 15, 20, 25 and 30 seconds. Significant differences were encountered, being more stable the catalytic honeycombs prepared with the PVA binding agent over Rauschert substrates (22.5 wt.% loss after 30 s of ultrasound exposure). To better characterize the microstructure of the catalytic coatings, the hydrotalcites were calcined in powder form as well, following exactly the same procedure. These samples were named 0.5/2.5/1_calc, 1/2/1_calc and 2/1/1_calc.

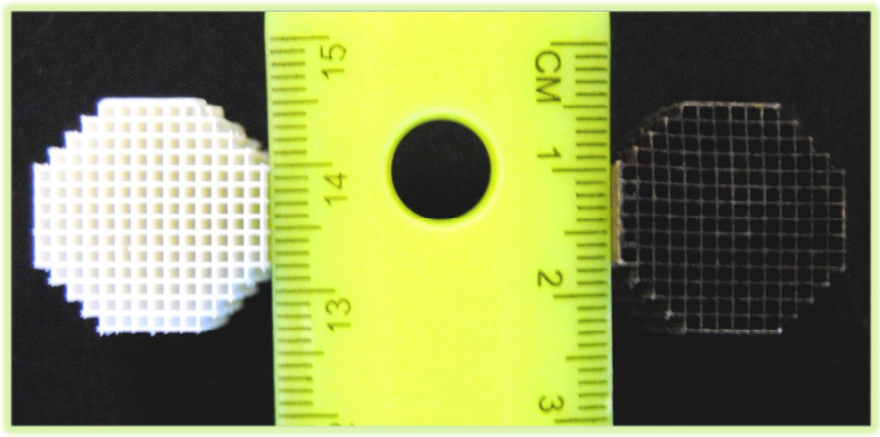

Fig. 2.1 Honeycombs before (left) and after (right) washcoat

2.2.3 Catalytic tests

Ethanol steam reforming was carried out in the temperature range 523-823 K at atmospheric pressure in a tubular stainless-steel reactor over the as-synthesized honeycombs without any pretreatment. The reaction was tested with a gaseous H_2O:CH_3CH_2OH=4:1 molar mixture (steam to carbon, S/C=2) provided directly with a Knauer Smartline HPLC pump (the liquid mixture was vaporized at 450 K before entering the reactor), or by using a nitrogen stream saturated with the reactants. VHSV values ranged from 420 to 660 h^{-1} and W/F values ranged from 390-10^4 $g \cdot min/mol_{EtOH}$. The reactor effluent was monitored on-line every 5 minutes by gas chromatography (Agilent 3000 A) using MS 5 Å, Plot U and Stabilwax columns. Stability tests were conducted at

823 K with pure liquid mixture. On the other hand, 0.5/2.5/1_calc, 1/2/1_calc and 2/1/1_calc powder samples were subjected to ESR at 823 K for 7 h in a similar manner and the resulting samples were labeled as 0.5/2.5/1_reac, 1/2/1_reac and 2/1/1_reac and used for characterization.

2.2.4 Characterization techniques

Powder X-ray diffraction (XRD) patterns of the powder catalysts were collected between 5 and 70^{o} 2θ, at a step width of 0.02^{o} and a step time of 1 s using a Bruker D8 instrument equipped with a Cu target and a graphite monochromator. Magnetization (M) vs. applied magnetic field (H) (at 5 and 298 K) and ZFC-FC curves (at 50 Oe) were measured with a superconducting quantum interference device (SQUID) magnetometer (Quantum Design MPMS5XL, USA). A given amount of powder was confined in a gelatin capsule (of known mass) and pressed with a given amount of cotton to avoid the powder from moving during the measurement. The diamagnetic contribution of the capsule and the cotton was subtracted from the total magnetization (m_{total}) as follows:

$$M_{powder}\left(\frac{emu}{g}\right) = \frac{m_{total}(emu) - (\chi_{capsule} \cdot mass_{capsule} + \chi_{cotton} \cdot mass_{cotton})}{mass_{powder}(g)} \qquad (2.7)$$

where χ is the magnetic susceptibility in cgs units: χ(capsule)=-3.39·10^{-7} emu·g^{-1}Oe^{-1} and χ(cotton)=-7.79·10^{-7} emu·g^{-1}Oe^{-1}.

Thermogravimetric analysis (TGA) was accomplished with a Netzsch STA 449 F1 Jupiter analyzer. Differential scanning calorimetry (DSC) was performed on a DSC 8500 Perkin Elmer. Heating rate was fixed at 10 K·min^{-1}, from room temperature to 1173 K, both under argon and under air. Temperature programmed reduction (TPR) was performed in a Catalyst Analyzer BELCAT-M (BEL Japan, Inc.), equipped with a water trap and a thermal conductivity detector (TCD). Prior to each TPR run, samples were heated up to 823 K (10 K·min^{-1}) and cooled down to room temperature under argon. Then they were analyzed by heating up to 1173 K (10 K·min^{-1}) using hydrogen (10 vol% in argon) under a flow rate of 30 ml·min^{-1}. The morphologies of the catalysts were observed by SEM with a Neon40 Crossbeam Station (Zeiss) equipped with a field emission electron source and an

energy dispersing X-ray dispersive (EDX). A small portion of each sample powder was deposited on a metallic disk holder and covered with a thin gold layer before SEM analysis. High resolution transmission electron microscopy (HRTEM) was conducted on a JEOL 2010F microscope operating at 200kV and equipped with a field emission electron source. The point-to-point resolution of the instrument was 0.19 nm and the resolution between lines was 0.14 nm. Samples were dispersed onto holey-carbon grids from alcohol suspensions.

Infrared spectra were collected using a Shimadzu FTIR 8400S spectrometer (resolution 2 cm^{-1}). X-ray photoelectron spectroscopy (XPS) was performed with a SPECS system equipped with an Al anode XR50 source operating at 150 W and a Phoibos 150 MCD-9 detector. Sample powders were pressed to pellets and then fixed into a special sample holder (no glue was used). Spectra were recorded with pass energy of 25 eV at 0.1 eV steps at a pressure below $6 \cdot 10^{-9}$ mbar; binding energies were referred to the adventitious C 1s signal. The apparatus was equipped with an additional high pressure cell (HPC-20) for in situ treatments that, in addition to calcination and reduction treatments, allowed reproducing ESR conditions, too. An Ametek mass spectrometer connected to the high pressure cell was used to monitor the reaction products to ascertain that the in situ XPS experiments reproduced those performed over the catalytic honeycombs during the conventional ESR tests. Experiments were carried out at 1 bar and temperature was provided with an infrared source and was measured directly on the sample holder by a thermocouple. After each in situ treatment, samples were transferred from the reaction cell to the analysis chamber under high vacuum (less than $5x10^{-7}$ Pa).

The characterization of sample 1/2/1 was deeper in detail since its catalytic activity and selectivity towards hydrogen was the best of the three studied samples.

2.3 Results and discussion

2.3.1 As-synthesized samples

The peaks in the X-ray diffractogram of the as-synthesized samples could be indexed both to the Mg/Al and Co/Al hydrotalcite phases (XRD patterns 00-020-0658 [44] and

00-051-0045 [45], respectively; (see Figure 2.2). Since there is only one set of peaks we understand the samples are composed of Co/Mg/Al hydrotalcites. It has been reported that the crystallinity of MgAl hydrotalcites dramatically degrades due to the substitution of magnesium by cobalt ions [46]. In particular, the c parameter, related to the thickness of the interlayer distance in hydrotalcites (c = 3 x d (003)), decreases as the Co/Mg ratio is increased, because of a decay in electrostatic attraction between the brucite layer positive charges and interlayer negative charges [47]. In this sense, the first three peaks of the hydrotalcite diffractograms, indexed to 006, 0012 and 0018 reflections, are shifted to higher angles as the amount of cobalt increases. Sample 1/2/1_as is not only the most crystalline (narrowest peaks), but also bears these peaks at lower angles than the other two, indicating that cobalt ions might have not completely substituted magnesium cations within the brucite-like layers.

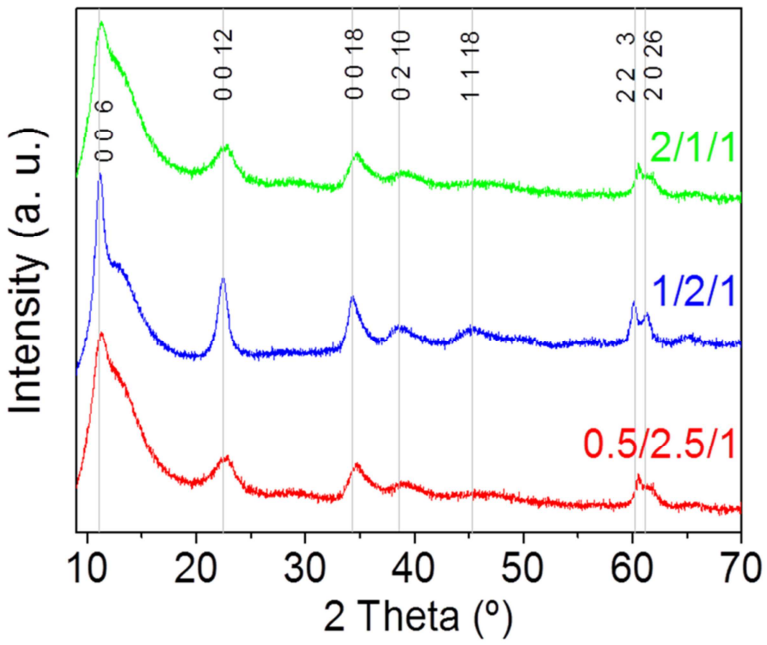

Fig. 2.2 X-Ray diffractograms of as-synthesized hydrotalcites. The hump centered around 13° is due to the sample holder.

IR spectra (not shown) also contain the bands corresponding to the hydrotalcite bonds: a broad band centered at 3458 cm^{-1} and a small one at 1618 cm^{-1} due to hydroxyl ions

and physically adsorbed water molecules, respectively; narrow bands around 1387 cm^{-1} corresponding to carbonate ions; and bands at low wavenumber 435, 625 and 637 cm^{-1} associated to Al-O, Co-O and Mg-O vibrations, respectively [48].

The morphology and structure of sample 1/2/1_as was studied by scanning and transmission electron microscopies (Figure 2.3). SEM showed a homogeneous and laminar material, as expected for hydrotalcites. The energy dispersive X-ray detector identified the presence of carbon, oxygen, cobalt, magnesium and aluminum with a molar ratio of Co:Mg:Al = 26:50:24, very close to the nominal value of 25:50:25. A closer view was facilitated by TEM. The sample bears sheet-like particles (average length = 62 ± 13 nm), stacked in bunches.

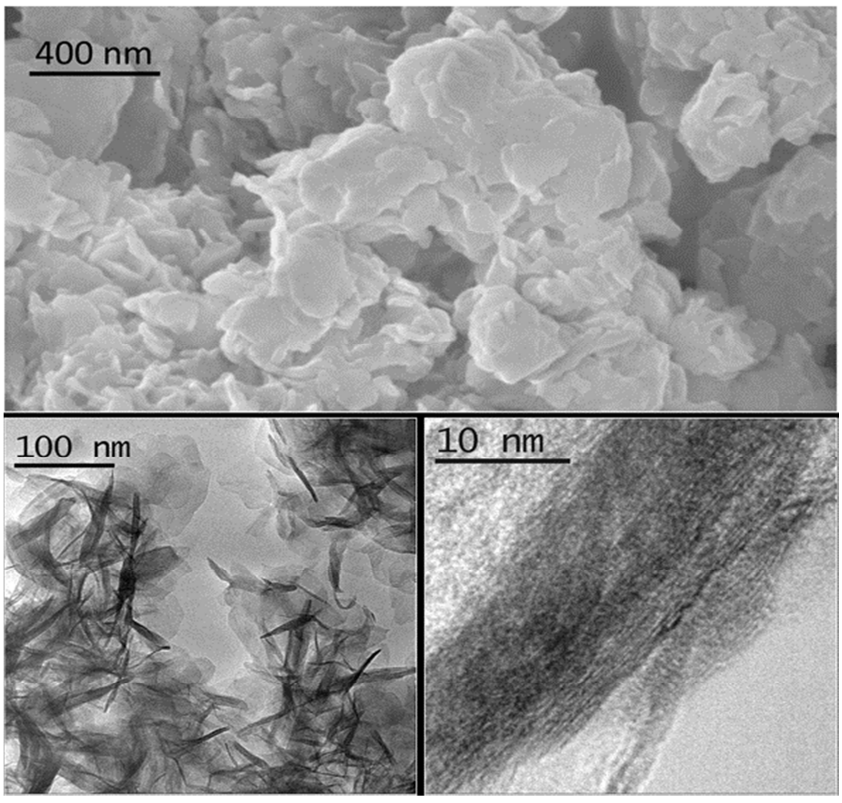

Fig 2.3 SEM image (above) and TEM images (below) of sample 1/2/1_as.

The as-synthesized samples showed paramagnetic (PM) behavior at room temperature and slightly superparamagnetic (SPM) at 5 K (Figure 2.4). The profile of the zero field cooled - field cooled (ZFC-FC) curves is characteristic of paramagnetic materials, with no maximum in the ZFC curve. The inverse of molar susceptibility of cobalt (χ_M; emu·mol^{-1}·Oe^{-1}) vs. temperature obeys the Curie-Weiss (2.7) law over 50 K (see Figure 2.4, right below).

$$\chi_M = \frac{C_M}{T-\theta} \qquad \text{(cgs units)} \qquad (2.8)$$

where C_M is the Curie constant (emu·K·mol^{-1}·Oe^{-1}), T is the temperature (K) and θ is the Weiss constant (K). Then, the inverse of the molar susceptibility is linear to the temperature:

$$\frac{1}{\chi_M} = \frac{1}{C_M} \cdot T - \frac{\theta}{C_M} \qquad (2.9)$$

The Curie constant is, in turn, related to the effective magnetic moment (μ_{eff}):

$$\mu_{eff} = \sqrt{\frac{C_M \cdot 3 \cdot k_B}{n \cdot N_A}} \qquad (\mu_B \text{ units}) \qquad (2.10)$$

where k_B is the Boltzmann constant (1.38·10^{-16} erg·K^{-1}), *n* is the number of magnetic atoms per molecular formula, N_A is the Avogadro's number (6.022·10^{23} mol^{-1}) and μ_B is the Bohr magneton (9.274·10^{-21} erg·Oe^{-1}). The calculated Curie constants for the 0.5/2.5/1_as, 1/2/1_as and 2/1/1_as samples were 8.30, 3.51 and 2.34 (emu·K·mol^{-1}·Oe^{-1}), respectively. The corresponding Weiss constants (θ) were -7.5, -15.1 and -13.4 K. These negative values indicate that antiferromagnetic (AFM) interactions are present in the samples. Furthermore, these AFM exchange interactions are enhanced (higher |θ|) as the Co/Mg ratio increases. Consequently, the magnetic moment per cobalt atom decays: 8.14, 5.30 and 4.33 μ_B for 0.5/2.5/1_as, 1/2/1_as and 2/1/1_as, respectively. The values of 1/2/1_as and 2/1/1_as are typical of cobalt atoms located in octahedral environments, as they are within the brucite-like layer of the hydrotalcite structure. The magnetic spins of the cobalt ions are usually aligned parallel within each layer. The observed AFM character is probably originated because of the layered structure with magnetic spins of opposite orientation in consecutive layers. As the amount of cobalt

increases, the probability of finding cobalt cations in consecutive layers is higher, for what the antiferromagnetic character intensifies. This description matches the one of some reported antiferromagnetic cobalt-aluminum hydrotalcites [49, 50], where a Curie constant of 2.91 emu·K·mol Co^{-1}·Oe^{-1}, a Weiss constant of -3.8 K and a magnetic moment of 4.82 μ_B for a Co:Al=3:1 molar ratio hydrotalcite were encountered.

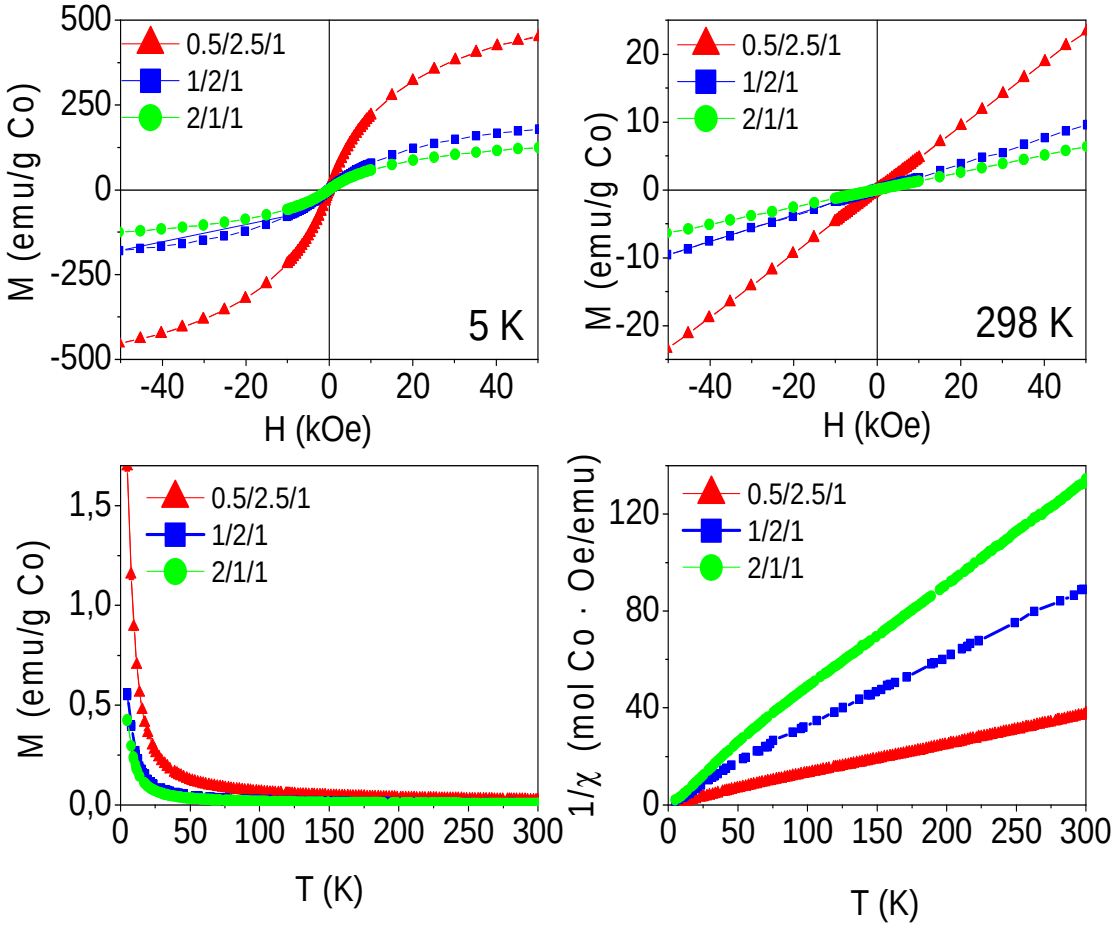

Fig. 2.4 Magnetization curves vs. applied magnetic field at 5 K and 298 K (above), magnetization vs. temperature at 50 Oe (below left) and inverse of susceptibility vs. temperature at 50 Oe (below right) of the as-synthesized samples.

2.3.2 Calcined samples

Ethanol steam reforming reaction was carried out over catalytic honeycombs calcined at 823 K since it is well known that thermal decomposition of Mg-Al hydrotalcites leads to a well dispersed mixture of magnesium and aluminum oxides with basic properties, which are favorable for the dehydrogenation of ethanol into acetaldehyde, the first step of ESR over Co-based systems (eq. 2.5). For that reason, hydrotalcites were thoroughly characterized after calcination at this temperature.

The calcination process was followed by thermogravimetric analysis (TGA) and differential scanning calorimetry (DSC). TGA profiles were derived to get the differential thermogravimetric (DTG) profiles for a better detection of the mass losses. Panels a, b and c in Figure 2.5 show these profiles of the three as-synthesized hydrotalcites. Furthermore, some of the analyses were coupled to a mass spectrometer, in order to identify the nature of the decomposed species. As can be observed in Figure 4, the three as-synthesized samples showed similar DTG profiles in argon: the first peak centered at 398 K was assigned to the desorption of physisorbed water, the one at 437 K corresponded to the decomposition of interlayer water and a small amount of carbonate ions in the form of carbon dioxide, and the overlapped peaks centered around 560 K and 627 K indicated the loss of interlayer anions (carbonates in the form of carbon dioxide, nitrate in the form of nitrous oxide and hydroxyl ions in the form of water). Further dehydroxylation of the brucite-like layers was accomplished mainly up to 900 K (as observed by mass spectrometry) but kept on slowly up to 1173 K. This profile for hydrotalcite thermal decomposition matches published results by other groups [51, 52]. The endothermic peak observed in the DSC profile above 900 K goes together with a drastic drop in the water evolved, as observed by mass spectrometry. Chmielarz et al. observed the evolution of molecular oxygen at this temperature range, for what they proposed that part of Co^{2+} cations were firstly oxidized to Co^{3+} by NOx species, and then the reverse process occurred with oxygen evolving [52]. As we do not observe oxygen evolving, neither other species, we understood the endothermic process as a crystalline restructuration of the material from hydrotalcite to spinel (see XRD data below), after dehydroxylation of the brucite-like structure. The percentages of mass losses in each stage are summarized in Table 2.1.

Co/Mg/Al molar ratio		0.5/2.5/1	1/2/1	2/1/1
T range 303–480 K	T DTG (K)	400	398, 498	400, 437
	Wt.%	11	11	11
	MS		H_2O	
T range 440–700 K	T DTG (K)	560, 627	570, 639	558, 626
	Wt.%	21	24	21
	MS		CO_2, NO, H_2O	
T range 700–1173 K	T DTG (K)	-	-	-
	Wt.%	7	6	6
	MS		H_2O	
Mass% left at ending T (1173K)		61	59	62
Theoretical wt.% $(Co,Mg,Al)O_x$/HT Co		59	61	65

Table 2.1 Data derived from thermogravimetric analysis of cobalt hydrotalcites. T DTG = temperature of minima in DTG profile. MS = species identified by mass spectrometry. HT Co = cobalt hydrotalcite

The amounts of mass losses are close to those expected from hydrotalcites with nominal formula: $[Co_xMg_{6-x}Al_2(OH)_{16}]CO_3{\cdot}4H_2O$, with x = 0.5, 1 and 2 and the mass left at 1173 K is close to the theoretical remaining mass of metal oxides $(Co_xMg_{6-x}Al_2)O_9$. The samples decomposed at the same temperature under air (see Figure 5). The most relevant difference between air and argon experiments is the lack of a peak in the DSC profiles around 1000 K under air atmosphere. Considering these peaks under argon as the crystalline change from hydrotalcite to spinel, we understand that the heating of the sample under air provides oxygen in order to follow this process progressively, from lower temperatures on. The IR spectra of the calcined samples showed (Co,Mg,Al)-O vibrations at low wave numbers and hydroxyl groups at 3470 cm^{-1}, whereas the band at 1380 cm^{-1} almost disappeared, suggesting the elimination of the carbonate groups.

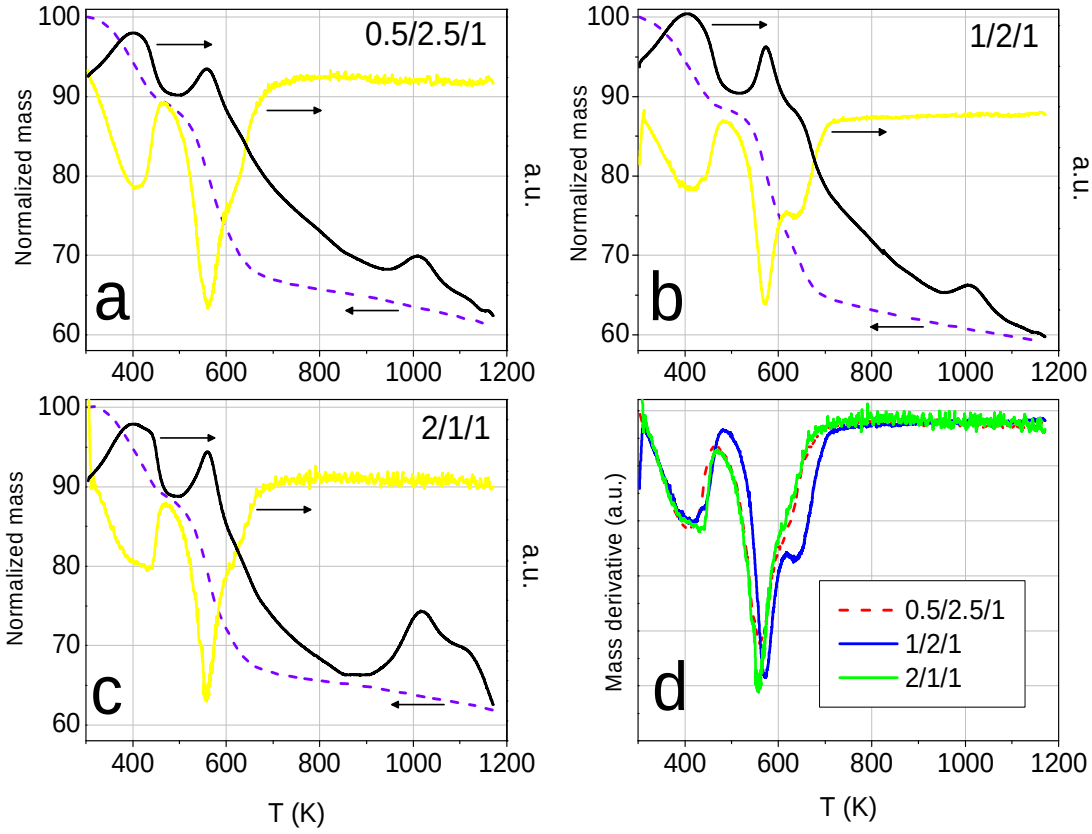

Fig. 2.5 Panels a, b and c: TGA profiles (dashed line), DT profiles (yellow line) and DSC profiles (black line) of cobalt hydrotalcites, heated under argon at 10 K min^{-1}. Panel d: DTG profiles under argon.

Panels d in Figure 2.5 and Figure 2.6 show the three DTG profiles together, under argon and under air, respectively. They highlight the better thermal stability of sample 1/2/1_as, fact that could have been expected from the higher crystallinity observed by XRD. Jiang et al [46] and Gennequin et al [47] observed that the addition of cobalt to Mg-Al hydrotalcites destabilizes them thermally, because $Co(OH)_2$ is less stable in air than $Mg(OH)_2$ and $Al(OH)_3$ and Co^{2+} has less affinity to CO_3^{2-} than Mg^{2+}. In this sense, the better thermal stability of sample 1/2/1_as could be understood as if not all the cobalt ions would have entered the crystal structure of hydrotalcite, in accordance with XRD data.

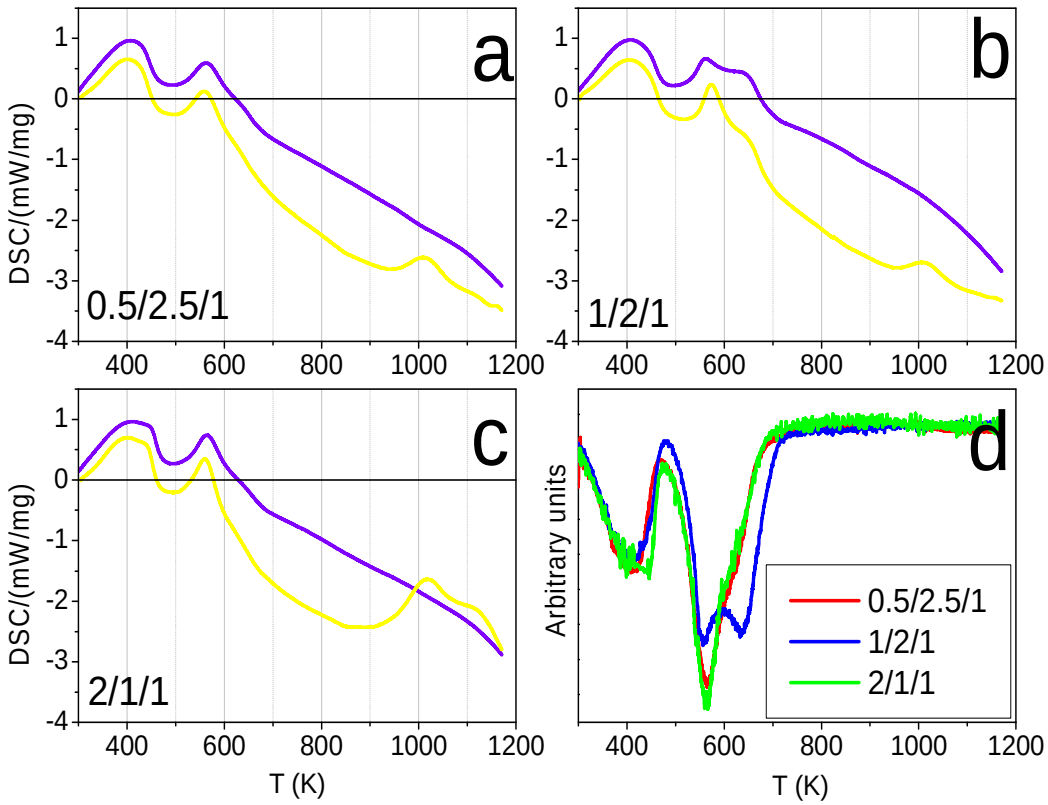

Fig. 2.6 Panels a, b and c: DSC profiles under air (violet line) and under argon (yellow line) of cobalt hydrotalcites, heated under argon at 10 K min^{-1}. Panel d: DTG profiles under air.

The X-ray diffractograms of the three samples after calcination showed a set of common peaks, indexed to $MgAl_2O_4$ and/or Co_2AlO_4 spinels (XRD patterns 01-075-1798 [53] and 00-038-0814 [54], respectively; see Figure 2.7. Diffractogram of sample 1/2/1_calc illustrates two shoulders at $2\theta \approx 43°$ and 63° (highlighted with arrows in Figure 6) which coincide with the main peaks of the rock salt type phase common to MgO and CoO (XRD patterns 01-07-1525 [55] and 01-075-0533 [56], respectively). There is also a different relative intensity of the (400) peak at $2\theta \approx 45°$: I(1/2/1_calc) = 60% and I(0.5/2.5/1_calc) ≈ I(2/1/1_calc) ≈ 42%. Considering the relative intensity of the peaks in $MgAl_2O_4$ and Co_2AlO_4 patterns [53, 54], the former difference in intensity at 45° might indicate a higher amount of magnesium spinel in 1/2/1_calc than cobalt spinel. These results are in accordance with the TGA profile of this sample (higher decomposition temperature) and the XRD data of the as-synthesized samples, suggesting that cobalt ions in sample 1/2/1 are not fully integrated into its crystalline structure.

Figure 2.8 depicts SEM images of sample 1/2/1_calc, which show a very homogeneous rounded morphology (above, left). By using a backscattered electron detector some particles with higher contrast were observed (white spots in the image above, right), which were assigned to cobalt-rich particles (since magnesium and aluminum have similar electron density, much lower than that of cobalt). Backscattered electron images and the shoulders observed in the X-ray diffractogram suggest that these particles are formed of CoO. A homogeneous area of the calcined sample was analyzed by EDX. The atomic ratio Co:Mg:Al was 27:50:24, close to the nominal value, 25:50:25. This analysis was contrasted with another performed onto a spot of higher contrast and, as expected, a higher amount of cobalt was detected, Co:Mg:Al = 56:31:13. HRTEM confirmed the change of morphology due to calcination in sample 1/2/1_calc (see Figure 7, below). The sheets of the as-synthesized sample were smashed up into small nanoparticles with average size 6.6 ± 2.2 nm (see below, left image). Some elongated particles were still seen, which reminded the hydrotalcite structure. Several lattice fringe images of bulk and edge particles were taken (see the two images in Figure 7, below middle and right). The lattice fringes of the bulk material were indexed to MgAl and/or CoAl spinels [53, 54], and the edge particles were indexed mainly to (Co,Mg)O, and also to spinel, in accordance with X-ray diffraction. A large number of the spinel rectangular particles showed preferential orientation along the [400] axis (d = 0.21 nm).

Calcination at 823 K not only induced strong morphologic and crystalline changes, but also magnetic ones. The magnetization at room temperature increased linearly with the magnetic field, as a paramagnet (see Figure 2.9, above right). At 5 K, the three calcined samples behaved slightly SPM (Figure 2.9, above left). At both temperatures, the net magnetization per gram of cobalt decreased as the molar ratio of Co in the formula increased, suggesting an increase in the antiferromagnetic exchange interactions between cobalt atoms, as they get closer to each other.

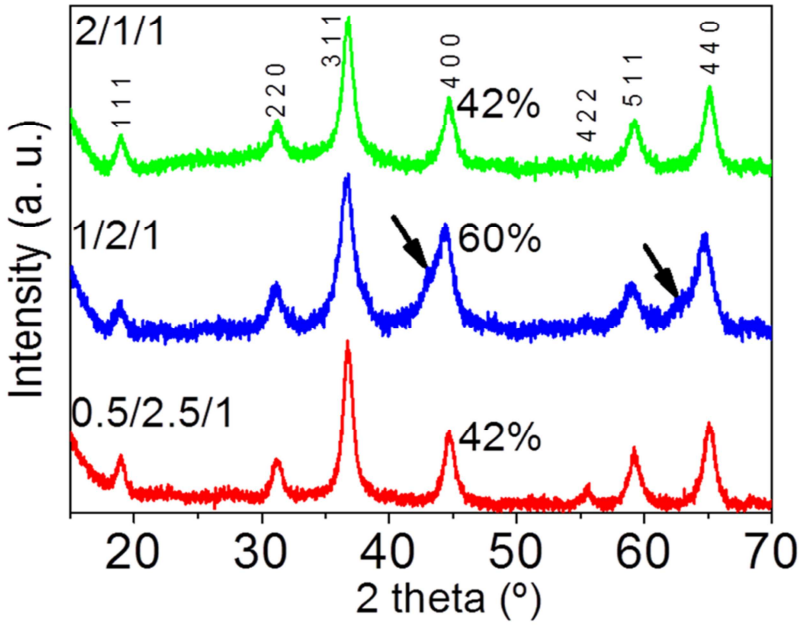

Fig. 2.7 X-Ray diffractograms of calcined samples.

The ZFC-FC curves showed hysteresis below 350, 230 and 300 K for 0.5/2.5/1_calc, 1/2/1_calc and 2/1/1_calc, respectively, although they also showed a remarkable paramagnetic behavior, evidenced by the high increase in magnetization at the lowest temperatures (Figure 2.9, below). Samples 1/2/1_calc and 2/1/1_calc presented a maximum in the ZFC curve at 200 and 220 K, respectively, defined as blocking temperature. This feature denotes a change in magnetic behavior with temperature. The blocking temperature of an AFM material is named Néel temperature. The CoAl spinels are AFM materials, with Néel temperatures below 33 K (the Néel temperature of the cobalt spinel, Co_3O_4) [57, 58]. CoO has a Néel temperature of 289 K.

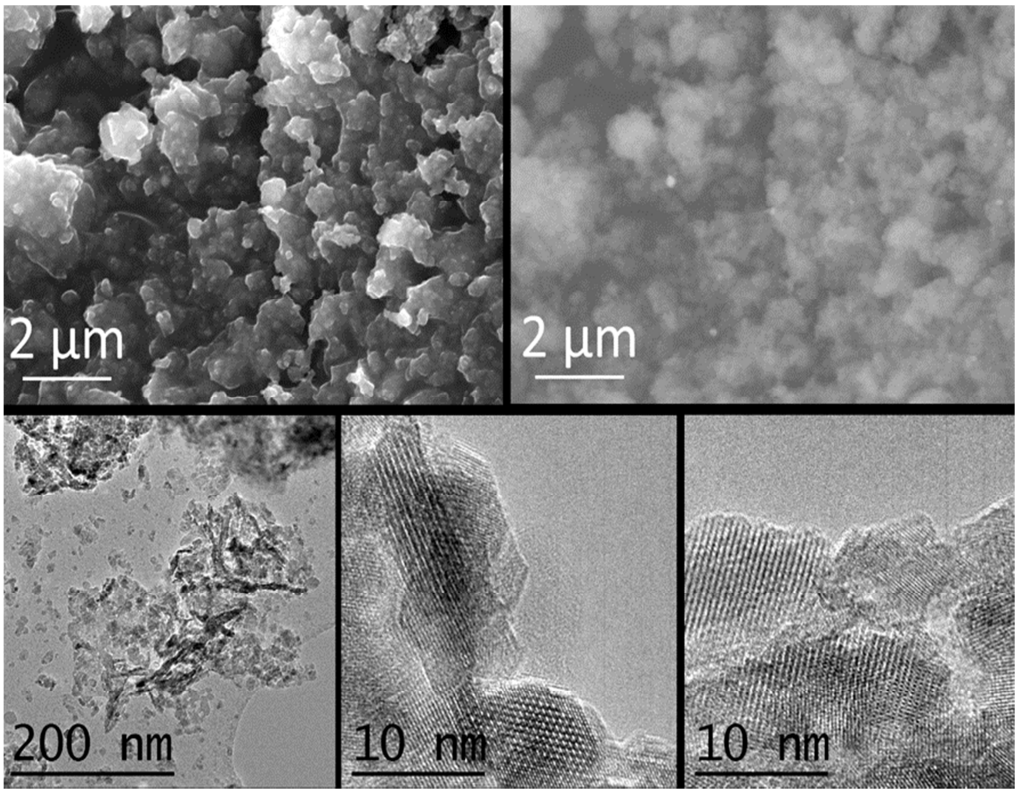

Fig. 2.8 SEM images (SE and backscattered electrons (BSE), above) and TEM images (below) of sample 1/2/1_calc.

The (Co,Mg)O solid solution bares decreasing values of Néel temperature as the amount of Mg is increased [59, 60]. In this context, the magnetic phase responsible for the high increase in magnetization at low temperature might be the CoAl spinel (which might have a Néel temperature lower than 5 K, unable to be measured with our equipment) and the magnetic phase responsible for the Néel temperature at 200 and 220 K, for 1/2/1_calc and 2/1/1_calc, might be a (Co,Mg)O solid solution with compositions $Co_{0.7}Mg_{0.3}O$ and $Co_{0.75}Mg_{0.25}O$, respectively (considering the data published in references [59, 60]). Magnetization measurements are much more sensitive than X-ray diffraction, for what it would be understandable that no peaks of this phase were identified by XRD in samples 0.5/2.5/1 and 2/1/1. No metallic cobalt was identified in the calcined samples with any technique.

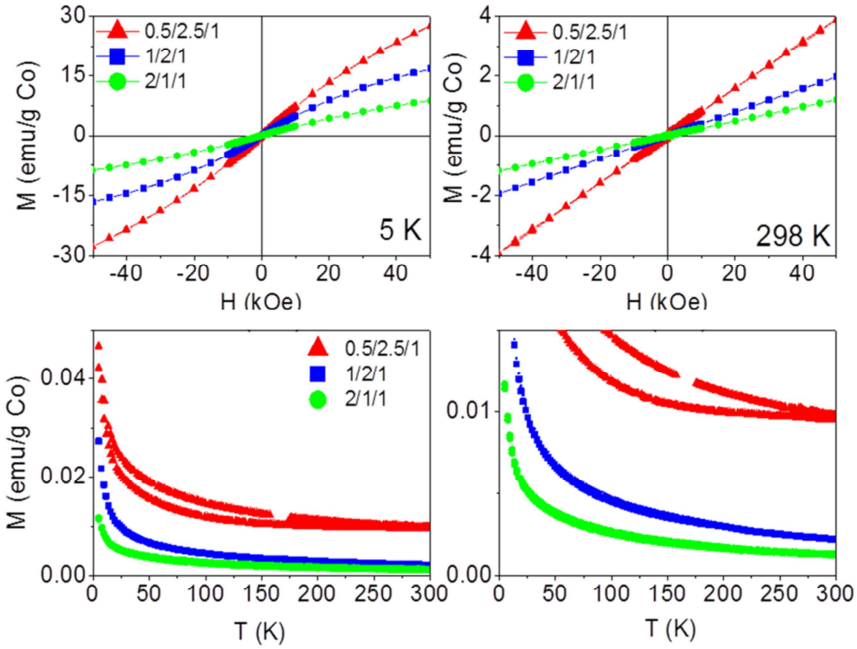

Fig. 2.9 Magnetization curves vs. applied magnetic field at 5 K (above, left) and 298 K (above, right) and vs. temperature at 50 Oe (below: on the left the whole curve and on the right a zoom at low magnetization) of the three calcined samples.

2.3.3 Ethanol steam reforming

The three catalysts performed well for the steam reforming of ethanol under the conditions tested in this work. Table 2.2 compiles the ethanol conversion values for each catalytic monolith attained in the 523-823 K temperature range as well as selectivity values on a dry basis at S/C=2, W/F=10^4 g·min·mol_{EtOH}^{-1} and VHSV=420 h^{-1}. Total conversion of ethanol was achieved at ca. 823, 773 and 823 K for samples 0.5/2.5/1_calc, 1/2/1_calc and 2/1/1_calc, respectively. At these temperatures, hydrogen selectivity was 67.3%, 69.5% and 67.2%, respectively. Therefore, sample 1/2/1_calc showed the best catalytic performance at the lowest temperature. This better performance might be related to the cobalt cations not being fully integrated into the crystalline structure of the catalyst, as discussed above. Below 773 K, the dehydrogenation of ethanol into acetaldehyde (equation 2.5) was the main reaction.

Dimethylketone was also obtained as a by-product, possibly by condensation of acetaldehyde, as reported in other cobalt-based systems [15, 16]. The temperature of disappearance of acetone matched the temperature of highest hydrogen selectivity for each sample. As expected, the amount of CO increased with temperature at the expense of CO_2 according to the water gas shift equilibrium. Interestingly, low amounts of methane were formed, indicating that decomposition of ethanol and methanation reactions were not important.

Co/Mg/Al molar ratio	T (K)	Ethanol conv. (%)	Selectivity (%)							
			CH_3CH_2OH	H_2	CO_2	C_2H_4	CH_3CHO	CH_3COCH_3	CH_4	CO
0.5/2.5/1	553	2	42.5	37.5	12.5	---	17.2	---	6.2	6.2
	673	25	23.4	41.7	12.5	3.1	15.1	5.2	1.0	2.1
	773	94	2.3	52.6	14.5	3.8	0.2	21.8	3.4	2.4
	823	100	0.1	67.2	10.6	0.5	---	0.9	4.1	16.8
1/2 /1	553	13	20.9	31.0	18.1	---	26.2	0.0	---	4.8
	673	66	8.2	45.9	6.6	7.1	27.9	9.8	0.5	1.1
	773	100	---	69.5	10.8	0.1	---	1.4	1.6	16.6
	823	100	---	69.1	9.1	---	---	---	1.9	20.0
2/1/1	553	5	41.9	26.3	10.5	---	23.9	5.3	5.3	5.3
	673	44	24.0	43.0	10.5	4.5	10.2	6.3	1.5	2.5
	773	88	4.7	56.0	15.5	2.9	---	14.9	5.1	4.1
	823	100	---	67.3	9.2	---	---	---	2.9	20.5

Table 2.2 Ethanol conversion (conv.) and product selectivity at different temperature over catalytic honeycombs loaded with hydrotalcite-derived cobalt catalysts. W/F = 104 g min mol_{EtOH}^{-1}, VHSV = 420 h^{-1}. Co/Mg/Al is the metallic molar ratio.

Figure 2.10 shows the stability of the catalytic monoliths tested in terms of hydrogen yield (defined as ethanol conversion multiplied by hydrogen molar fraction on a dry basis) over time on stream at 823 K under a pure ethanol-water mixture (S/C=2,W/F=390 g·min·mol_{EtOH}^{-1}, VHSV=660 h^{-1}). Samples showed a slow deactivation over time, but to a different degree; the stability follows the trend 1/2/1_calc>2/1/1_calc~0.5/2.5/1_calc. Therefore, the catalytic honeycomb 1/2/1_calc exhibited the best catalytic behavior, both in terms of selectivity towards hydrogen and stability. This result merits to be highlighted because to the best of our knowledge this is the first cobalt-based catalyst which shows such stability for ESR under undiluted

ethanol-water mixtures. In most cobalt-based systems strong deactivation occurs readily under high ethanol loads due to extensive carbon deposition.

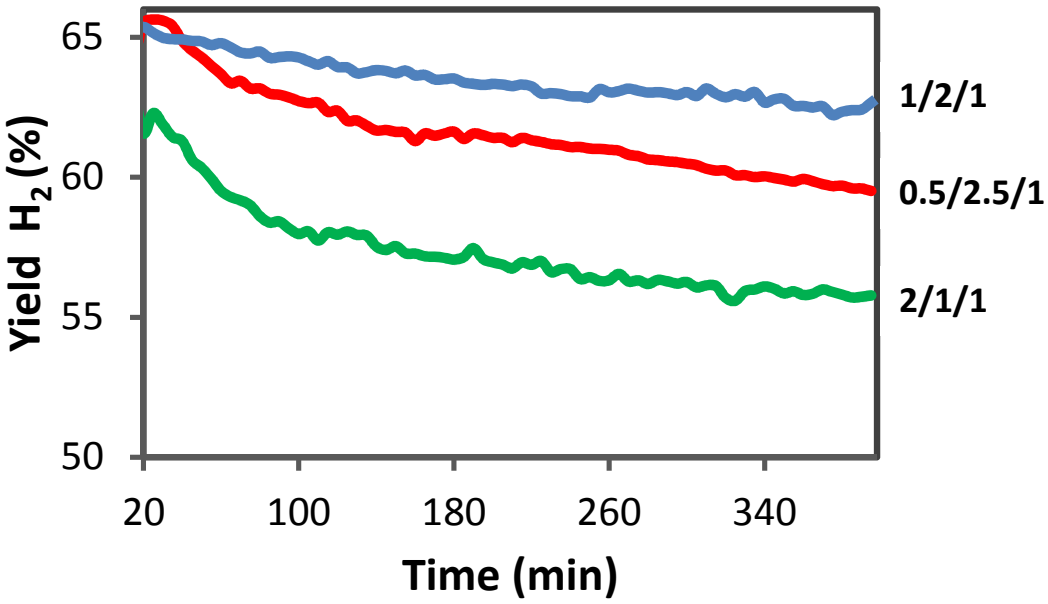

Fig. 2.10 Hydrogen yield obtained under ESR at 823 K. S/C = 2, W/F = 390 g min mol_{EtOH}^{-1}, VHSV = 660 h^{-1}.

2.3.4 Samples after ESR

The reacted samples showed simple XRD profiles (Figure 2.11) with three peaks, which correspond to the rock salt type phase, common to MgO and CoO (XRD patterns 01-07-1525 [55] and 01-075-0533 [56]). Once more, sample 1/2/1_reac was different from the other two in the relative intensity of the peak located at 37°, 29% vs. 45% for 0.5/2.5/1_reac and 2/1/1_reac counterparts. Considering that the theoretical relative intensity of this peak for MgO is 12% and for CoO is 68%, it can be concluded that sample 1/2/1_reac has a higher amount of MgO than the other two samples. The crystalline size, calculated using the Scherrer's formula, is nanometric in all samples (between 5 and 12 nm). On the other hand, bands at 565 and 680 cm^{-1} in the IR spectra are prominent, which are assigned to $Co^{\delta+}$-O [61].

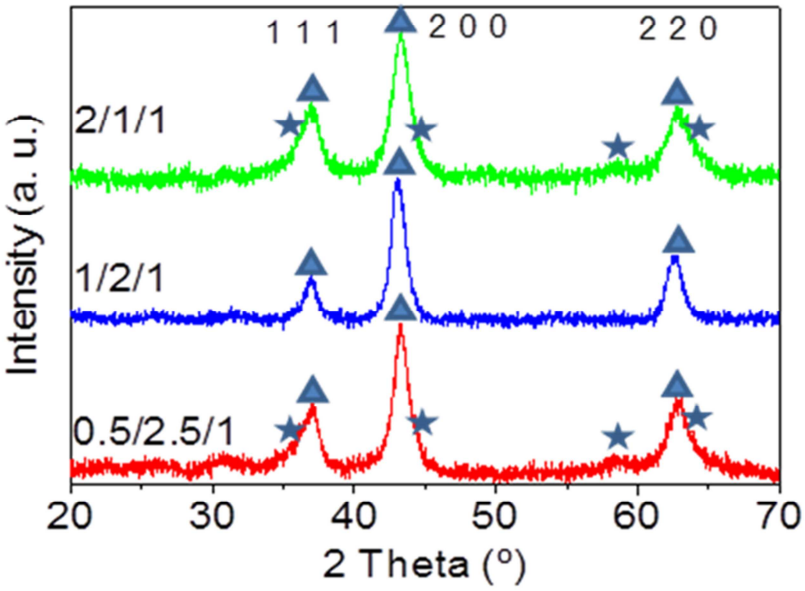

Fig. 2.11 X-Ray diffractograms of reacted samples. Triangles indicate CoMgO solid solution and stars spinel phase.

The morphology of sample 1/2/1_reac observed by SEM (Figure 2.12) was similar to sample 1/2/1_calc, that is, a cluster-of-grape morphology of small, rounded particles together with cobalt-rich particles. Furthermore, only a few sporadic carbon nanotubes could be observed. The Co:Mg:Al elemental ratio analyzed by EDS in homogeneous areas was also close to the nominal value (22/52/26). TEM images also showed that sample 1/2/1_reac was composed of rounded and kidney-like particles, with an average size of 7.4±1.9 nm (Figure 2.12). Some elongated structures were visible, which were understood as rehydrated hydrotalcites. Again, no significant carbon deposition was observed and only a few carbon nanotubes could be detected. From lattice-fringe images and Fourier Transform (FT) analysis, a clear difference in composition between the bulk matrix and the cobalt-rich particles was encountered. The former is composed only by (Co,Mg)O solid solution, whereas the cobalt-rich particles showed interplanar distances corresponding to spinel phases, similar to the ones identified in the calcined sample. Interestingly, no metallic cobalt particles were found, which have been extensively reported to occur in cobalt catalysts after ethanol steam reforming operation [12, 13, 15, 16, 33].

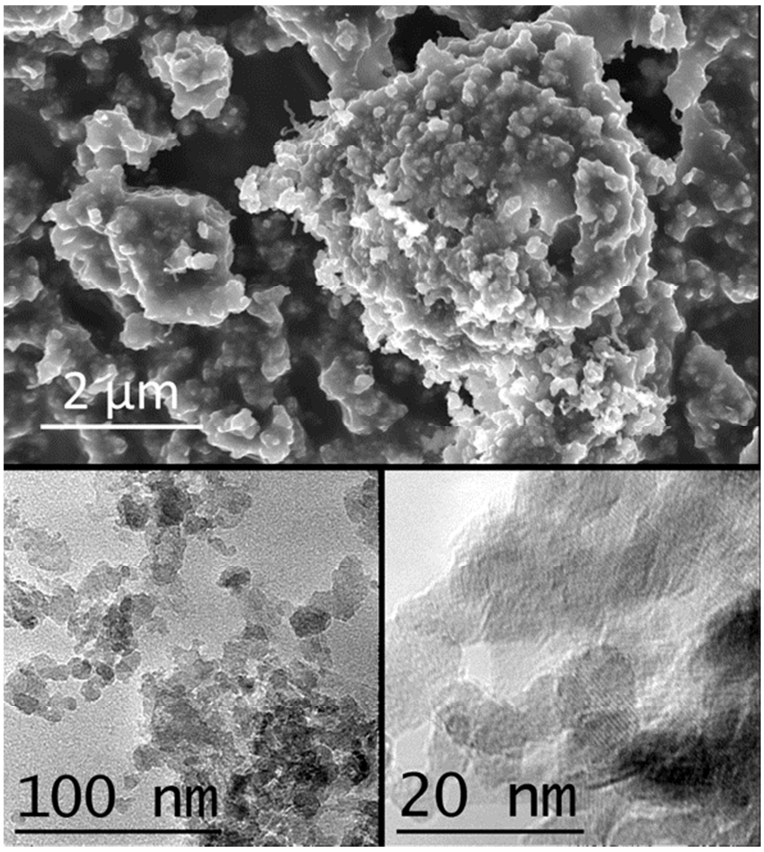

Fig. 2.12 Representative SEM (above) and TEM (below) images of sample 1/2/1_reac.

The reacted samples showed a new magnetic behavior. At room temperature the magnetization vs. field curves revealed two magnetic roles (Figure 2.13): a ferromagnetic one (FM), illustrated by the hysteresis cycle at low fields, and another paramagnetic (PM), illustrated by the linear increase at high fields. At 5 K the hysteresis is still visible for samples 0.5/2.5/1_reac and 1/2/1_reac, but no more for 2/1/1_reac. The ferromagnetic behavior must be attributed to the presence of metallic cobalt. Nevertheless, the percentage of metallic cobalt in the sample is very low, considering that its bulk saturation magnetization is 163 emu/g and the saturation magnetization of samples 0.5/2.5/1, 1/2/1 and 2/1/1 is only 9.65, 1.18 and 0.17 emu/g Co, respectively. Therefore, we estimate 5.9wt.%, 0.7wt.% and 0.1wt.%, of metallic cobalt in each sample. The ZFC-FC curves show a big hysteresis for sample 0.5/2.5/1_reac, smaller hysteresis for 1/2/1_reac and even smaller for 2/1/1_reac, in accordance with the previous data. The Néel temperatures in the three cases are over, but close to, 300 K. Based on the above, the reacted samples contain two magnetic phases: traces of metallic cobalt (FM)

and a main AFM phase, which is attributed to oxidized cobalt (CoO or (CoMg)O solid solution and a likely small contribution of CoAl spinel), according to XRD and HRTEM. Another datum to support that the oxidized cobalt is the main phase is the fact that the higher the amount of cobalt, the smaller the net magnetization of the reacted samples, in accordance with the behavior of an antiferromagnetic material. No nanoparticles of metallic cobalt were identified by HRTEM, although its high electronic density favors its detection due to a higher electron contrast compared to magnesium- and aluminum-containing oxides. Together with the small saturation magnetization values, we assume that there are very few nanoparticles and they have very small size.

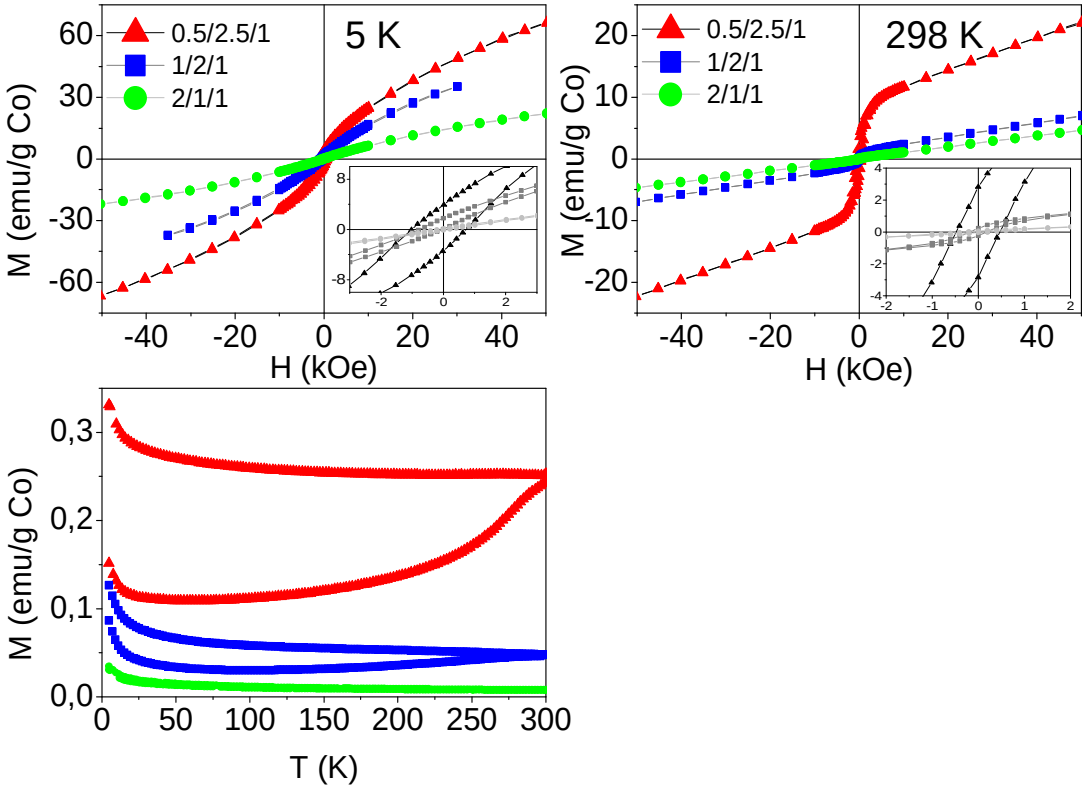

Fig. 2.13 Above: Magnetization curves of reacted samples vs. applied magnetic field at 5 K and 298 K (insets: magnification of low field areas). Below: Magnetization curves of reacted samples vs. temperature at 50 Oe.

The reacted samples were also analyzed by TPR (Figure 2.14) and showed only one peak, which corresponds to the reduction of oxidized cobalt to Co^0. Sample 0.5/2.5/1_reac has its maximum at 833 K. However, samples 2/1/1_reac and 1/2/1_reac show maxima at

higher temperatures, 904 and 990 K, respectively, and they just begin to reduce at 823 K. The effluents of the TPR experiments were followed by mass spectrometry. It was observed that some methane was evolved, between 673 and 1073 K, due to the reduction of superficial carbon. After calibration of the signal M/Z = 15 (CH_3^+), the amount of methane, and therefore of carbon, was quantified for the three samples. The mass of carbon for samples 0.5/2.5/1_reac, 1/2/1_reac and 2/1/1_reac was 4.4, 0.8 and 0.1 wt.% C, respectively. Considering that the samples were submitted to ethanol reforming conditions for 7 hours, they generated $6.3 \cdot 10^{-3}$, $1.2 \cdot 10^{-3}$ and $2.0 \cdot 10^{-3}$ $g_C \cdot g_{catalyst}^{-1} \cdot h^{-1}$. The amount of carbon is, in any case, scarce for cobalt catalysts working under high ethanol loadings. It might be deduced that, at the reforming temperature, 823 K, sample 0.5/2.5/1 is partially reduced to metallic cobalt (Figure 2.14), which can be the origin of its higher instability during reforming conditions (Figure 2.10), due to the formation of some carbon. Indeed, the order of stability during reforming conditions matches the order of reduction temperature in TPR experiments: 0.5/2.5/1_reac < 2/1/1_reac < 1/2/1_reac.

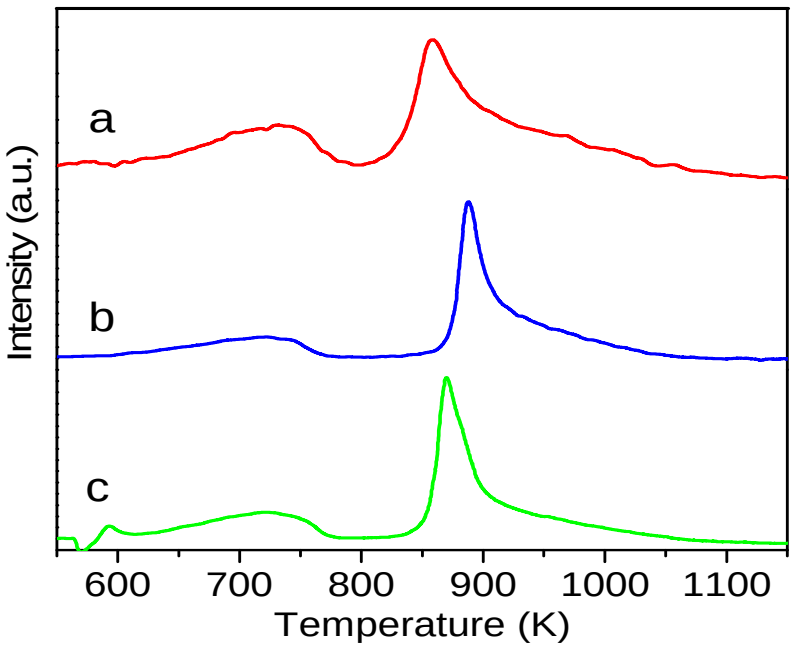

Fig. 2.14 TPR profiles of calcined samples, 0.5/2.5/1_reac (a), 1/2/1_reac (b) and 2/1/1_reac (c).

XPS analysis of the reacted samples showed differences in their surface composition. Surprisingly, the Co/Mg/Al molar ratios at the surface were 1.1/1.3/1, 0.9/2.0/1 and

0.9/1.2/1, for samples 0.5/2.5/1_reac, 1/2/1_reac and 2/1/1_reac, respectively. Sample 0.5/2.5/1 has 4 times more cobalt at the surface than the nominal value, sample 1/2/1 is quite homogeneous and sample 2/1/1 has around 37% of the nominal cobalt at the surface. Each Co2p spectra is formed of two main peaks (components $2p_{3/2}$ and $2p_{1/2}$) and two satellites. In sample 0.5/2.5/1_reac each peak can be fitted to two components: the first one, at 779.4 eV, can be assigned to metallic cobalt and the second one, at 781.1 eV, corresponds to oxidized cobalt and is accompanied by a satellite. Samples 1/2/1_reac and 2/1/1_reac show only one component of oxidized cobalt. There is a relationship between the cobalt/magnesium molar ratio at the surface and the amount of metallic cobalt, as shown by magnetometry and also XPS.

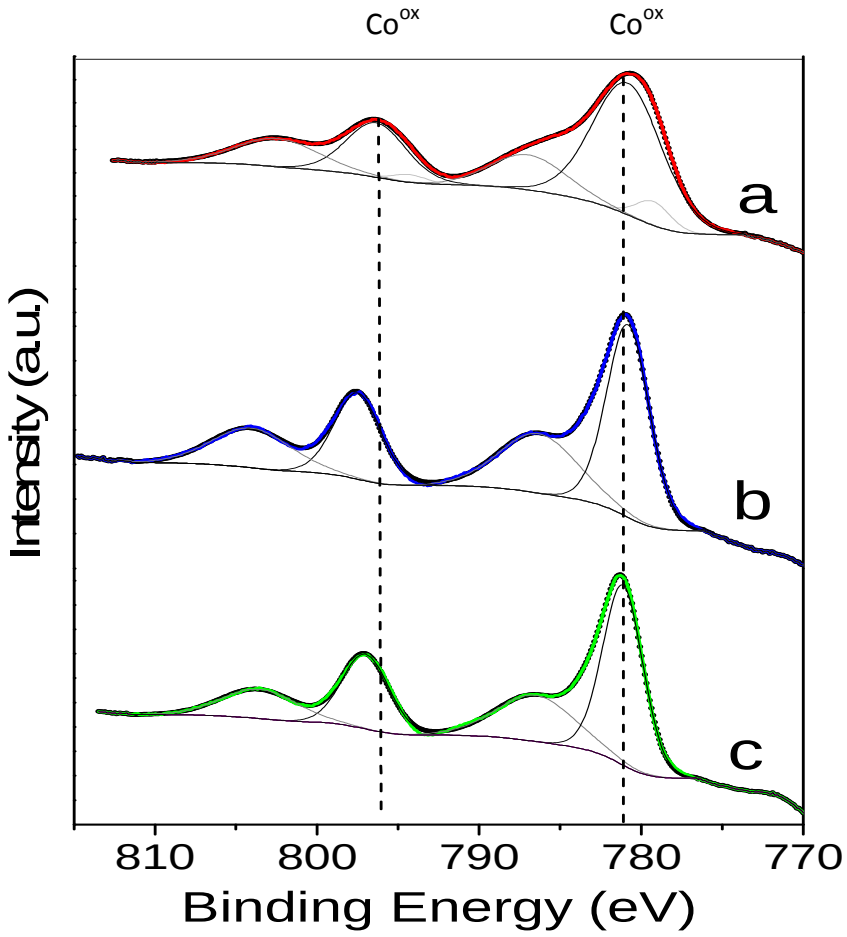

Fig. 2.15 Co 2p XPS spectra of sample 0.5/2.5/1_reac (a), 1/2/1_reac (b) and 2/1/1_reac (c).

In addition, we decided to carry out an in situ XPS study over the sample 1/2/1 in order to get insight into the occurrence of surface reduced cobalt under reaction conditions, which has been largely considered the active species for ESR over cobalt systems [13, 33, 35, 36]. Sample 1/2/1 was analyzed in situ in its as-synthesized form, after calcination at 823K, after ESR reaction at 823 K (the evolution of reaction products was followed simultaneously by mass spectrometry) and also after being reduced at 823 K under a hydrogen flow. All the analyses were performed consecutively, under high vacuum. The spectra corresponding to the Co 2p core level are shown in Figure 15. The spectrum of the as-prepared sample (Figure 2.13a) showed two peaks centered at binding energies of 781.0 (Co $2p_{3/2}$) and 797.2 eV (Co $2p_{1/2}$), along with two satellites. The position of these peaks and their separation are ascribed to Co^{2+} species. The high intensities of the satellites are in accordance with the structure of the cobalt hydrotalcite, where the metal occupies octahedral sites in a 2+ oxidation state. After calcination (Figure 14b) the intensity of the satellite lines decreased relative to the spin-orbital splitting components. In addition, two sets of signals appeared at 781.0 / 796.0 eV and 781.4 / 797.5 eV, which correspond to Co^{2+} species in different environments. The satellite lines were located at about 8-9 eV above the photo lines, thus indicating a partial charge transfer from Co^{2+}, probably due to a strong interaction with Mg and Al [62]. The presence of these two Co^{2+} species could be related to the formation of cobalt aluminate spinel and (Co,Mg)O solid solution [63, 64], in accordance with XRD and magnetic measurements. Co^{2+} in (Co,Mg)O solid solution exhibits an octahedral environment whereas Co^{2+} in cobalt spinel may occupy both octahedral and tetrahedral positions, depending on Al^{3+} substitution. After ESR (Figure 2.15c) the XP spectrum showed again strong satellite lines, which were located at about 6-6.5 eV above the photo lines. Contrary to that, very weak satellites, to be shifted about 10-11 eV to higher binding energies from the main peaks, are characteristic of Co^{3+} species, and metallic cobalt does not contain shake-up satellite structure at all [65]. Moreover, the full width at half maximum (FWHM) of Co^0 is characteristically narrow (< 1.5 eV) and FWHM values of the bands in Figure 2.15c are about 2.5-3 eV. Therefore, the only species identified at the surface of the catalyst under ethanol steam reforming conditions is Co^{2+}. Contrarily to other in situ XPS experiments conducted under similar conditions [13], no reduced cobalt species has been identified. In the spectrum, two Co^{2+} species are identified at 780.7 / 796.7 eV and 782.7 /

796.6 eV, which may correspond to the cobalt-alumina spinel and CoO phases infused from magnetic measurements as well. Finally, the sample was exposed to hydrogen flow at the same temperature used for ESR (823 K). The resulting spectrum is virtually identical to that recorded after ESR, thus indicating that at this temperature Co^{2+} species are stable and do not evolve into metallic entities. Actually, the TPR profile confirms that sample 1/2/1_reac reduces significantly only over 860 K (Figure 2.14), and at reforming temperature, 823 K, it is oxidized. This in situ experiment allows us to conclude that Co^{2+} species are active for the ethanol steam reforming reaction. Moreover, the absence of metallic cobalt at the surface of the catalyst would preclude carbon deposition. The C/Co atomic ratio at the surface for samples 1/2/1_calc and 1/2/1_reac was calculated from the XP spectra were 0.04 and 0.15, respectively. Together, this represents a new generation of cobalt catalysts for producing hydrogen from ethanol at moderate temperature.

2.3.5 Spinel

Since the characterization of the catalysts after reaction showed the existence of cobalt-aluminum spinel along with MgO-CoO, an additional experiment was performed over a mixture of CoAl spinel and MgO in order to check if CoAl spinel and MgO are responsible for the catalytic performance in ESR by themselves or if the hydrotalcite precursor plays a key role in the catalytic properties of the final material. This experiment will serve to check if CoAl spinel prepared by conventional methods exhibits the same behavior as spinel derived from hydrotalcite precursor.

CoAl spinel was prepared by the combustion synthesis method from $Mg(NO_3)_2{\cdot}H_2O$ (Sigma Aldrich) and $Al(NO_3)_3 \cdot 9H_2O$ (Sigma Aldrich) and urea (Sigma Aldrich) as a fuel [66]. The reaction was carried out in a batch reactor. The mixture was grinded vigorously to get a homogenous mixture, and then heated at 773 K for three hours.

The resulting product was characterized by powder X-ray diffraction (XRD) (Fig 2.16). All peaks are indexed to Co_2AlO_4 and/or MgO (XRD patterns JCPDS 00-038-0814 and JCPDS 00-045-0946, respectively).

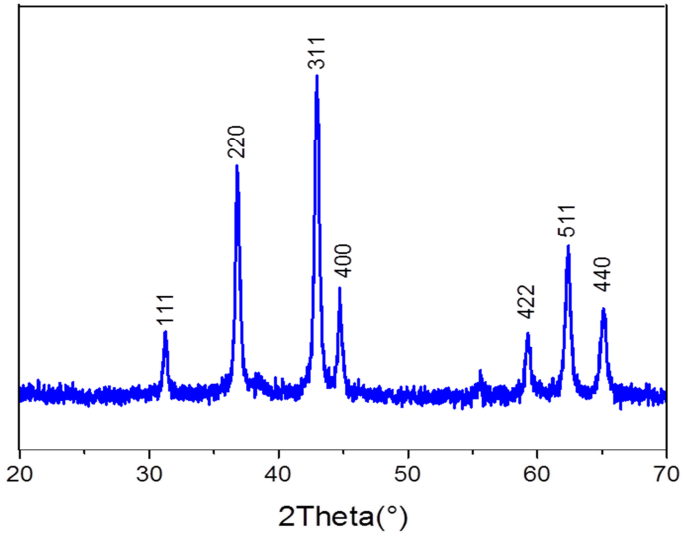

Fig. 2.16 XRD profile of the synthesized CoAl spinel

ESR tests were carried out exactly under the same conditions as reported previously for the hydrotalcite samples. Figure 2.17a shows ethanol conversion results for spinel and hidrotalcite 1/2/1. Both samples exhibit the same behavior having similar mass transfer properties from 750 to 823 K. However, the hydrotalcite-derived catalyst is more active for ethanol transformation at lower temperature than the spinel synthesized ex-situ. This could be ascribed to a particle size effect since hydrotalcite-derived spinel particles are about 6.6 nm in size whereas spinel particles prepared ex-situ are about 8.0 nm (as deduced from XRD).

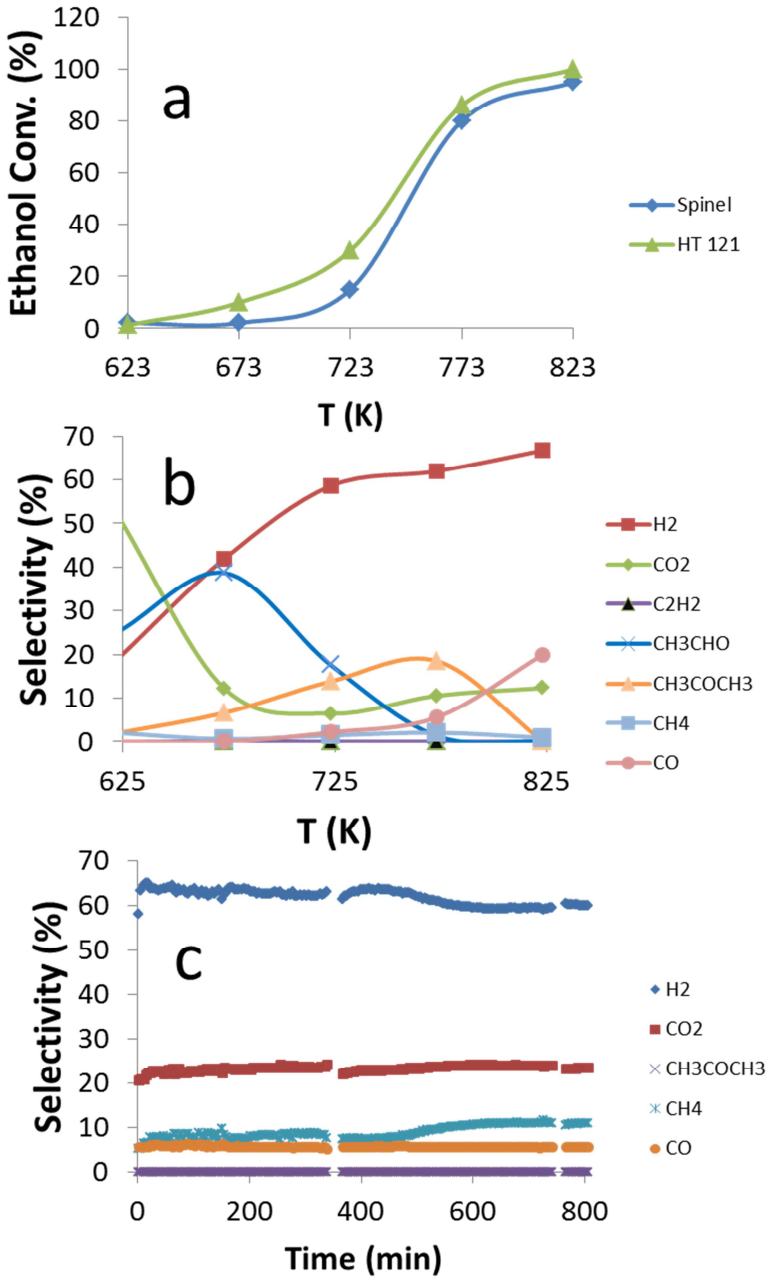

Fig. 2.17 ESR over CoAl spinel prepared ex-situ, S/C = 2, W/F = 390 g min mol_{EtOH}^{-1}, VHSV=660 h^{-1}. Ethanol conversion (a) and selectivity (b) vs. temperature and stability at 823 K (c).

The distribution of products for the spinel sample is shown in fig 2.17b. At 775 K, when both hydrotalcite-derived catalyst and spinel sample have similar ethanol conversion values, acetaldehyde and acetone selectivity is slightly higher in the spinel sample than that obtained over the hydrotalcite 1/2/1 (table 2.2). Therefore, at similar conversion the hydrotalcite-derived catalyst shows better selectivity for the steam reforming of

ethanol, which suggests that the CoAl spinel, although remarkably active for the reaction, performs better when it is obtained by decomposition of the hydrotalcite precursor. Finally, a ESR stability test over the CoAl spinel prepared ex-situ is also included in figure 2.17c. After approximately 8 h on stream at 823 K there is an increase of the methane production at the expense of hydrogen due to the decomposition of ethanol. Then, the CoAl spinel is also less stable than the corresponding hydrotalcite-derived catalyst, which almost showed no signs of deactivation (figure 2.18).

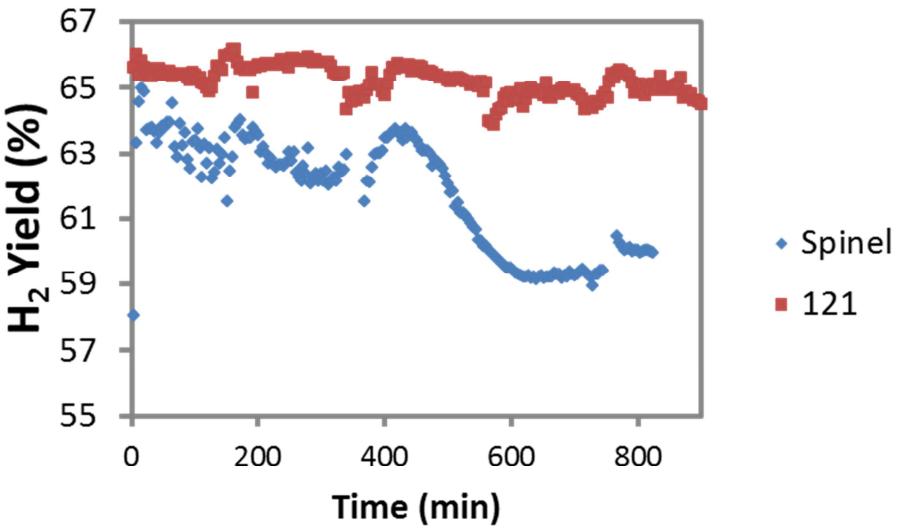

Fig. 2.18 Hydrogen yield over time on stream of hydrotalcite 1/2/1 vs CoAl spinel.

2.4 Conclusions

We have synthesized cobalt-based catalysts for ESR derived from Co/Mg/Al hydrotalcites that present high activity and selectivity towards hydrogen (69.5%) at moderate temperature (773 K). The best catalytic performance is obtained over the material obtained from Co/Mg/Al=1/2/1 hydrotalcite. A thorough characterization has evidenced that it contains CoAl spinel particles as well as CoO strongly interacting with MgO. However, CoAl spinel prepared separately is less active and stable for ESR than the hydrotalcite-derived material. Unlike previously reported cobalt catalysts for ESR, no metallic cobalt has been detected in our material, which scarcely generates carbon under practical ESR conditions. Then, Co^{2+} species should be active for ESR reaction. This is a meaningful result, since the catalytic activity in cobalt-based systems has been traditionally assigned to metallic cobalt.

2.5 References

[1] A. Haryanto, S. Fernando, N. Murali and S. Adhikari, Energ. F., 19, (2005), 2098-2106.

[2] P. D. Vaidya and A. E. Rodrigues, Ch. Eng. J., 117, (2006), 39-49.

[3] M. Ni, D. Y. C. Leung and M. K. H. Leung, Int. J. Hydrogen Energy, 32, (2007), 3238-3247.

[4] G. Kolb, Fuel processing for fuel cells, ed. Wiley-VCH, (2008), 1-434.

[5] J. Llorca, in Handbook of sustainable energy, ed. W. H. Lee and V. G. Cho, Nova Publishers, 22, (2010), 693-699.

[6] A. Casanovas, M. Saint-Gerons, F. Griffon and J. Llorca, Int. J. Hydrogen Energy, 33, (2008), 1827-1833.

[7] G. A. Deluga, J. R. Salge, L. D. Schmidt and X. E. Verykios, Sci., 303, (2004), 993-997.

[8] F. Frusteri and S. Freni, J. of Power Sources, 173, (2007), 200-209.

[9] H. Idriss, M. Scott, J. Llorca, S. C. Chan, W. Chiu, P. Y. Sheng, A. Yee, M. A. Blackford, S. J. Pas, A. J. Hill, F. M. Alamgir, R. Rettew, C. Petersburg, S. D. Senanayake and M. A. Barteau, Chem Sus Chem, 1, (2008), 905-910.

[10] J. Llorca, A. Casanovas, T. Trifonov, A. Rodriguez and R. Alcubilla, J. Catal., 255, (2008), 228-233.

[11] A. Casanovas, C. de Leitenburg, A. Trovarelli and J. Llorca, Cat. Today, 138, (2008), 187-192.

[12] M. Dominguez, E. Taboada, E. Molins and J. Llorca, Cat. Today, 138, (2008), 193-197.

[13] M. Dominguez, E. Taboada, H. Idriss, E. Molins and J. Llorca, J. of Mat. Chemistry, 20, (2010), 4875-4883.

[14] A. Casanovas, M. Dominguez, C. Ledesma, E. Lopez and J. Llorca, Cat. Today, 143, (2009), 32-37.

[15] J. Llorca, N. Homs, J. Sales and P. R. de la Piscina, J. Catal., 209, (2002), 306-317.

[16] J. Llorca, P. R. de la Piscina, J. A. Dalmon, J. Sales and N. Homs, App. Catal. B. Environ., 43, (2003), 355-369.

[17] J. Llorca, N. Homs, J. Sales, J. L. G. Fierro and P. R. de la Piscina, J. Catal., 222, (2004), 470-480.

[18] S. Tuti and F. Pepe, Catal. Lett., 122, (2008), 196-203.

[19] A. E. Galetti, M. F. Gomez, L. A. Arrua, A. J. Marchi and M. C. Abello, Catal. Commun., 9, (2008), 1201-1208.

[20] J. C. Vargas, S. Libs, A. C. Roger and A. Kiennemann, Catal. Today, 107, (2005), 417-425.

[21] P. Bichon, G. Haugom, H. J. Venvik, A. Holmen and E. A. Blekkan, T. Catalysis, 49, (2008), 38-45.

[22] S. S. Y. Lin, D. H. Kim and S. Y. Ha, Catal. Lett., 122, (2008), 295–301.

[23] S. Freni, S. Cavallaro, N. Mondello, L. Spadaro and F. Frusteri, Catal. Commun., 4, (2003), 259-268.

[24] J. Sun, X. P. Qiu, F. Wu and W. T. Zhu, Int. J. Hydrogen Energy, 30, (2005), 437-445.

[25] F. Marino, G. Baronetti, M. Jobbagy and M. Laborde, App. Catal. A. General, 238, (2003), 41-54.

[26] M. S. Batista, R. K. S. Santos, E. M. Assaf, J. M. Assaf and E. A. Ticianelli, J. of Power Sources, 134, (2004), 27-32.

[27] H. Song and U. S. Ozkan, J. Catal., 261, (2009), 66-74.

[28] H. Song, L. Z. Zhang, R. B. Watson, D. Braden and U. S. Ozkan, Catal. Today, 129, (2007), 346-354.

[29] H. Wang, J. L. Ye, Y. Liu, Y. D. Li and Y. N. Qin, Catal. Today, 129, (2007), 305-312.

[30] M. Benito, R. Padilla, L. Rodriguez, J. L. Sanz and L. Daza, J. of Power Sources, 169, (2007), 167–176.

[31] A. Kaddouri and C. Mazzocchia, Catal. Commun., 5, (2004), 339-345.

[32] A. Chica and S. Sayas, Catal. Today, 146, (2009), 37-43.

[33] J. Llorca, P. R. de la Piscina, J. A. Dalmon and N. Homs, Chem. Materials, 16, (2004), 3573-3578.

[34] V. M. Garcia, E. Lopez, M. Serra and J. Llorca, J. of Power Sources, 192, (2009), 208-215.

[35] J. Llorca, N. Homs and P. R. de la Piscina, J. Catal., 227, (2004), 556-560.

[36] J. Llorca, J. A. Dalmon, P. R. de la Piscina and N. Homs, Appl. Catal., A, 243, (2003), 261-269.

[37] G. Busca, U. Costantino, T. Montanari, G. Ramis, C. Resini and M. Sisani, Int. J. Hydrogen Energy, 35, (2010), 5356-5366.

[38] L. He, H. Berntsen, E. Ochoa-Fernandez, J. C. Walmsley, E. A. Blekkan and D. Chen, Top. Catal., 52, (2009), 206-217.

[39] A. F. Lucredio, J. A. Bellido and E. M. Assaf, Catal. Commun., 12, (2011), 1286-1290.

[40] A. Casanovas, C. de Leitenburg, A. Trovarelli and J. Llorca, Chem. Eng. J., 154, (2009), 267-273.

[41] A. Casanovas, M. Roig, C. de Leitenburg, A. Trovarelli and J. Llorca, Int. J. Hydrogen Energy, 35, (2010), 7690-7698.

[42] M. Ohyama, H. Kozuka and T. Yoko, Thin Solid Films, 306, (1997), 78-85.

[43] Y. Men, H. Gnaser, R. Zapf, V. Hessel, C. Ziegler and G. Kolb, Appl. Catal., A, 277, (2004), 83-90.

[44] G. J. Ross and H. Kodama, American Mineralogist., 52, (1967), 1036-1047.

[45] T. Baird, K. C. Campbell, P. J. Holliman, R. Hoyle, D. Stirling and B. P. Williams, J. Chem. Soc., Faraday Trans., 91, (1995), 3219-3230.

[46] Z. Jiang, J. J. Yu, J. Cheng, T. C. Mao, M. O. Jones, Z. P. Hao and P. P. Edwards, Fuel Process. Technol., 91, (2010), 97-102.

[47] C. Gennequin, S. Siffert, R. Cousin and A. Aboukais, Top. Catal., 2009, 52, 482–491.

[48] K. Yan, X. M. Xie, J. P. Li, X. L. Wang and Z. Z. Wang, J. Nat. Gas Chem., 16, (2007), 371-376.

[49] J. Perez-Ramirez, A. Ribera, F. Kapteijn, E. Coronado and C. J. Gomez-Garcia, J. Mater. Chem., 12, (2002), 2370-2375.

[50] A. A. Khassin, V. F. Anufrienko, V. N. Ikorskii, L. M. Plyasova, G. N. Kustova, T. V. Larina, I. Y. Molina and V. N. Parmon, Phys. Chem. Chem. Phys., 4, (2002), 4236-4243.

[51] D. Tichit, M. H. Lhouty, A. Guida, B. H. Chiche, F. Figueras, A. Auroux, D. Bartalini and E. Garrone, J. Catal., 151, (1995), 50-59.

[52] L. Chmielarz, P. Kustrowski, A. Rafalska-Lasocha, D. Majda and R. Dziembaj, Appl. Catal., B, 35, (2002), 195-210.

[53] T. Yamanaka and Y. Takeuchi, Z. Kristallogr., 165, (1983), 65-78.

[54] P. G. Casado and I. Rasines, J. Solid State Chem., 52, (1984), 187-193.

[55] E. Schiebold, Z. Kristallogr., Kristallgeom., Kristallphys., Kristallchem., 52, (1921), 1036-1047.

[56] W. D. Johnston, R. R. Heikes and D. Sestrich, J. Phys. Chem. Solids, 7, (1958), 1-13.

[57] O. H. Hansteen, H. Fjellvag and B. C. Hauback, Acta Chem. Scand., 52, (1998), 1285-1292.

[58] T. Suzuki, H. Nagai, M. Nohara and H. Takagi, Journal of Physics- Condensed Matter, 19, (2007), 145-165.

[59] N. Mironova-Ullmane, U. Ullmanis, A. Kuzmin, I. Sildos, M. Pärs, M. Cestelli Guidi, M. Piccinini and A. Marcelli, Phys. Solid State, 50, (2008), 1723-1726.

[60] A. Z. Menshikov, Y. A. Dorofeev, N. A. Mironova and M. V. Medvedev, Solid State Commun., 98, (1996), 839-842.

[61] T. Montanari, M. Sisani, M. Nocchetti, R. Vivani, M. C. H. Delgado, G. Ramis, G. Busca and U. Costantino, Catal. Today, 152, (2010), 104-109.

[62] R. Guil-Lopez, R. M. Navarro, M. A. Pena and J. L. G. Fierro, Int.J. Hydrogen Energy, 36, (2011), 1512-1523.

[63] S. Kannan and C. S. Swamy, Catal. Today, 53, (1999), 725-737.

[64] K. Omata, T. Takada, S. Kasahara and M. Yamada, Appl. Catal., A, 146, (1996), 255-267.

[65] A. A. Khassin, T. M. Yurieva, V. V. Kaichev, V. I. Bukhtiyarov, A. A. Budneva, E. A. Paukshtis and V. N. Parmon, J. Mol. Catal. A: Chem., 175, (2001), 189-204.

[66] A.D. Mazzoni, E.F. Aglietti, Magnesium aluminium spinels from combustions reactions, Brazilian Ceramic Congress, 8, (1999), 19-22.

CHAPTER 3

Ethanol steam reforming over hydrotalcite-derived Co catalysts doped with Pt and Rh

Published in:

"Ethanol steam reforming over hydrotalcite-derived Co catalysts doped with Pt and Rh"

Raúl Espinal, Elena Taboada, Elies Molins, Ricardo J. Chimentao, Francesc Medina and Jordi Llorca

Topics in Catalysis, 56, (2013), 1660-1671.

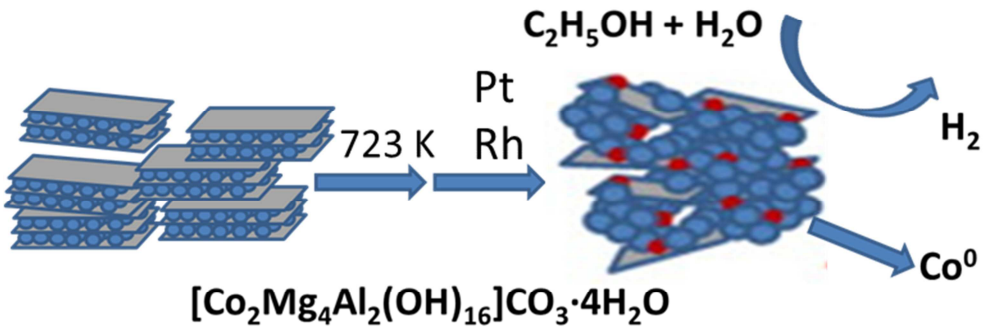

3.1 Introduction

Ethanol is nowadays a well-established source of hydrogen via catalytic steam reforming, oxidative reforming or partial oxidation processes. Numerous reviews have been published in the last years, covering both catalytic aspects and fuel reformer concepts [1-5]. Ethanol has the advantage over other conventional substrates such as natural gas, gasoline or liquefied petroleum gas (LPG) that it is readily available, easy to obtain from biomass, CO_2-neutral (bioethanol) and safe to handle [6]. Among the different processes for hydrogen production, ethanol steam reforming (ESR) is the simplest for implementation and the one that yields more hydrogen (eq. 3.1).

$$C_2H_5OH + 3\ H_2O \rightarrow 6\ H_2 + 2\ CO_2 \qquad (3.1)$$

The drawback of ESR, however, is thermal management. Steam reforming reactions are strongly endothermic and require a continuous supply of heat. In ethanol reformers, this can be provided by combustion of ethanol and/or by burning the anode off-gas of a fuel cell [4-7]. In this context, it is desirable to develop catalysts for low-temperature ESR to optimize thermal management in addition to build long life and safe reformers that can be used for portable applications. An efficient catalyst for hydrogen production from ethanol has to dissociate the C-C bond, maintain a low CO concentration and be stable under catalytic operation. A survey of the literature reveals that noble metal-based catalysts perform well for ESR [1,3,8,9]. They are stable and exhibit high activity. However, they are expensive and need high temperatures to be active (923-1023 K). The reason is that the reaction mechanism involves the decomposition of ethanol at low temperature into a mixture of hydrogen, carbon monoxide and methane (eq. 3.2), followed by the water gas shift reaction (WGS) at intermediate temperature (eq. 3.3) and, finally, the steam reforming of methane at high temperature (eq. 3.4) [10].

$$C_2H_5OH \leftrightarrows H_2 + CO + CH_4 \qquad (3.2)$$

$$CO + H_2O \leftrightarrows H_2 + CO_2 \qquad (3.3)$$

$$CH_4 + 2\ H_2O \leftrightarrows 4\ H_2 + CO_2 \qquad (3.4)$$

The reaction mechanism over nickel-based catalysts follows the same steps as over noble metal-based catalysts; however, nickel tends to sinter under ESR reaction conditions and carbon deposition occurs easily [11]. In order to carry out ESR at low temperature, a different type of catalyst is required; in particular, a catalyst that does not yield methane as an intermediate species in the reaction mechanism, which can only be reformed at high temperature. Inexpensive cobalt catalysts fulfill this requirement. Over cobalt-based catalysts, ethanol is first dehydrogenated at low temperature into a mixture of hydrogen and acetaldehyde (eq. 3.5), and then acetaldehyde reacts with steam at moderate temperature to yield mainly hydrogen and carbon oxides (eq. 3.6), or decompose into carbon monoxide and methane (eq. 3.7) [12,13]. Dimethyl ketone can be also formed via condensation of acetaldehyde. A complete network of reactions can be found in Song et al. [14]. Given the lower temperature of the overall process (673-823 K), the WGS equilibrium (eq. 3.3) favors the hydrogen yield.

$$C_2H_5OH \leftrightarrows H_2 + CH_3CHO \quad (3.5)$$

$$CH_3CHO + H_2O \leftrightarrows 3\ H_2 + 2\ CO \quad (3.6)$$

$$CH_3CHO \leftrightarrows CH_4 + CO \quad (3.7)$$

The first work on ESR over cobalt catalyst was reported by Haga et al. in 1997, where the catalytic performance of cobalt supported over Al_2O_3, SiO_2, MgO, ZrO_2 and C was described [15]. This pioneering work was followed by those of Cavallaro et al. and Llorca et al. in 2001-2002. Cavallaro reported on the ESR over Co/Al_2O_3 and Co/MgO [16]. They noticed that Co/Al_2O_3 decayed in short time because of coke deposition, whereas Co/MgO was found more stable. Llorca studied cobalt supported over a great variety of supports with different acidity and redox properties (MgO, Al_2O_3, SiO_2, TiO_2, V_2O_5, ZnO, La_2O_3, CeO_2 and Sm_2O_3) [17]. Supports with strongly acidic properties favored the dehydration of ethanol into ethylene whereas supports with basic properties favored dehydrogenation of ethanol into acetaldehyde (eq. 3.5). The same conclusion was reached by Kaddouri and Mazzocchia and by Batista et al. on Co/SiO_2 and Co/Al_2O_3 catalysts [18,19].

However, in contrast to noble metal-based systems, most cobalt catalysts suffer from severe deactivation during ESR due to extensive carbon deposition, particularly under realistic loads of ethanol. The search for cobalt-based catalysts for ESR that do not generate coke and therefore, do not deactivate, is an open issue. Essential for this matter is the understanding of the role of cobalt oxidation state. In situ IR spectroscopy [20], in situ magnetic measurements [21,22], in situ XPS [23], in situ XRD [24] and controlled-atmosphere XAFS [24] have revealed that Co metal particles are formed easily under reaction conditions, which rapidly detach from the catalyst support and originate carbon nanotubes, nanofibers and platelets. At the same time, methane selectivity and the amount of higher hydrocarbons increase at the expense of the reforming products (H_2 and CO_x). Several strategies have been attempted to minimize coke formation over Co-based catalysts under ESR conditions. Llorca et al. incorporated Na^+ promoter into Co/ZnO and obtained an important decrease of coke deposition during ESR, as evidenced by XPS and HRTEM, due to blocking of strong acidic sites of the support, which leads to the formation of ethylene, a well-known coke precursor [25]. A similar conclusion was reached by Kim et al. by EXAFS over the same catalysts [26]. On the other hand, remarkable efforts have been addressed by the group of Ozkan towards the Co/CeO_2 and Co/ZrO_2 systems for ESR due to the large oxygen storage capacity and high oxygen mobility exhibited by ceria and ceria-zirconia solid solutions, which are able to oxidize carbon residues and prevent extensive carbon deposition. They used DRIFT and isotopic labeling to show the mechanism of carbon removal and the involvement of water in the reaction network over these catalysts during ESR [27,28]. High S/C ratios and the presence of oxygen promoted cleaning of the Co surface under ESR for Co/CeO_2-ZrO_2, as expected [29-31]. Avila-Neto et al. used in situ temperature and spatial resolved XANES to show that the Co^{2+}/Co^0 ratio in Co/Al_2O_3 modified with La_2O_3 and CeO_2 can be tuned by choosing appropriate water and oxygen partial pressures to approach stable catalysts for ESR operation [32]. Rybak et al. pointed out that the ZrO_2/CeO_2 ratio exerts significant influence on coke formation under ESR [33]. Enhanced oxygen mobility in CeO_2 was achieved by Song and Ozkan by Ca^{2+} incorporation, which originated unit cell expansion in the ceria lattice and improved catalytic performance in ESR as well [34]. The influence of the preparation method on the reducibility of Co/Ce-Zr-O catalysts has been also reported [35-38]. A proper metal-support interaction allows only partial

reduction of cobalt and leads to a superior catalytic performance for the production of hydrogen through ESR.

It is generally accepted that metallic cobalt is an active species for the ESR, being essential for the reaction, but it has been also demonstrated that Co^{2+} plays an important role for ESR [39-42]. Busca *et al.* found that the presence of oxidized cobalt increased the selectivity towards H_2 and CO_2 over Ni-Co-Zn-Al catalysts [43]. Their data suggested that the less reduced the surface, the more favored is the conversion of ethanol into acetic acid, likely through ethoxy groups and acetaldehyde. Acetic acid and its adsorbed forms as acetate species may be converted to CO_2 on a less reduced surface, while they mostly decompose to methane and CO_x on a highly reduced catalyst. Recently, Espinal et al. have performed detailed in situ XPS, HRTEM, XRD and magnetic characterization of catalysts derived from Co/Mg/Al hydrotalcites and found that no metallic cobalt is formed under ESR at 823 K [44]. This interesting result allows designing catalysts containing cobalt for ESR without coke deposition (no metallic cobalt) by placing in appropriate environments Co^{2+} active species. A similar conclusion has been reached by Da Costa-Serra and Chica using delaminated zeolite as Co support [45]. Over K^+-doped hydrotalcite-derived cobalt catalysts Espinal et al. [46] have reported stable operation for 300 h under high loads of ethanol and commercial bioethanol at 823 K.

Finally, alloying cobalt with more electronegative elements such as Ni or Cu results in worse catalytic performance for ESR, whereas alloying cobalt with the less electronegative elements Fe [47-49] and Mn [50,51] promotes the redox pair $Co^0 \leftrightarrows Co^{2+}$, both in terms of a lower cobalt reduction temperature as well as a fast re-oxidation, which in turn results in a better catalytic stability. Also, the addition of Fe and Mn promoters hinders acetaldehyde decomposition (eq. 3.7) and less methane is formed as byproduct [52]. Noble metal (Pt, Pd, Rh, Ru, Ir)-promoted cobalt catalysts have been also investigated for ESR [53,54]. The effects of the noble metals include a marked lowering of the reduction temperature of the cobalt surface species interacting with the support due to hydrogen spillover and the stabilization of Co sites in the reduced state throughout the reaction. This causes an enhancement of catalytic activity, but in most cases a rapid deactivation by coke deposition is observed.

In this work, we have extended our work on hydrotalcite-derived cobalt catalysts by studying the effect of Pt and Rh addition on the catalytic performance for ESR under practical conditions. To that end, we have used catalytic honeycombs instead of conventional powdered or pelletized samples because they are robust, easy to scale up and replace, and offer homogeneous flow distribution patterns with low pressure drop, which constitute critical aspects for the development of fuel reformers [4,5,55-59]. The hydrotalcite with molar composition Co:Mg:Al=1:2:1 was chosen to be doped with noble metals because it showed the best catalytic performance in the former study [44]. The aim of the noble metal doping was to increase catalytic activity. Rh was chosen as this metal is the most effective with respect to ethanol conversion and hydrogen selectivity, due to its strong capacity to successfully dissociate the C-C bond of the ethanol molecule [60,61]. Pt was chosen because it promotes the WGS reaction and it is active and selective towards H_2 production [62].

3.2. Experimental

3.2.1. Catalyst preparation

The Co/Mg/Al hydrotalcite with formula $[Co_2Mg_4Al_2(OH)_{16}]CO_3 \cdot 4H_2O$ (Co:Mg:Al molar ratio=1:2:1) was prepared by the co-precipitation method. Briefly, aqueous solutions of an appropriate amount of $Co(NO_3)_2 \cdot 6H_2O$, $Mg(NO_3)_2 \cdot 6H_2O$ and $Al(NO_3)_3 \cdot 9H_2O$ precursors and 2M NaOH alkaline solution were separately prepared. These solutions were simultaneously added drop-wise into 100 ml of deionized water maintaining a constant pH (10±0.5) under vigorous mechanical stirring. After the co-precipitation, the suspension was aged overnight under stirring at room temperature, filtered, and thoroughly washed with deionized water. The resulting solid was dried overnight at 373 K and calcined at 823 K for 12 hours to obtain the hydrotalcite-derived mixed oxide.

Noble metal (Rh and Pt) addition to the calcined hydrotalcite (over the same batch) was accomplished by impregnation with 0.2 M aqueous solutions of H_2PtCl_6 and $RhCl_3$. Three samples with different amount of Rh were prepared: 0.1, 0.3 and 0.5 wt. %, referred to the nominal cobalt content. Four samples with different amount of Pt were prepared:

0.1, 0.3, 0.5 and 1.0 wt. %, referred to the nominal cobalt content. The resulting materials were dried at 373 K and calcined at 823 K for 4 hours. Rh and Pt were introduced after the formation and calcination of the hydrotalcite, instead of co-precipitating the noble metal salt together with the other metal salts or instead of impregnating the hydrotalcite previous to calcination to favor its deposition at the surface of the mixed oxide. The samples will be referred from now on as CoHT (reference sample with no noble metal), 0.1Pt-CoHT, 0.3Pt-CoHT, 0.5Pt-CoHT, 1Pt-CoHT, 0.1Rh-CoHT, 0.3Rh-CoHT and 0.5Rh-CoHT, according to their noble metal promoter and amount, referred to the nominal cobalt content.

The catalyst powders were deposited onto cordierite supports (400 cells per square inch) by the washcoating method. Honeycombs were from Rauschert Company, with a nominal chemical composition of $Al_3Mg_2AlSi_5O_{18}$. They were cut into cylindrical pieces of 1.8 cm in diameter and 2 cm long. A 5:1 molar mixture of polyvinyl alcohol (PVA) and acetic acid was used as binding agent. The resulting catalytic honeycombs were dried at 363 K for 2 hours and calcined at 823 K for 3 hours. The washcoating procedure was repeated several times until the catalyst loading was ca. 10 % with respect to the cordierite support (1.5 $mg \cdot cm^2$).

3.2.2. Catalytic tests

Ethanol steam reforming (ESR) was carried out in the temperature range 523-823 K (every 50 K) at atmospheric pressure in a tubular stainless-steel reactor over the catalytic honeycombs without any pre-treatment. The reaction was first tested with a gaseous H_2O:CH_3CH_2OH=4:1 molar mixture (steam to carbon, S/C=2) by using a nitrogen stream saturated with the reactants ($7 \cdot 10^{-4}$ $g_{EtOH} \cdot min^{-1}$, W/F=10^4 $g \cdot min \cdot mol_{EtOH}^{-1}$). Stability tests were then conducted at 823 K with pure liquid mixtures of absolute ethanol (Sigma-Aldrich)-water provided directly with a Knauer Smartline HPLC pump (S/C=2, 0.018 $g_{EtOH} \cdot min^{-1}$, W/F=400 $g \cdot min \cdot mol_{EtOH}^{-1}$). The liquid mixture was vaporized at 450 K before entering the reactor. The reactor effluent was monitored on-line every 5 minutes by gas chromatography (Agilent 3000 A) using MS 5 Å, Plot U and Stabilwax columns. On the other hand, 0.5Pt-CoHT and 0.5Rh-CoHT powder samples were

subjected to ESR at 823 K for 8 h with pure liquid mixture in a similar manner than monoliths, to enable extra ex situ characterization. The resulting samples, both monoliths and powder, are labeled from now on as *xxx*-CoHT-reac.

3.2.3. Characterization techniques

X-ray diffraction (XRD) patterns were collected between 10 and 90° of 2θ using a Bruker D8 instrument equipped with Cu K_α incident radiation (λ=1.5404 Å) and a graphite monochromator. Diffractograms were recorded with a step width of 0.02° and a step time of 1.5 s.

X-ray photoelectron spectroscopy (XPS) was performed with a SPECS system equipped with an Al anode XR50 source operating at 150 W and a Phoibos 150 MCD-9 detector. Sample powders were pressed to pellets and then fixed into a special sample holder (no glue was used). Spectra were recorded with pass energy of 25 eV at 0.1 eV steps at a pressure below $5 \cdot 10^{-12}$ bar; binding energies were referred to the C 1s signal.

Temperature programmed reduction (TPR) was performed in a Catalyst Analyzer BELCAT-M (BEL Japan, Inc.). Prior to each TPR run, samples were heated up to 823 K (10 $K \cdot min^{-1}$) and cooled down to room temperature under argon. Then, they were analyzed by heating up to 1173 K (10 $K \cdot min^{-1}$) using hydrogen (10 vol. % in argon) under a flow rate of 30 $ml \cdot min^{-1}$.

Scanning electron microscopy (SEM) was carried out with a Neon40 Crossbeam Station (Zeiss) equipped with a field emission electron source. Samples were deposited on a metallic disk holder and covered with a thin Au layer before analysis.

Magnetization (M) vs. applied magnetic field (H) (at 5 and 298 K) and ZFC-FC curves (at 50 Oe) were measured with a superconducting quantum interference device (SQUID) magnetometer (Quantum Design MPMS5XL). A given amount of powder was confined in a gelatin capsule (of known mass) and pressed with a given amount of cotton to avoid the powder from moving during the measurement. The diamagnetic contributions of the capsule and the cotton were subtracted from the total magnetization (m_{total}) as follows:

$$M_{powder}\left(\frac{emu}{g}\right) = \frac{m_{total}(emu) - (\chi_{capsule} \cdot mass_{capsule} + \chi_{cotton} \cdot mass_{cotton})}{mass_{powder}(g)}$$

where χ is the magnetic susceptibility in cgs units: χ(capsule)=-3.39·10^{-7} emu·g^{-1}·Oe^{-1} and χ(cotton)=-7.79·10^{-7} emu·g^{-1}·Oe^{-1}.

3.3. Results and discussion

3.3.1. Ethanol steam reforming

All catalytic honeycombs loaded with hydrotalcite-derived cobalt catalysts promoted with different amounts of Pt and Rh performed well for the steam reforming of ethanol under the conditions tested in this work. Table 3.1 compiles the ethanol conversion values for each catalytic honeycomb attained in the 673-823 K temperature range as well as selectivity values on a dry basis at S/C=2, W/F=10^4 g·min·mol$_{EtOH}^{-1}$ and VHSV=850 h^{-1}. It merits to be highlighted that, under the same operation conditions, catalytic honeycombs containing noble metal exhibited higher activities with respect to the non-promoted sample CoHT. This is particularly visible when comparing the selectivity towards acetaldehyde, which is the first intermediate of the reforming process (eq. 3.5), under near or complete ethanol conversion at 723 K for the different samples. At this temperature, the acetaldehyde selectivity is remarkably higher for the non-promoted sample CoHT (28.2 %) with respect to samples promoted with Pt (between 0 and 7.9 %, depending on the Pt content) and to samples promoted with Rh (between 0 and 5.6 %, depending on the Rh content). Therefore, noble metal addition to hydrotalcite-derived cobalt catalysts results in a significant enhancement of the reforming capability and, in particular, promotes the transformation of acetaldehyde. This is in accordance with the results reported by Profeti et al. over noble-metal promoted Co/Al_2O_3 and Co supported over magnesium aluminate catalysts [53,54]. Catalytic honeycombs 1Pt-CoHT and 0.5Rh-CoHT exhibited the best activity in terms of both ethanol and acetaldehyde conversion in the range of temperature considered. For each family of catalysts, the higher the noble metal content the higher the catalytic activity. However, samples promoted with noble metals yielded progressively higher amounts of methane (up to about 5.5 %) at

increasing noble metal content, meaning that the decomposition of acetaldehyde (eq. 3.7) was favored with respect to the non-promoted Co sample, where the highest methane selectivity achieved was only 1.9 %. Interestingly, addition of Pt and Rh promoted the WGS reaction (eq. 3.3) at low temperature and higher CO_2/CO ratios were measured in comparison to the non-promoted sample. On the other hand, the amount of CO increased at the expense of CO_2 and H_2 at increasing temperature, as expected from thermodynamics. The formation of dimethyl ketone, a secondary product resulting from the aldol condensation of acetaldehyde [17], was enhanced in promoted catalysts with low noble metal content, whereas was progressively inhibited at higher noble metal content values, where the occurrence of dimethyl ketone was lower than that obtained over the non-promoted cobalt catalyst. In all cases, the amount of ethylene, a well-known coke precursor in ESR, was kept low at 773-823 K, particularly for Rh-bearing samples. No other hydrocarbons were detected among the reaction products.

Catalyst	T	$EtOH_{conv}$	Selectivity (%)						
	(K)	(%)	H_2	CO_2	CO	CH_4	CH_3CHO	$(CH_3)_2CO$	C_2H_4
0.1Pt-CoHT	673	59.4	46.4	5.8	4.3	1.4	30.4	7.2	4.3
	723	93.4	53.1	11.1	2.2	1.4	7.9	18.4	6.0
	773	100	65.0	11.9	13.6	1.9	-	6.0	1.6
	823	100	67.4	10.3	19.9	2.3	-	-	-
0.3Pt-CoHT	673	59.1	47.8	6.7	3.7	1.5	25.4	11.2	3.7
	723	99.4	67.3	11.8	13.6	2.8	0.3	3.5	0.7
	773	100	69.0	13.1	15.5	2.4	-	-	-
	823	100	65.2	11.2	19.8	3.8	-	-	-
0.5Pt-CoHT	673	61.1	49.4	7.1	3.9	1.9	24.7	10.4	2.6
	723	97.4	55.7	11.4	5.7	1.5	3.7	18.2	3.7
	773	100	67.7	13.2	16.2	3.0	-	-	-
	823	100	65.3	11.4	19.4	3.9	-	-	-
1Pt-CoHT	673	68.9	48.7	6.6	4.6	2.6	25.0	9.9	2.6
	723	100	67.9	17.3	9.8	5.0	-	-	-
	773	100	66.2	14.9	14.2	4.6	-	-	-
	823	100	65.4	12.0	19.0	3.5	-	-	-
0.1Rh-CoHT	673	5	47.2	6.9	3.0	1.3	29.9	9.1	2.6
	723	92.6	54.6	11.7	1.8	1.4	5.6	20.4	4.5
	773	100	55.4	13.5	2.7	2.1	0.1	22.4	3.7
	823	100	67.0	8.6	21.7	2.4	-	-	0.3
0.3Rh-CoHT	673	52.3	47.0	4.7	5.1	2.6	31.2	6.8	2.6
	723	100	68.9	15.2	10.5	5.4	-	-	-

	773	100	67.9	13.2	14.1	4.9	-	-	-
	823	100	65.4	11.1	19.4	4.2	-	-	-
0.5Rh-CoHT	673	72.6	51.7	5.9	7.8	3.4	23.4	6.9	0.9
	723	100	65.1	16.5	10.3	8.0	-	-	-
	773	100	64.4	14.3	14.3	7.0	-	-	-
	823	100	63.4	10.9	20.2	5.5	-	-	-
CoHT	673	66	38.7	22.6	6.1	-	32.7	-	-
	723	98.8	46.4	6.7	1.1	0.5	28.2	9.9	7.1
	773	100	69.5	10.8	16.6	1.6	-	1.4	0.1
	823	100	69.0	9.1	20.0	1.9	-	-	-
Equilibrium	823	-	59.7	20.3	6.3	13.7	-	-	-

Table 3.1 Ethanol conversion and distribution of products on a dry basis obtained at W/F=104 g min mol_{EtOH}^{-1} and S/C = 2 over catalytic honeycombs with 1.5 mg_{cat} cm^{-2}

Catalytic honeycombs were subsequently tested at 823 K for 8 h under high reactant loads by using an undiluted ethanol-water mixture provided directly by a liquid injection pump (S/C=2, W/F=400 g·min·mol_{EtOH}^{-1}, VHSV=600 h^{-1}). In all cases, total conversion of ethanol was achieved and constant selectivity values were maintained at about 64 % H_2, 22 % CO_2, 6 % CO and 8 % CH_4. As a representative example, Figure 3.1 shows the stability of the catalytic honeycombs 0.5Pt-CoHT and 0.5Rh-CoHT over time on stream. Similar yields of hydrogen (measured as $100 \cdot F_{H2,out}/6 \cdot F_{EtOH,in}$) of about 85 % were obtained in both cases, as well as with the other catalyst formulations. It is important to recall that these values are significantly different from those corresponding to equilibrium (Table 3.1). In particular, the selectivity towards methane was lower than that predicted by thermodynamic equilibrium. This is due to the reaction mechanism, which does not proceed via decomposition of ethanol into hydrogen, carbon monoxide and methane (eq. 3.2), which is the main path over noble metals as explained in the introduction section, but via the acetaldehyde route (eq. 3.5), which is characteristic of cobalt-based systems, as discussed above. Also, the amount of carbon dioxide produced is higher than that expected from equilibrium, which points to CO_2 as a primary product of the reaction, as has been already reported in other cobalt-based catalysts [20,22,23].

At the end of the stability tests, catalytic honeycombs were weighted in order to check for carbon deposition. Carbon accumulation was severe in all the honeycombs loaded

with hydrotalcite-derived cobalt samples promoted with noble metals, 0.01-0.1 $g_C \cdot g_{cat}^{-1} \cdot h^{-1}$ (Table 3.2). Noticeably, samples promoted with Pt accumulated more carbon than their corresponding Rh counterparts. In contrast, the amount of carbon deposited over the CoHT-reac sample (non-promoted catalyst) under the same operating conditions was considerably minor, 0.002 $g_C \cdot g_{cat}^{-1} \cdot h^{-1}$ [44].

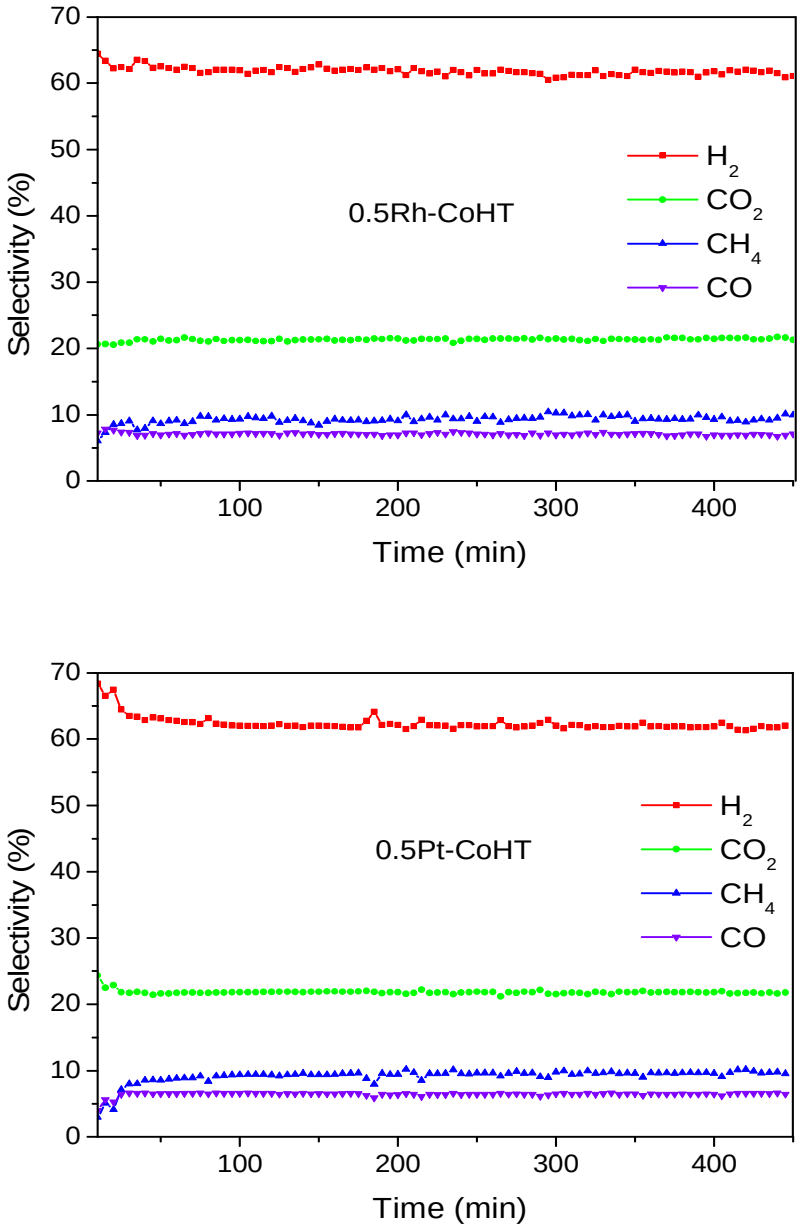

Fig. 3.1 Product selectivity versus time at 823 K with 100 % EtOH conversion obtained over catalytic honeycombs 0.5Pt-CoHT and 0.5Rh-CoHT. S/C = 2, 0.018 g_{EtOH} min^{-1}, W/F=400 $g \cdot min \cdot mol^{-1}_{EtOH}$.

Catalyst	$g_C g_{cat}^{-1} h^{-1}$
0.1Pt-CoHT	0.017
0.3Pt-CoHT	0.040
0.5Pt-CoHT	0.031
1Pt-CoHT	0.096
0.1Rh-CoHT	0.018
0.3Rh-CoHT	0.012
0.5Rh-CoHT	0.013
CoHT	0.002

Table 3.2 Carbon accumulated over honeycombs loaded with hydrotalcite-derived cobalt samples promoted with noble metals.

3.3.2. Characterization of samples before and after ESR

Ethanol steam reforming (ESR) was carried out over catalytic honeycombs calcined at 823 K since it is well known that thermal decomposition of Mg-Al hydrotalcites leads to a well dispersed mixture of magnesium and aluminum oxides with basic properties, which are favorable for the dehydrogenation of ethanol into acetaldehyde, the first step of ESR over Co-based systems (eq. 3.5). X-ray diffraction (XRD) profiles and magnetization measurements of the calcined samples doped with Pt and Rh (not shown) were virtually identical and indistinguishable from those of non-promoted hydrotalcite-derived cobalt catalyst, CoHT. In all cases, the samples are comprised by an intimate mixture of Co_2AlO_4 spinel and (Co,Mg)O solid solution, in accordance with previous works [44,46].

Thermal programmed reduction (TPR) profiles are depicted in figure 3.2 The TPR profile of the non-promoted sample, CoHT, shows two peaks. The first one, which corresponds to the reduction of Co^{3+} to Co^{2+} [44], is centered at about 710 K. The second peak appears between 1058 K and 1137 K and corresponds to the total reduction of Co^{2+} to Co^0 [44]. The consumption of hydrogen corresponding to the second peak is ca. four times higher than that associated with the first peak, as expected from the stoichiometry of cobalt spinel ($Co^{II}Co^{III}AlO_4$) and/or a mixture of cobalt in other spinels and CoO. The reducibility of cobalt is strongly influenced by the presence of Pt and Rh, even in small amounts. In the samples with the lowest noble metal content, 0.1 wt. % with respect to Co, in addition to these two reduction peaks there are also new

hydrogen uptakes at lower temperatures. Two new reduction peaks appear at 628 K and 563 K for sample 0.1Pt-CoHT and at 663 K and 563 K for sample 0.1Rh-CoHT. The low-temperature hydrogen uptake becomes progressively more important as the content of the noble metal promoter increases. In Pt-promoted samples, the temperature of the maximum of the second peak corresponding to the reduction of Co^{2+} to Co^{0} decreases as the nominal amount of platinum increases, from 1123 K to 868 K, whereas the temperature of the maximum of the low-temperature peak corresponding to the reduction of Co^{3+} to Co^{2+} stabilizes at 518 K. In Rh-promoted samples, the low-temperature hydrogen uptake stabilizes at 528 K whereas the reduction of Co^{2+} to Co^{0} occurs in two steps at 903-943 K and 1058-1088 K. It is well known that noble metals facilitate reduction of cobalt via the spillover effect in bimetallic catalysts [64]. Therefore, under the ethanol steam reforming conditions tested in this work (523-823 K), it is expected that the hydrogen produced during the reaction will completely reduce Co^{3+} and partially reduce the cobalt (II) ions to metallic cobalt in the samples promoted with Pt and Rh, depending on reaction temperature. In contrast, at the maximum reaction temperature tested, 823 K, cobalt (II) species will not undergo significant reduction in the non-promoted sample, CoHT.

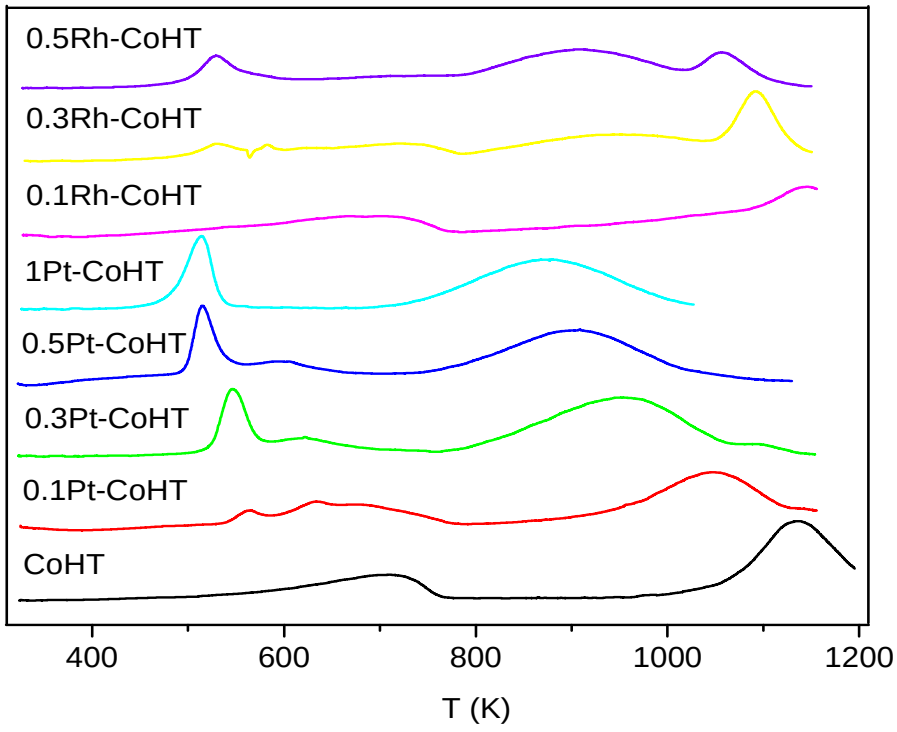

Fig 3.2 TPR profiles.

The magnetic properties of samples 0.5Pt-CoHT-reac and 0.5Rh-CoHT-reac obtained after ethanol steam reforming at 823 K were studied in detail in order to identify the magnetic phases present in the samples and, specifically, to determine the occurrence of metallic cobalt. Figure 3.3a shows the magnetization curves vs. magnetic field (M(H) curves) of sample 0.5Pt-CoHT-reac at 5 K and room temperature. Both curves are characteristic of ferromagnetic character, as evidenced by the hysteresis cycles, which indicate the presence of metallic cobalt. Coercivity at 5 K is -1475 and 1356 Oe, and at 298 K the coercivity is 460 Oe. The magnetization curve at 5 K does not saturate, even at high fields, which is attributed to the presence of a non-ferromagnetic phase. Saturation magnetization at room temperature is 29 emu·g_{Co}^{-1}. An estimation of the amount of metallic cobalt can be done considering that the bulk saturation magnetization of metallic cobalt is 163 emu·g_{Co}^{-1}, and therefore, 29 emu·g_{Co}^{-1} represents 18 % of metallic cobalt in the sample. We assume that the non-metallic cobalt in the sample corresponds to the antiferromagnetic (AFM) phase cobalt oxide, CoO, or (Co,Mg)O solid solution, according to the X-ray diffraction profile and previous works [44,46]. Sample 0.5Rh-CoHT-reac shows the same magnetic behavior than 0.5Pt-CoHT-reac (see Figure 3.3 b). The hysteresis cycles, both at low and room temperature, denotes the presence of metallic cobalt. Coercivity at 5 K is -2232 and 1891 Oe and at 298 K the coercivity is 400 Oe. Saturation magnetization at room temperature reaches 49.1 emu·g_{Co}^{-1}, which corresponds to 30 % of metallic cobalt. The inset in Figure 4b zooms on the magnetization at low applied fields. It can be clearly observed a turning point at zero field, which corresponds to a superparamagnetic or antiferromagnetic phase. We ascribe it to the cobalt oxide or (Co,Mg)O solid solution [44,46]. Figure 3.3c contains the zero field cool-field cool curves of both samples. The hysteresis up to room temperature implies, once more, the presence of a ferromagnetic phase. Magnetization of sample 0.5Pt-CoHT-reac in the field cool curve slightly decreases with temperature. This is indicative of the existence of a superparamagnetic (SPM) or AFM phase, since magnetic susceptibility in these materials is dependent on applied magnetic field and inversely proportional to temperature; in turn, magnetization is directly related to the magnetic susceptibility (M(emu/g) = χ(emu)/m(g), where M is magnetization, χ is magnetic susceptibility and m is mass). In sample 0.5Rh-CoHT-reac, magnetization decreases with temperature only at low temperature, suggesting that the amount of SPM or AFM phase

in this sample is lower than in the Pt-containing sample, in accordance with the M(H) curves. Metallic cobalt is not identified by X-ray diffraction, although this phase represents 18 % and 30 % of the cobalt content in 0.5Pt-CoHT-reac and 0.5Rh-CoHT-reac samples, respectively. This could be ascribed to a very small size of metallic cobalt particles, which would give rise to broad diffraction peaks, non-observable. It should be recalled that the samples were in contact with air during the magnetic measurements, which could partially oxidize the metallic cobalt particles. Therefore, samples under reaction conditions could have even a higher amount of reduced cobalt. The magnetic behavior of sample CoHT-reac has been reported previously and there is practically no metallic cobalt (<0.7 %) [44].

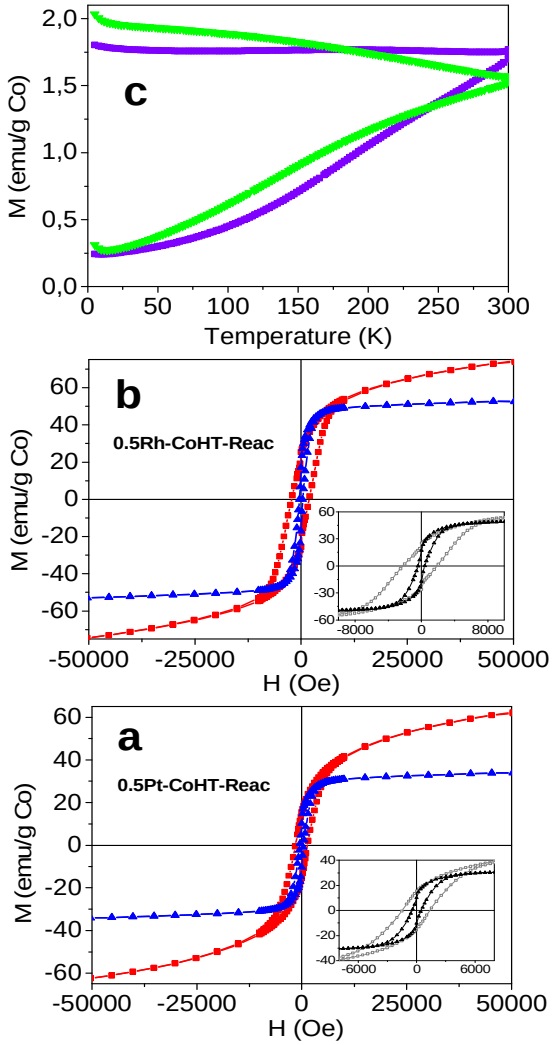

Fig. 3.3 Magnetization curves versus magnetic field applied at 5 K (red squares) and 298 K (blue line) of samples 0.5Pt-CoHTreac (a) and 0.5Rh-CoHT-reac (b). Insets zoom on low magnetic field. (c) ZFC–FC curves of samples 0.5Pt-CoHT-reac (green line) and 0.5Rh-CoHT-reac (violet line) at 50 Oe. Upper curves field cool curves. Lower curves zero-field cool curves.

X-ray photoelectron spectra of the samples promoted with 0.5 % Pt and 0.5 % Rh were analysed before and after ESR reaction in order to study the oxidation state of the cobalt atoms. The Co2p core-level is composed of two components, $Co2p_{3/2}$ and $Co2p_{1/2}$, which result from the spin orbital splitting, and shake up satellites. XP spectra of the calcined samples 0.5Pt-CoHT and 0.5Rh-CoHT have the same structure at the same energy range; there are two main peaks, the $Co2p_{3/2}$ and $Co2p_{1/2}$ photolines, and two weak satellites (figure 3.4). The main peaks as well as the satellites can be fitted to two components. The $Co2p_{3/2}$ components appear at 781.3 eV and 781.9 eV and can be assigned to oxidized cobalt species in different atomic environments. This is compatible with the existence of cobalt spinel and CoO or (Mg,Co)O, according to the magnetic measurements. As expected, there are no peaks of metallic cobalt around 777-778 eV. After ESR, the XP spectra of samples 0.5Pt-CoHT-reac and 0.5Rh-CoHT-reac share again the shape and the energy range; there are two main peaks around 781.5 eV and 797.5 eV, which correspond to the $Co2p_{3/2}$ / $Co2p_{1/2}$ spin orbital splitting, and two strong satellites. The main peaks, as well as the satellites, could be fitted again with two components. The spin orbital splitting is 16.0 eV and the separation between the satellite lines and the photo lines is close to 6 eV, indicative of high spin Co^{2+} species, like those of cobalt oxide (Co,Mg)O, and practically excluding the existence of Co^{3+} ions. A small contribution at 777.3 eV is visible in the sample 0.5Rh-CoHT-reac, indicating the presence of metallic cobalt at the surface of the catalyst. In fact, the asymmetry in the coercitive field observed in samples 0.5Pt-CoHT-reac and 0.5Rh-CoHT-reac (figure 3.4) might imply that a layer of CoO is formed over metallic cobalt entities, thus explaining the low metallic cobalt signal in the XP spectra. It has been reported that Co particles coated with CoO exhibits exchange bias effect due to interfacial interaction between ferromagnetic Co metal and antiferromagnetic CoO [65]. In situ XPS experiments reported previously revealed that no metallic cobalt was formed under ESR over the non-promoted sample CoHT-reac [44].

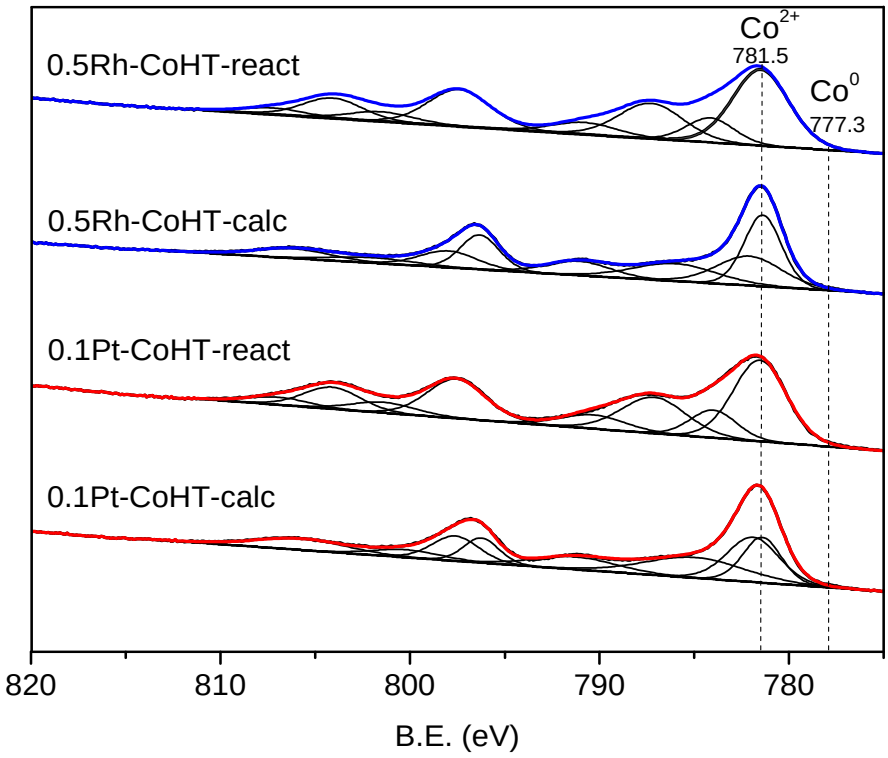

Fig. 3.4 X-ray photoelectron spectra of samples 0.5Pt-CoHT and 0.5Rh-CoHT before and after ESR.

A detailed FESEM study was performed over samples 0.5Pt-CoHT-reac, 0.5Rh-CoHT-reac and CoHT-reac. Figure 3.5 shows representative images for these samples after ESR reaction at 823 K recorded with secondary and backscattered electron detectors. Secondary electrons (SE) are useful for morphology studies whereas backscattered electrons (BE) are much sensible to atomic number differences. The morphology of all samples is similar and corresponds to an intimate mixture of round-shaped particles of nanometric size (fig. 3.5 a, 3.5 c and 3.5 e). Interestingly, the BE images reveal the presence of metallic cobalt nanoparticles as bright dots only in the samples 0.5Pt-CoHT-reac and 0.5Rh-CoHT-reac (fig. 3.5 b and 3.5 d), whereas the non-promoted catalyst CoHT does not contain them (fig. 3.5 f). The Co nanoparticles are well resolved and measure about 10-15 nm in 0.5Pt-CoHT-reac and 0.5Rh-CoHT-reac samples, thus confirming the magnetometry results. Concerning carbon deposition, SEM images recorded over both 0.5Pt-CoHT-reac and 0.5Rh-CoHT-reac samples reveal the presence

of abundant carbon nanotubes (figure 3.6), whereas no carbon structures are recognized in the non-promoted sample CoHT-reac after ESR.

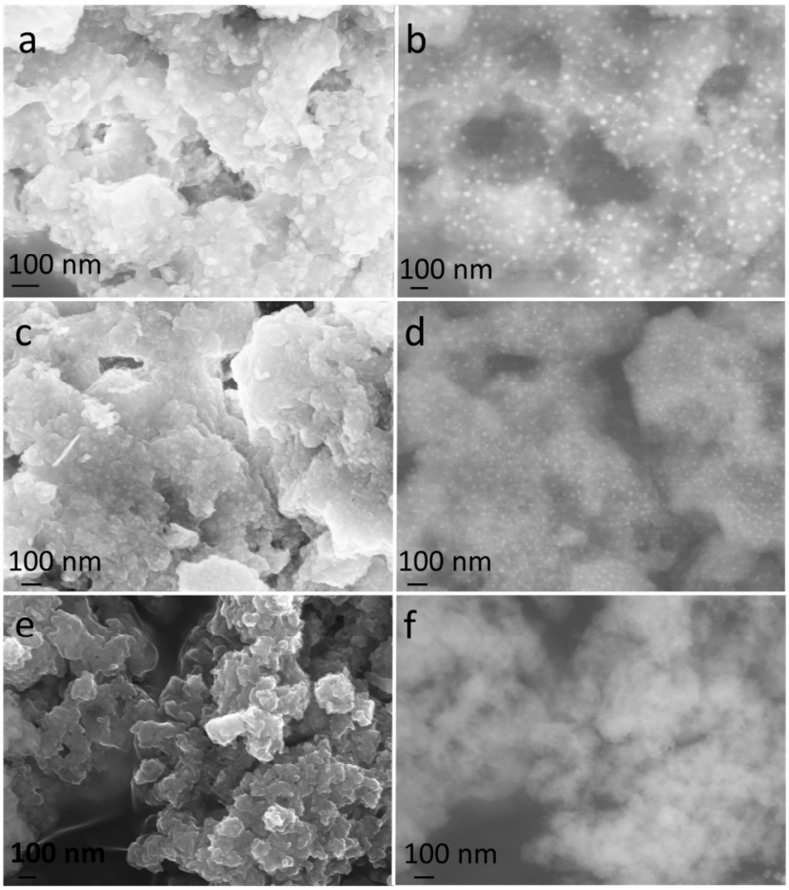

Fig. 3.5 SEM images obtained using SEs (a, c, e) and BE (b, d, f) of samples after ESR stability tests at 823 K. 0.5Pt-CoHT-reac (a, b), 0.5Rh-CoHT-reac (c, d) and CoHT-reac.

Taking into account the amount of carbon accumulated during ESR for the different catalysts (Table 2) and the characterization of samples before and after reaction by means of magnetic measurements, XPS and SEM, it is possible to conclude that carbon deposition in the form of nanotubes is directly related to the presence of metallic cobalt nanoparticles. In samples promoted with Pt and Rh, cobalt is easily reduced to form such metallic nanoparticles under reaction conditions, as deduced from TPR experiments, whereas over non-promoted catalyst cobalt remains in an oxidized state and no carbon

accumulation occurs. The calculations of percentage of metallic cobalt phase, as well as the amount of generated coke, match the results obtained previously for hydrotalcite-derived cobalt catalysts with no addition of noble metals (sample CoHT-reac) [44] and also with samples doped with potassium [46]. Hydrotalcite-derived cobalt catalysts with and without addition of potassium generate much less amount of coke than Pt- and Rh-doped samples and, in accordance, contain a significantly lesser amount of metallic cobalt after reaction (<0.7 % Co^0 compared to 18 % and 30 % Co^0 in Pt- and Rh-doped samples, respectively). These results reinforce the finding that oxidized cobalt is an active species in the ethanol reforming reaction that does not generate coke [44,46].

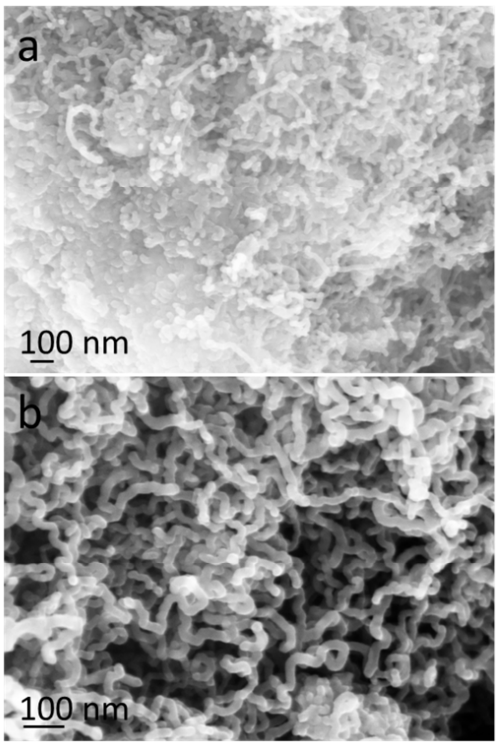

Fig. 3.6 Scanning electron microscopy images of samples 0.5Pt-CoHT-reac (a) and 0.5Rh-CoHT-reac (b) showing abundant carbon deposition.

3.4 Conclusions

Hydrotalcite-derived cobalt catalysts promoted with noble metals Pt and Rh are very active for ethanol steam reforming at moderate temperature. Total conversion of ethanol and a gas stream containing ca. 64 % H_2, 22 % CO_2, 6 % CO and 8 % CH_4 is obtained at 823 K with a direct liquid feed of ethanol-water (S/C=2, W/F=400 $g \cdot min \cdot mol_{EtOH}^{-1}$) over honeycombs loaded with 1.5 $mg_{cat}cm^{-2}$. However, metallic cobalt nanoparticles of about 10-15 nm in size evolve under reaction conditions because Pt and Rh strongly promote the reduction of cobalt by spillover effect, as determined by temperature-programmed reduction experiments, magnetic measurements, X-ray photoelectron spectroscopy and electron microscopy. These cobalt nanoparticles cause a rapid accumulation of carbon in the honeycomb channels (carbon nanotubes) under ethanol steam reforming conditions (up to ca. 0.1 $g_C \cdot g_{cat}^{-1} \cdot h^{-1}$). In contrast, hydrotalcite-derived cobalt catalysts not promoted with noble metals are less active under the same operational conditions, but are stable since almost no carbon accumulation occurs (less than 0.002 $g_C \cdot g_{cat}^{-1} \cdot h^{-1}$) because cobalt remains oxidized under ethanol steam reforming reaction. Appropriate cobalt-based catalysts for ethanol steam reforming can be designed by placing in appropriate environments Co^{2+} active species.

3.5 References

[1] A. Haryanto, S. Fernando, N. Murali and S. Adhikari, Energy F., 19, (2005), 2098-2106.

[2] P.D. Vaidya and A.E. Rodrigues, Chemical Eng. J., 117, (2006), 39-49.

[3] M. Ni, D.C.Y. Leung and M.K.H. Leung, Int. J. Hydrogen Energy, 32, (2007), 3238-3247.

[4] G. Kolb, Fuel processing for fuel cells, ed. Wiley-VCH, (2008), 1–434.

[5] J. Llorca, in Handbook of sustainable energy, ed. W. H. Lee and V. G. Cho, Nova Publishers, (2010), 693–699.

[6] M. Murdoch, G.I.N. Waterhouse, M.A. Nadeem, J.B. Metson, M.A. Keane, R.F. Howe, J. Llorca, H. Idriss, Nat. Chem., 3, (2011), 489-492.

[7] A. Casanovas, M. Saint-Gerons, F. Griffon and J. Llorca, Int. J. Hydrogen Energy, 33, (2008), 1827-1833.

[8] G. A. Deluga, J. R. Salge, L. D. Schmidt, X. E. Verykios, Renewable Hydrogen from Ethanol by Autothermal Reforming. Science, 303, (2004), 993-997.

[9] F. Frusteri and S. Freni, J. of Power Sources, 173, (2007), 200-209.

[10] H. Idriss, M. Scott, J. Llorca, S. Chan, W. Chiu, P. Sheng, A. Yee, M. Blackford, S. Pas, A. Hill, F. Alamgir, R. Rettew, C. Petersburg, S. Senanayake, M. Barteau, ChemSusChem, 1, (2008), 905-910..

[11] F. Frusteri, S. Freni, V. Chiodo, L. Spadaro, O.Di Blasi, G. Bonura, S. Cavallaro, Applied Catalysis A: General 270, (2004), 1-7.

[12] J. Llorca, P. Ramírez de la Piscina, J. A. Dalmon, N. Homs, Chem. Mater. 16, (2004), 3573-3578.

[13] V. M. Garcia, E. Lopez, M. Serra and J. Llorca, J. of Power Sources, 192, (2009), 208-215.

[14] H. Song, L. Zhang, and U.S. Ozkan, Ind. Eng. Chemistry Research, 49, (2010), 8984-8989.

[15] F. Haga, T. Nakajima, H. Miya, S. Mishima, Catal. Lett. 48, (1997), 223-227.

[16] S. Cavallaro, N. Mondello, S. Freni, J. Power Sources 102, (2001), 198-204.

[17] J. Llorca, N. Homs, J. Sales, P. Ramírez de la Piscina, J. Catal. 209, (2002), 306-317.

[18] A. Kaddouri, C. Mazzocchia, Catal. Commun. 5, (2004), 339-345.

[19] M.S. Batista, R.K.S. Santos, E.M. Assaf, J.M. Assaf, , E.A. Ticianelli, High efficiency steam reforming of ethanol by cobalt-based catalysts. J. Power Sources 134, (2004), 27-32.

[20] J. Llorca, N. Homs, P. Ramírez de la Piscina, J. Catal. 227, (2004), 556-560.

[21] J. Llorca, J. A. Dalmon, P. Ramírez de la Piscina, N. Homs, Appl. Catal. A:Gen. 243, (2003), 261-269.

[22] J. Llorca, P. Ramírez de la Piscina, J. A. Dalmon, J. Sales, N. Homs, Appl. Catal. B: Environ. 43, (2003), 355-369.

[23] M. Dominguez, E. Taboada, H. Idriss, E. Molins and J. Llorca, J. of Mat. Chemistry, 20, (2010), 4875–4883.

[24] B. Bayram, I.I. Soykal, D. von Deak, J.T. Miller, U.S. Ozkan, J. Catal. 284, (2011), 77-89.

[25] J. Llorca, N. Homs, J. Sales, J. L. G. Fierro, P. Ramírez de la Piscina, J. Catal. 222, (2004), 470-480.

[26] K.S. Kim, H.R. Seo, S.Y. Lee, J.G. Ahn, W.C. Shin, Y.K. Lee, Topics Catal. 53, (2010), 615-620.

[27] H. Song, U.S. Ozkan, J. Catal. 261, (2009), 66-74.

[28] H. Song, X. Bao, C.M Hadad, U.S. Ozkan, Catal. Lett. 141, (2011), 43-54.

[29] S.M. Lima, A.M. da Silva, L.O.O. da Costa, U.M. Graham, G. Jacobs, B.H. Davis, L.V. Mattos and F.B. Noronha, J. of Catalysis, 268, (2009), 268-281.

[30] J. C. Vargas, S. Libs, A. C. Roger and A. Kiennemann, Catal. Today, 107, (2005), 417-425.

[31] H. Song, L. Z. Zhang, R. B. Watson, D. Braden and U. S. Ozkan, Catal. Today, 129, (2007), 346-354.

[32] C.N. Avila-Neto, J.W.C. Liberatori, A.M. da Silva, D. Zanchet, C.E. Hori, F.B. Noronha, J.M.C. Bueno, J. Catal. 287, (2012), 124-137.

[33] P. Rybak, B. Tomaszewska, A. Machocki, W. Grzegorczyk, A. Denis, Catal. Today 176, (2011), 14-20.

[34] H. Song, U.S. Ozkan, J. Phys. Chem. A 114, (2010), 3796-3801.

[35] S.S.Y. Lin, D.H. Kim, S.Y. Ha, Appl. Catal. A:Gen. 355, (2009), 69-77.

[36] H. Song, T. Bing and U.S. Ozkan, Cat. Lett., 132, (2009), 422-429.

[37] H. Wang, J. L. Ye, Y. Liu, Y. D. Li and Y. N. Qin, Catal. Today, 129, (2007), 305-312.

[38] M. Benito, R. Padilla, A. Serrano-Lotina, L. Rodríguez, J.J. Brey, L. Daza, J. Power Sources 192, (2009), 158-164.

[39] J. Llorca, N. Homs, P. Ramírez de la Piscina, J. Catal. 227, (2004), 556-560.

[40] E. Martono, M.P. Hyman, J.M. Vohs, Phys. Chem. Chem. Phys. 13, (2011), 9880-9886.

[41] A.M. Karim, Y. Su, M.H. Engelhard, D.L. King, Y. Wang, ACS Catal. 1, (2011), 279-286.

[42] M.P. Hyman and J.M. Vohs, Surf. Sci. 605, (2011), 383-389.

[43] G. Busca, U. Costantino, T. Montanari, G. Ramis, C. Resini and M. Sisani, Int. J. Hydrogen Energy, 35, (2010), 5356-5366.

[44] R. Espinal, E. Taboada, E. Molins, R.J. Chimentao, F. Medina and J. Llorca, RSC Advances, 2, (2012), 2946-2956.

[45] J.F. Da Costa-Serra and A. Chica, Int J Hydrogen Energy, 36, (2011), 3862-3876.

[46] Espinal R, Taboada E, Molins E, Chimentao RJ, Medina F and Llorca J, App. Cat. B: Environ., 127, (2012), 59-67.

[47] Y. Sekine, A. Kazama, Y. Izutsu, M. Matsukata, E. Kikuchi, Catal. Lett. 132, (2009), 329-334.

[48] A. Casanovas, M. Roig, C. de Leitenburg, A. Trovarelli, J. Llorca, Int. J. Hydrogen Energy 35, (2010), 7690-7698.

[49] A. Kazama, Y. Sekine, K. Oyama, M. Matsukata, E. Kikuchi, Appl. Catal. A:Gen. 383, (2010), 96-101.

[50] J. A. Torres, J. Llorca, A. Casanovas, M. Domínguez, J. Salvadó, D. Montané, J. Power Sources 169, (2007), 158-166.

[51] A. Casanovas, C. de Leitenburg, A. Trovarelli, J. Llorca, Chem. Eng. J. 154, (2009), 267-273.

[52] M. Domínguez, E. Taboada, E. Molins and J. Llorca, Catalysts, 2, (2012), 386-399.

[53] L.P.R. Profeti, P.R. Luciene, E.A. Ticianelli, A. Edson and E.M. Assaf, J. Power Sources, 175, (2008), 482-491.

[54] L.P.R. Profeti, E.A. Ticianelli, E.M. Assaf, Appl. Catal. A:Gen., 360, (2009), 17-25.

[55] A. Casanovas, C. de Leitenburg, A. Trovarelli, J. Llorca, Cat. Today, 138, (2008), 187-192.

[56] A. Casanovas, M. Dominguez, C. Ledesma, E. Lopez and J. Llorca, Cat. Today, 143, (2009), 32-37.

[57] J. Llorca, A. Casanovas, T. Trifonov, A. Rodriguez and R. Alcubilla, J. of Catalysis, 255, (2008), 228-233.

[58] E. López, A. Irigoyen, T. Trifonov, A. Rodríguez and J. Llorca, Int J Hydrog Energy, 35, (2010), 3472-3479.

[59] M. Domínguez, G. Cristiano, E. López and J. Llorca, Chem Eng J, 280, (2011), 177-177.

[60] C. Diagne, H. Idriss, A. Kiennemann, Catal. Commun. 3, (2002), 565-571.

[61] F. Romero-Sarria, J. C. Vargas, A-C. Roger, A. Kiennemann, Catal. Today, 133-135, (2008), 149-153.

[62] M. Dömök, A. Oszko, K. Baan, I. Sarusi, A. Erdohelyi, App. Catal. A: Gen. 383, (2010), 33-42.

[63] J. Llorca, P. R. de la Piscina, J. Sales and N Homs, Chem Commun, 7, (2001), 641-642.

[64] L.P.R. Profeti, E.A. Ticianelli and E.M. Assaf, J. Power Sources, 75, (2008), 482-489.

[65] J. Nogués and I. Schuller, J Magn and Magn Mater, 200, (1999), 192-203.

CHAPTER 4

Cobalt hydrotalcites as catalysts for bioethanol steam reforming. The promoting effect of potassium on catalyst activity and long-term stability

Partially published in:

"Cobalt hydrotalcites as catalysts for bioethanol steam reforming. The promoting effect of potassium on catalyst activity and long-term stability"

Raúl Espinal, Elena Taboada, Elies Molins, Ricardo J. Chimentao, Francesc Medina and Jordi Llorca

Applied Catalysis B: Environmental, 127, (2012), 59–67

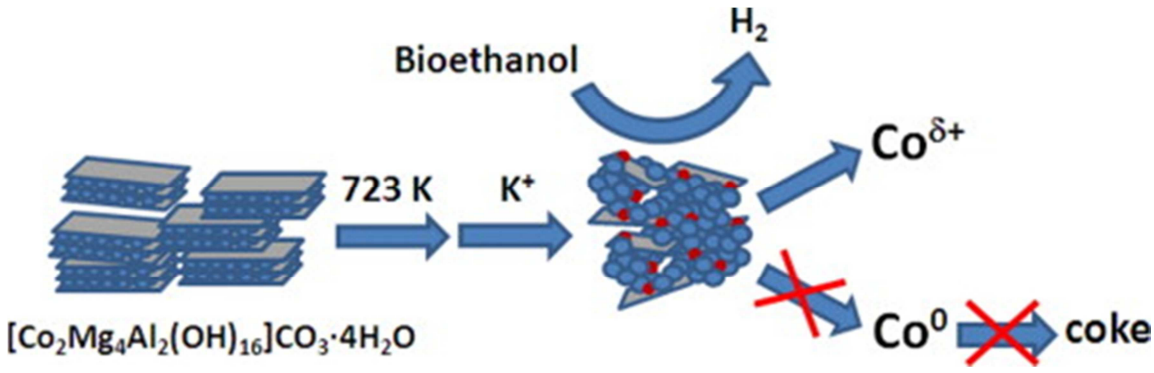

4.1 Introduction

Hydrogen production from ethanol steam reforming (ESR) reaction has great interest because it allows obtaining six molecules of hydrogen from one molecule of ethanol and three molecules of water:

$$C_2H_5OH + 3\ H_2O \rightarrow 6\ H_2 + 2\ CO_2 \qquad (4.1)$$

Bioethanol is produced from biomass fermentation, for what it is a renewable energy source. Bioethanol is then CO_2 neutral within the reforming reaction, because the carbon dioxide produced in this reaction comes from the carbon dioxide absorbed from the biomass during its growth.

For ESR, the use of suitable catalysts allows total conversion of ethanol at lower temperatures and better selectivity towards hydrogen, with reduced production of undesirable side-products. Catalysts based on noble metals are optimal to avoid coke formation [1]. However, they are very expensive and need high temperatures to be active (923-1023 K). On the other hand, cobalt-based catalysts are cheap and active at low temperatures (523-823 K), but they deactivate quickly due to coke generation. Coke formation is associated to metallic nanoparticles, which nucleate the growth of carbon nanotubes [2]. It is generally accepted that metallic cobalt is the active species for the ESR, being essential for the reaction, but also that the redox pair $Co^0 \leftrightarrows Co^{2+}$ is responsible for the activity of cobalt in ESR [3-6]. Casanovas *et al.* pointed out that the easy exchange between oxidized and reduced cobalt centres may promote catalytic activity of Co-ZnO not only in ESR but also in WGS, where water behaves both as a reactant and as an oxidant [7]. Busca *et al.* also found that the presence of oxidized cobalt increased the selectivity towards H_2 and CO_2 over Ni-Co-Zn-Al catalysts. Their data suggested that the less reduced the surface, the more favoured is the conversion of ethanol into acetic acid, likely through ethoxy groups and acetaldehyde. Acetic acid and its adsorbed forms as acetate species may be converted to CO_2 on a less reduced surface, while they mostly decompose to methane and CO_x on a highly reduced catalyst [8]. An important advantage of carrying out the ESR at moderate temperature is that WGS occurs simultaneously with steam reforming and consequently CO concentration is

kept low. In addition, methane is not an intermediate of the reforming process over Co-based catalysts and, consequently, high hydrogen yields are easy to achieve [7]. CH_4 is a secondary product formed through the methanation reaction [9].

Within this context, the search for cobalt-based catalysts for ESR that do not generate coke and therefore, do not deactivate, is an open issue. Essential for this matter is the understanding of the role of cobalt oxidation state. In one of our previous works, we studied cobalt hydrotalcites as precursors for ESR catalysts [10]. After calcination at 823 K, they are converted to cobalt spinels, which are very active. Ethanol conversion was total at 823 K, reaching 70% of hydrogen selectivity (S/C=2, W/F=390 to 10^4 g·min·mol$^{-1}_{EtOH}$) and, more interestingly, coke formation was scarce. We analysed the samples after reaction by several techniques (magnetometry, XRD, XPS, HRTEM, etc.) and we observed traces of metallic cobalt only by magnetometry (between 5.9 and 0.1 wt. % Co^0, depending on the metallic molar fraction of the hydrotalcite); no metallic cobalt was detected by X-ray diffraction, neither by *in-situ* XPS and HRTEM. Therefore, we concluded that the main active species in ESR was oxidized cobalt. This interesting result allows designing catalysts containing cobalt for ESR without coke deposition (no metallic cobalt) by placing in appropriate environments Co^{2+} active species. A similar conclusion has been reached by Da Costa-Serra and Chica [11] using delaminated zeolite as Co support.

Here, we present a further study of cobalt hydrotalcites which were doped with potassium at several weight percentages. The hydrotalcite with molar composition Co:Mg:Al=1:2:1 was chosen to be doped with potassium because it showed the better catalytic activity in the former study [10]. The aim of the potassium doping was to reduce even more the coke formation, by neutralizing the acid sites of the hydrotalcites, which are likely the responsible for ethanol dehydration into ethylene and other coke precursors. The catalysts are active for ESR, with high stability in time and scarce coke formation. Potassium acts as a promoter of the reaction, favouring the ethanol conversion at lower temperature. No metallic cobalt was observed by XPS after reaction and less than 0.1 wt. % by magnetometry. Then, oxidized cobalt appears once more as an active species for ethanol reforming. The catalytic tests were directly carried out over monoliths washcoated with the catalysts to simulate practical application. For the same

reason, the performance of the catalytic monoliths was also tested with commercial bioethanol.

4.2 Experimental

4.2.1. Catalyst preparation

The Co/Mg/Al hydrotalcite with formula $[Co_2Mg_4Al_2(OH)_{16}]CO_3 \cdot 4H_2O$ (Co:Mg:Al molar ratio=1:2:1) was prepared by the co-precipitation method. Briefly, aqueous solutions of an appropriate amount of $Co(NO_3)_2.6H_2O$, $Mg(NO_3)_2.6H_2O$ and $Al(NO_3)_3.9H_2O$ precursors and 2M NaOH alkaline solution were separately prepared. These solutions were then simultaneously added drop-wise into 100 ml of deionised water maintaining a constant pH (10±0.5) under vigorous mechanical stirring. After the co-precipitation, the suspension was aged overnight under stirring at room temperature, filtered, and thoroughly washed with deionised water. The resulting solid was then dried overnight at 373 K and calcined at 723 K for 12 hours to obtain the hydrotalcite-derived mixed oxides.

Potassium addition to the calcined hydrotalcite (over the same batch) was accomplished by impregnation with a 0.032 M KOH aqueous solution. Three samples with different amount of potassium were prepared: 0.5, 1.0 and 2.0 wt. %, referred to the nominal cobalt content. The resulting materials were dried at 373 K and calcined at 723 K for 4 hours. The potassium was introduced after the formation and calcination of the hydrotalcite, instead of co-precipitating the potassium salt together with the other metal salts or instead of impregnating the hydrotalcite previous to calcination, to favour its deposition at the surface of the mixed oxides. The samples will be referred from now on as 0K_calc (reference sample with no potassium), 0.5K_calc, 1K_calc and 2K_calc, respectively.

The calcined hydrotalcites were deposited onto cordierite supports (400 cells per square inch) by the washcoating method. Honeycombs were from Rauschert Company, with a nominal chemical composition of $Al_3Mg_2AlSi_5O_{18}$. They were cut into cylindrical pieces of 1.8 cm in diameter and 2 cm long. A 5:1 molar mixture of polyvinyl alcohol (PVA) and acetic acid was used as binding agent. The resulting catalytic honeycombs were dried at

363 K for 2 hours and calcined at 823 K for 3 hours. The washcoating procedure was repeated several times until the catalyst loading was ca. 5% with respect to the cordierite support.

4.2.2. Catalytic tests

Ethanol steam reforming (ESR) was carried out in the temperature range 523-823 K (every 50 K) at atmospheric pressure in a tubular stainless-steel reactor over the catalytic honeycombs without any pre-treatment. The reaction was first tested with a gaseous H_2O:CH_3CH_2OH=4:1 molar mixture (steam to carbon, S/C=2) by using a nitrogen stream saturated with the reactants ($8.0 \cdot 10^{-5}$ $g_{EtOH} \cdot min^{-1}$, W/F=$13.4 \cdot 10^3$ $g \cdot min \cdot mol_{EtOH}^{-1}$). Stability tests were then conducted at 823 K with pure liquid mixtures of absolute ethanol (Sigma-Aldrich) and commercial bioethanol (Deulep), provided directly with a Knauer Smartline HPLC pump (the liquid mixture was vaporized at 450 K before entering the reactor; S/C=2, 0.018 $g_{EtOH} \cdot min^{-1}$ for 7 h long stability tests and 0.036 $g_{EtOH} \cdot min^{-1}$ for 300 h long stability tests). VHSV values ranged from 325 to 625 h^{-1} and W/F values ranged from 475 to 115 $g \cdot min \cdot mol_{EtOH}^{-1}$, for 7 and 300 h, respectively. The reactor effluent was monitored on-line every 5 minutes by gas chromatography (Agilent 3000 A) using MS 5 Å, Plot U and Stabilwax columns. On the other hand, 0K_calc, 0.5K_calc, 1K_calc and 2K_calc powder samples were subjected to ESR at 823 K for 8 h with pure liquid mixture in a similar manner than monoliths, to enable extra characterization. The resulting samples, both monoliths and powder, were labelled as 0K_reac, 0.5K_reac, 1K_reac and 2K_reac.

4.2.3. Characterization techniques

X-ray diffraction (XRD) patterns of the calcined catalysts in powder form were collected between 10 and 90° of 2θ using a Bruker D8 instrument equipped with Cu Kα incident radiation (λ = 1.5404 Å) and a graphite monochromator. The reacted samples were analysed between 5 and 60° of 2θ, using a Rigaku Rotaflex RU-200 B, also equipped with a Cu target. All the diffractograms were recorded with a step width of 0.02° and a step time of 1 s.

X-ray photoelectron spectroscopy (XPS) was performed with a SPECS system equipped with an Al anode XR50 source operating at 150 W and a Phoibos 150 MCD-9 detector. Sample powders were pressed to pellets and then fixed into a special sample holder (no glue was used). Spectra were recorded with pass energy of 25 eV at 0.1 eV steps at a pressure below $6 \cdot 10^{-12}$ bar; binding energies were referred to the C 1s signal

Temperature programmed desorption of ammonia (TPD-NH_3) was performed in a Catalyst Analyzer BELCAT-M (BEL Japan, Inc.), equipped with a thermal conductivity detector (TCD). The samples were pre-treated under argon, heated up to 723 K (10 K·min^{-1}) maintained at 723 K for 1 hour and cooled down to 373 K. Then, the sample was saturated with pure NH_3 for 10 minutes (30 ml·min^{-1}). After this step, in order to drag out the excess of ammonia (the non-interacting with the catalyst) the sample was flushed with argon at 373 K, until the TCD signal was stabilized. Analysis was then performed by heating up to 1173 K (10 K·min^{-1}) under argon. The evolution of gases was also monitored by mass spectrometry, with a Cirrus spectrometer from MKS spectra products, equipped with a multiplier detector.

Temperature programmed reduction (TPR) was performed also in a Catalyst Analyzer BELCAT-M (BEL Japan, Inc.). Prior to each TPR run, samples were heated up to 823 K (10 K·min^{-1}) and cooled down to room temperature under argon. Then, they were analyzed by heating up to 1173 K (10 K·min^{-1}) using hydrogen (10 vol% in argon) under a flow rate of 30 ml·min^{-1}.

Magnetization (M) vs. applied magnetic field (H) (at 5 and 298 K) and ZFC-FC curves (at 50 Oe) were measured with a superconducting quantum interference device (SQUID) magnetometer (Quantum Design MPMS5XL, USA). A given amount of powder was confined in a gelatin capsule (of known mass) and pressed with a given amount of cotton to avoid the powder from moving during the measurement. The diamagnetic contributions of the capsule and the cotton were subtracted from the total magnetization (m_{total}) as follows:

$$\mathrm{M_{powder}}\left(\frac{\mathrm{emu}}{\mathrm{g}}\right) = \frac{\mathrm{m_{total}(emu)} - (\chi_{\,\mathrm{capsule}} \cdot \mathrm{mass}_{\,\mathrm{capsule}} + \chi_{\,\mathrm{cotton}} \cdot \mathrm{mass}_{\,\mathrm{cotton}})}{\mathrm{mass_{powder}(g)}}$$

where χ is the magnetic susceptibility in cgs units: χ(capsule)=-3.39·10^{-7} emu·g^{-1}·Oe^{-1} and χ(cotton)=-7.79·10^{-7} emu·g^{-1}·Oe^{-1}.

4.3. Results and discussion

4.3.1. Calcined hydrotalcites

The calcined samples were analysed by X-ray diffraction (see Figure 4.1). The XRD profiles of the four samples are identical, indicating that the addition of potassium in the studied range does not affect the crystalline phases of the calcined hydrotalcites (compare the XRD profile of the sample 0K_calc with those of the samples with potassium). Taking into account the stoichiometry of the parent hydrotalcite structure, these compounds are formed by a A(II)B(III)$_2$O$_4$ spinel and A(II)O oxide, where A=Mg^{2+}/Co^{2+} and B=Co^{3+}/Al^{3+} [12]. From the information compiled in Figure 4.1 it is deduced that the main peaks of the diffractograms can be indexed to $MgAl_2O_4$ and/or Co_2AlO_4 spinels [13, 14] (XRD patterns JCPDS 01-075-1798 and JCPDS 00-038-0814, respectively). In addition, the two shoulders at 43° and 63° of 2θ match the main peaks of the rock salt type phase common to MgO and CoO [15, 16] (XRD patterns JCPDS 01-07-1525 and JCPDS 01-075-0533, respectively), suggesting the incipient formation of the simple oxides or the double oxide.

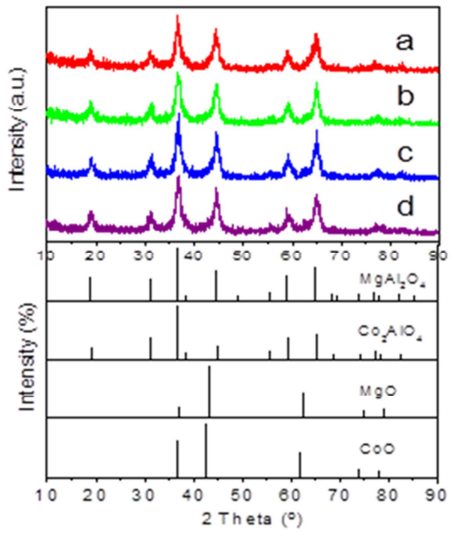

Fig. 4.1 X-ray diffractograms of samples (a) 0K calc, (b) 0.5K calc, (c) 1K calc and (d) 2K calc. XRD patterns of several spinel and oxide phases are included for comparison.

XP spectra of the calcined samples were analysed in order to determine the oxidation state of the cobalt atoms and to determine the atomic ratio between cobalt and potassium. According to the literature, the Co2p core-level is composed of two components, $Co2p_{3/2}$ and $Co2p_{1/2}$ (which result from the spin orbital splitting) and shake up satellites. XP spectra of the four calcined samples have the same structure at the same energy range: there are two main peaks, the $Co2p_{3/2}$ and $Co2p_{1/2}$ photolines, and two weak satellites. The main peaks can be fitted to two components, and the satellites as well (see Figure 4.2). A Fe LMM line due to the sample holder is also detected. The first $Co2p_{3/2}$ component appears at 780.5 eV and can be assigned to an oxidized cobalt species, Co^{n+}. The second component appears at 782.2 eV and might correspond to another cobalt cation in a higher oxidization state than the previous one, or in another atomic environment. This is compatible with the existence of directly Co_2AlO_4 spinel or with other cobalt spinels and CoO or (Mg,Co)O, according to the XRD results discussed above. As expected, there are no peaks assigned to metallic cobalt, around 777-778 eV.

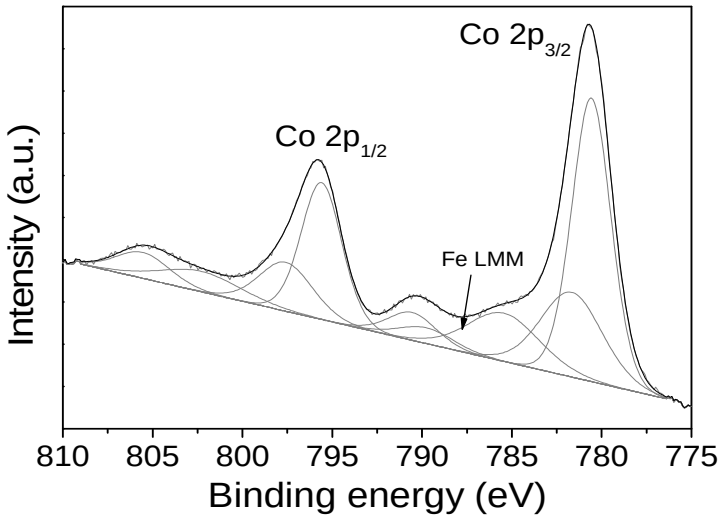

Fig. 4.2 XP spectrum of sample 1K calc, representative of the four samples. Residual STD = 1.03.

Sample	Co:Mg:Al atomic ratio			K/Co atomic ratio
	Co	Mg	Al	
0K calc	1	2.8	5	0
0.5K calc	1	3.8	1.9	0.31
1K calc	1	4.1	2.0	0.72
2K calc	1	4.2	2.4	0.41

Table 4.1 Elemental atomic composition of the surface of the catalysts determined by XPS.

XPS analysis of the surface revealed that the K/Co atomic ratio did not follow the nominal tendency (see Table 4.1). On the contrary, the amount of potassium at the surface followed the series: 0 < 0.5 < 2 < 1, being the experimental atomic percentage of K/Co at the surface: 0, 0.31, 0.41 and 0.72 atomic %, respectively. Also, the surface Co:Mg:Al ratio does not match the molar nominal ratio 1:2:1. Sample 0K_calc has the surface metal ratio closest to the nominal one: 1:2.8:1.5. Interestingly, as the amount of nominal potassium increases, so does the amount of magnesium and aluminium at the surface, with the corresponding decrease of cobalt (Table 4.1). These data indicate that the calcination treatment after potassium impregnation (4 hours at 723 K) favours the segregation of magnesium and aluminium atoms towards the surface of the calcined hydrotalcite. This has been reported in the literature for K-promoted Co-Cu-Zn-Al catalysts for higher alcohol synthesis [17] and could explain why the K/Co ratio at the surface exhibits a volcano shape with a maximum centred on the 1K_calc catalyst.

Thermal programmed desorption of ammonia (TPD-NH_3) was monitored with mass spectrometry (MS) to calculate the concentration of acid sites at the surface of the material. The TPD profiles present three peaks (Figure 4.3). The peak at the lowest temperature, between 433 K and 463 K, corresponds to desorption of ammonia, as evidenced by MS. The second peak is the less intense, between 600 and 700 K, and is

related with water evolution. The third peak, which has the largest area, corresponds to several processes: desorption of ammonia ($M=15^+$ in the mass spectrum), thermal reduction of cobalt with evolution of oxygen ($M=32^+$), evolution of water ($M=18^+,17^+$) and carbon dioxide ($M=44^+$). This third peak occurred between 939 K and 946 K. No hydrogen and nitrogen evolution was detected at any time, suggesting that there is no decomposition of NH_3 into N_2 and H_2. This has been reported to occur in some ruthenium metal centres [18]. Shen *et al*. studied the surface acid/base properties of hydrotalcite derived MgAlO oxides by infrared spectroscopy and identified the presence of Brønsted acid sites (H^+) and Lewis acid sites (Al^{3+}) [19]. Considering this information, the peak at the lowest temperature is assigned to NH_4^+ species formed between NH_3 and surface protons, as Lewis acid sites are stronger than Brønsted sites. The ammonia evolved at high temperature corresponds to the one anchored at the Al^{3+} ions within the Mg-O-Al species [20]. Interestingly, the area of the first peak decreases as the amount of potassium at the surface (the one determined by XPS) increases. In fact, it follows a linear relationship (see Figure 4.4). The amount of acid sites ranges from 0.34 to 0.07 $mmol_{NH3} \cdot g_{sample}^{-1}$. Moreover, the temperature of the most intense peak linearly decreases as the amount of potassium at the surface increases, indicating that not only the number of acid sites decreases, but also their strength (see Figure 4.3). The intensity of the third peak cannot be directly related to the number of Lewis acid sites, since reduction of cobalt and evolution of CO_2 also takes place. But, taking into account the first peak, our aim of reducing the acid strength of the hydrotalcites by doping with potassium was achieved.

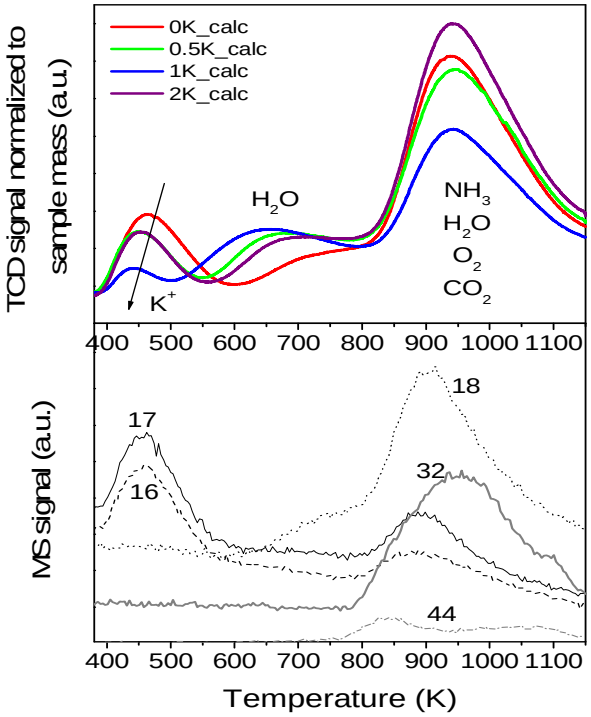

Fig. 4.3 (Above) TPD-NH_3 profiles of calcined samples with annotation of the evolved gases. (Below) Mass spectrum of sample 0K calc, coupled to the TPD-NH_3 experiment. Only masses with significant amount are shown.

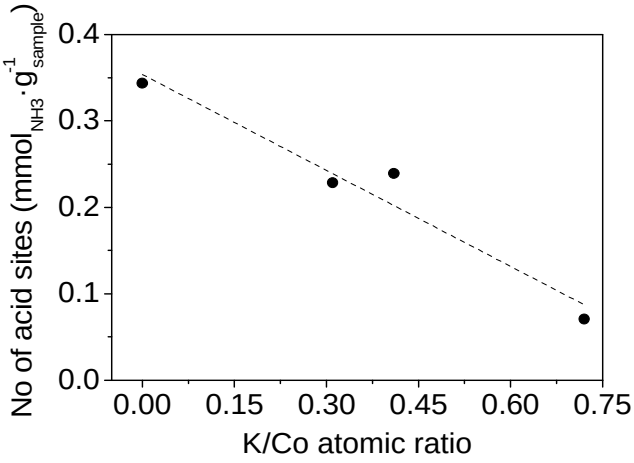

Fig. 4.4 Amount of acid sites corresponding to the peak centred at 450 K in the TPD NH_3 profiles vs. K/Co atomic ratio, determined by XPS.

Thermal programmed reduction (TPR) profiles are similar for the four samples (see Figure 4.5). Each profile shows two peaks. The first one, which corresponds to the

reduction of Co^{3+} to Co^{2+} [10], is centred around 710 K. The second peak appears between 1058 K and 1137 K and corresponds to the total reduction of Co^{2+} to Co^{0} [10]. The temperature of the maximum of the second peak decreases as the nominal amount of potassium increases, indicating that potassium doping favours the reduction of the cobalt (II) ions to metallic cobalt. The consumption of hydrogen corresponding to the second peak is ca. four times higher than that associated with the first peak, as expected from the stoichiometry of cobalt spinel (Co_2AlO_4) and/or a mixture of cobalt in other spinels and CoO.

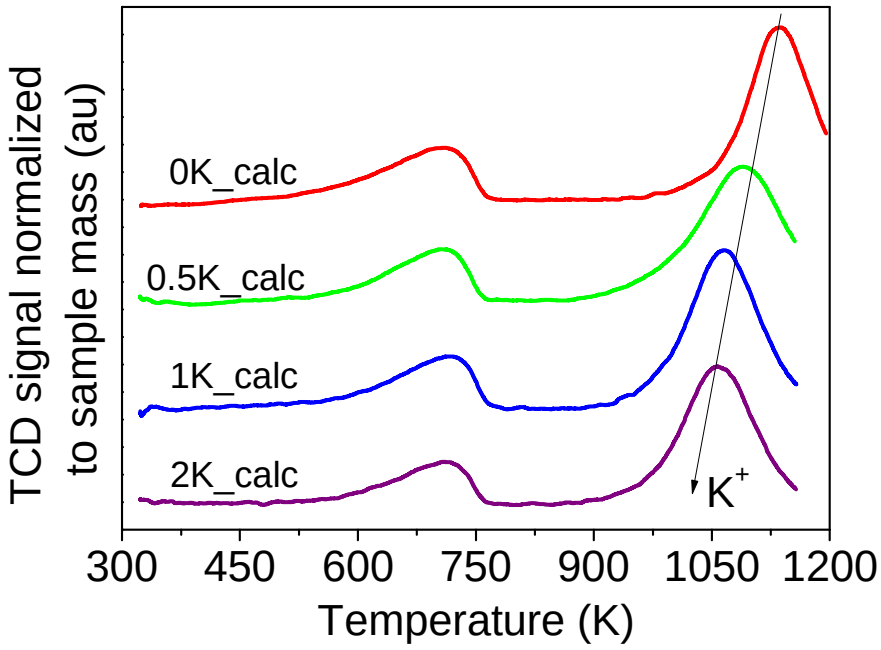

Fig. 4.5 TPR profiles of calcined samples.

Further characterization by magnetometry was performed on samples 0K_calc and 1K_calc, since they bear the lowest and highest amount of potassium at the surface, as determined by XPS. The magnetic behaviour is the one expected for an antiferromagnetic spinel, as it has been previously observed [21] and in accordance to XRD results. The magnetization at room temperature linearly increased with the magnetic field, as it is expected for a paramagnet (see Figure 4.6). At 5 K, the calcined samples behaved slightly superparamagnetic, matching their high magnetic

susceptibility at this temperature, as illustrated in the ZFC-FC curves by the high slope at low temperature. We had previously observed in a set of samples with different Co/Mg/Al molar ratio that the magnetization per gram of cobalt decreased as the amount of cobalt in the hydrotalcite increased, confirming the antiferromagnetic character of the calcined Co/Mg/Al hydrotalcites [10]. ZFC-FC curves appear as superimposed in each sample. The absence of hysteresis excludes the existence of a ferromagnetic phase. Moreover, the absence of inflection points indicates that there is only one magnetic phase, which is assigned to cobalt spinel. Then, and as expected, potassium addition to the hydrotalcites does not alter the magnetic properties of the calcined samples.

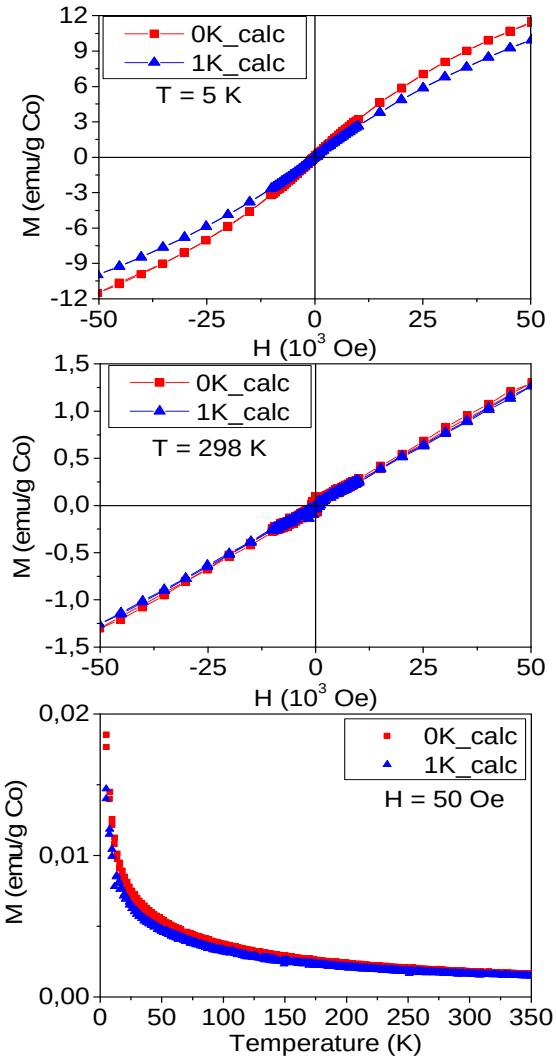

Fig. 4.6 Magnetization curves vs. applied magnetic field (up and center) and vs. temperature (down; H = 50 Oe) of samples 0K calc and 1K calc.

4.3.2. Ethanol steam reforming

Calcined cobalt hydrotalcites, doped with potassium, appear to be active catalysts for the ESR reaction. Monoliths loaded with the same amount of catalyst (150 mg) were tested between 623 K and 823 K with a gaseous H_2O:EtOH molar mixture of 4:1 (steam to carbon, S/C = 2, $8.0 \cdot 10^{-5}$ $g_{EtOH} \cdot min^{-1}$). Each temperature was maintained until the product amount was stabilized after ca. 35 min. Figure 4.7 shows the ethanol conversion vs. temperature for the four samples. Ethanol conversion starts to be detectable just above 600 K and reaches total conversion at 823 K. It should be highlighted that as the amount of potassium at the surface increases (determined by XPS), the ethanol conversion is higher at lower temperatures. Therefore, potassium can be regarded as a promoter of the reaction since it enhances the activity of the catalyst.

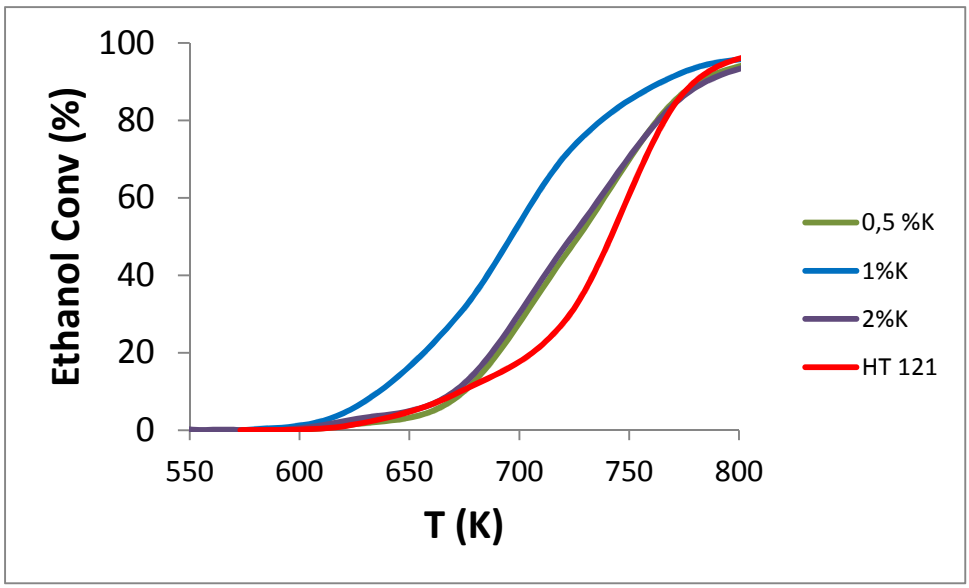

Fig. 4.7 Ethanol conversion vs. temperature; inlet flow $8.0 \cdot 10^{-5}$ g_{EtOH} min^{-1}, S/C = 2.

ESR reaction over cobalt-based catalysts is a complex process that begins with the dehydrogenation of ethanol into acetaldehyde and then follows with the steam reforming of acetaldehyde into hydrogen and a mixture of carbon oxides [7]. The decomposition process of ethanol into methane and carbon monoxide also takes place at high temperature, as well as methanation of carbon oxides. Figure 4.8 collects data of product selectivity vs. temperature of the four samples. Below 723 K, the main products

are H_2, CH_3CHO, acetone (an undesirable by-product formed at the expenses of acetaldehyde) and CO_2. Above 723 K, the H_2 and CO_2 selectivity increases at the expense of acetaldehyde and acetone. Finally, at 773-825 K oxygenates are consumed and the reverse WGS reaction takes place, with a concomitant increase of CO. Methane and ethylene content are kept low under the temperature range tested.

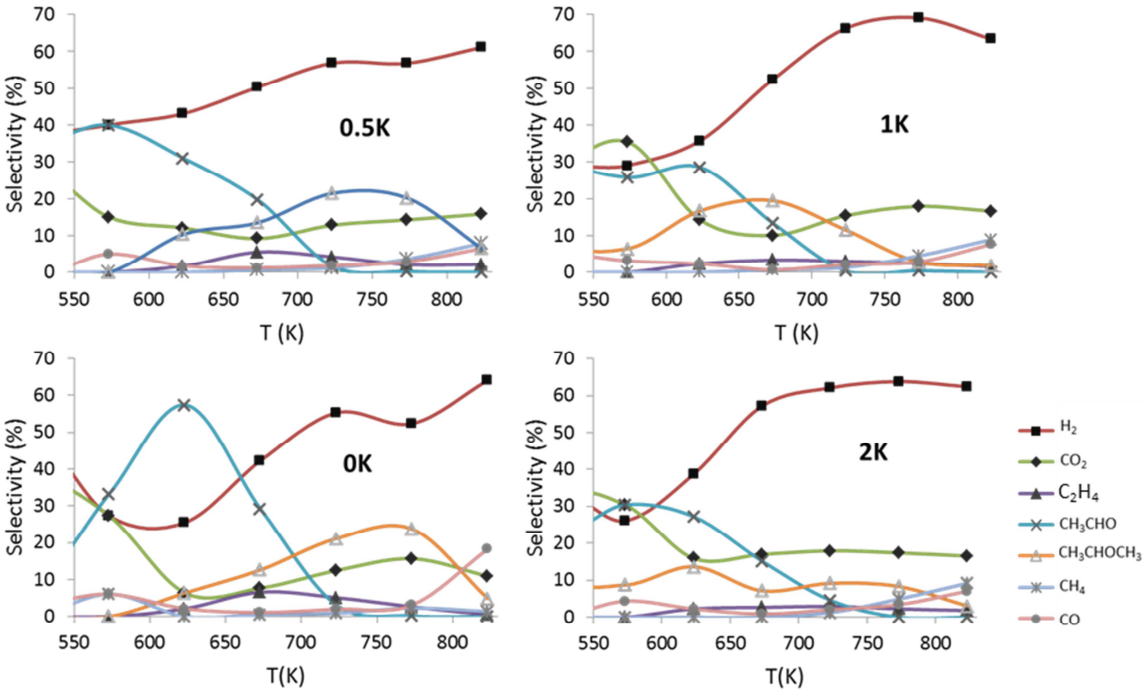

Fig. 4.8 Product selectivity vs. temperature ((■) H_2, (♦) CO_2, (▲) C_2H_4, (**X**) CH_3CHO, (□) CH_3COCH_3, (✱) CH_4 and (●) CO); inlet flow $8.0 \cdot 10^{-5}$ g_{EtOH} min^{-1}, S/C = 2.

As the ethanol conversion vs. temperature is dependent on the amount of potassium, selectivity data at 50% and 100% ethanol conversion have been collected in Figure 4.9, in order to study the influence of potassium on the product selectivity (the reaction temperature at 50% EtOH conversion, as depicted from Figure 4.7 is 740 K, 725 K, 695 K and 722 K for samples 0K to 2K, respectively; the reaction temperature at 100% EtOH conversion is 823 K for the four samples). Hydrogen selectivity increases with potassium addition at 50% EtOH conversion, but it is nearly independent at 100% EtOH conversion. At 50% EtOH conversion, acetaldehyde increases with potassium at the surface (identified by XPS), suggesting that the addition of potassium favours the

dehydrogenation of ethanol. At 100% EtOH conversion there is no CH_3CHO, and acetone also diminishes with higher potassium doping. Ethylene selectivity is independent of potassium content, being lower at higher ethanol conversions. Methane and carbon monoxide selectivity are below 2.5% at 50% EtOH conversion, i.e., potassium does not favour the decomposition of ethanol into CH_4 and CO at this temperature. At 100% EtOH conversion, CH_4 selectivity increases slightly due to the higher reaction temperature (823 K).

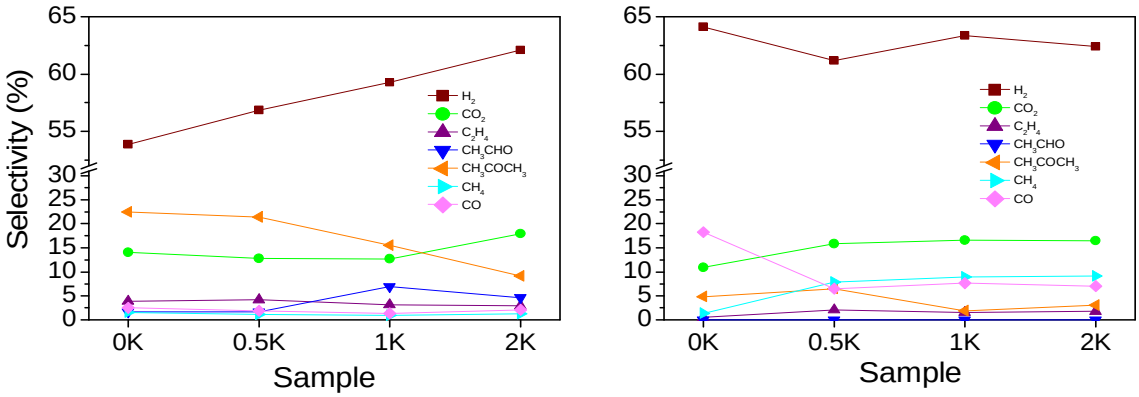

Fig 4.9 Product selectivity at 50% EtOH conversion (left: temperature ranges from 695 K to 740 K) and 100% EtOH conversion (right: T = 823 K).

Stability tests were performed at 823 K during 7 hours, with high load of reactants, 0.018 $g_{EtOH}\cdot min^{-1}$, vaporized before entering the reactor (S/C=2). The four samples were fairly stable during this period of time, reaching 60% of hydrogen selectivity and around 15% of CO_2 content on a dry basis. In order to study in depth how the stability was affected by the addition of potassium, samples 0K and 1K were submitted to severer conditions: 200 h of reaction fed with ethanol, followed by 100 h fed with bioethanol (823 K, 0.036 $g_{EtOH}\cdot min^{-1}$; see Figure 4.10). Bioethanol contains impurities, such as sugars and other compounds derived from the fermentation process, which are more difficult to reform than ethanol. Therefore, deactivation of catalysts is faster when fed with bioethanol [22]. Samples 0K and 1K were stable during the experiment and showed no significant changes of selectivity when fed either with ethanol or bioethanol (Figure 4.10). H_2 selectivity stabilized around 62%, CO_2 around 21%, CO and CH_4 around 5-8%,

and acetaldehyde was only in traces along the experiment. No acetone, neither ethylene, were produced.

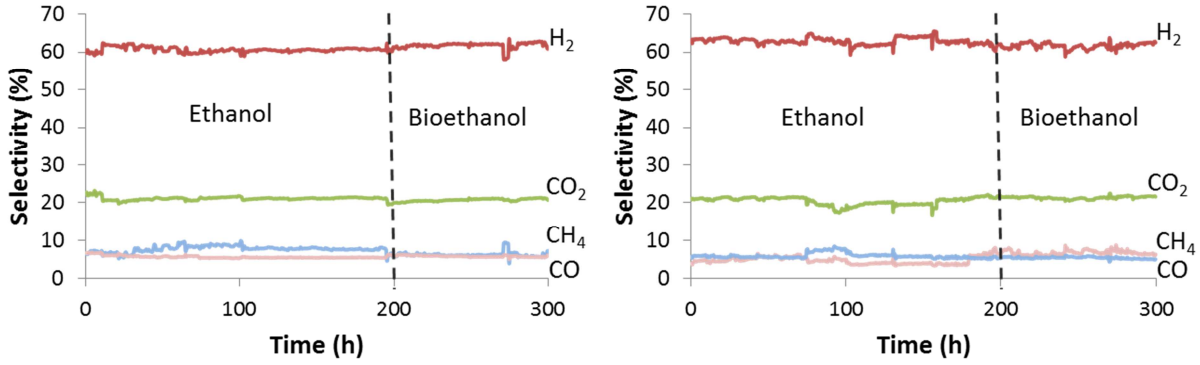

Fig. 4.10 Stability test: product selectivity vs. time at 823 K with 100% EtOH conversion (left: sample 0 K; right: sample 1 K). Inlet flow 0.036 g_{EtOH} min^{-1}, S/C = 2.

The usual lack of stability of cobalt-based catalysts is one of the drawbacks of these materials. Our results are outstanding since our catalysts are stable for at least 200 h under high load of ethanol and a further 100 h under high load of bioethanol, with no signs of deactivation. The disposition of the cobalt atoms within the crystalline structure of the spinel might be determinant for their long-term stability. On the other hand, potassium does not have a significant role in the stability of the catalysts in the time interval studied. The monoliths were weighed before and after the stability tests to monitor the amount of carbon deposited onto the catalysts. Interestingly, no increase of mass was detected in the short-time tests (7 hours) in any of the four samples. TPR coupled to mass spectrometry is also a useful tool for identifying carbon formation. Hydrogen reduces coke to methane between 673 K and 1073 K, which can be quantified by a signal at $M=15^+$ in the mass spectra (the signal $M=15^+$ corresponds to the radical CH_3^+, the most intense when sampling methane). No peak of mass 15^+ was detected in samples 0K_reac and 1K_reac after stability tests (7 h long), thus again indicating that coke formation was negligible. In the long-time tests (300 h), sample 0K generated $13.5 \cdot 10^{-3} g_C \cdot g^{-1}_{catalyst} \cdot h^{-1}$ and sample 1K $6.7 \cdot 10^{-3} g_C \cdot g^{-1}_{catalyst} \cdot h^{-1}$. These data confirm our initial hypothesis that the addition of potassium to cobalt hydrotalcite-derived catalysts might neutralize the acid sites and, in turn, decrease the coke formation. This fact might

favour a better stability in a longer time interval than 300 h, compared to the sample without K.

4.3.3. Samples after ESR

As we observed in our previous work [10], oxidized cobalt species are active for ethanol steam reforming and, in contrast to metallic cobalt, they are less active but do form scarce coke during reaction. This constitutes a big advantage on cobalt-based systems for ESR, since these catalysts deactivate easily due to coke formation, although they work at lower temperatures than other metal-based catalysts and they are remarkably cheaper. Here, we have made an effort on the determination of the oxidation state of cobalt after the reaction.

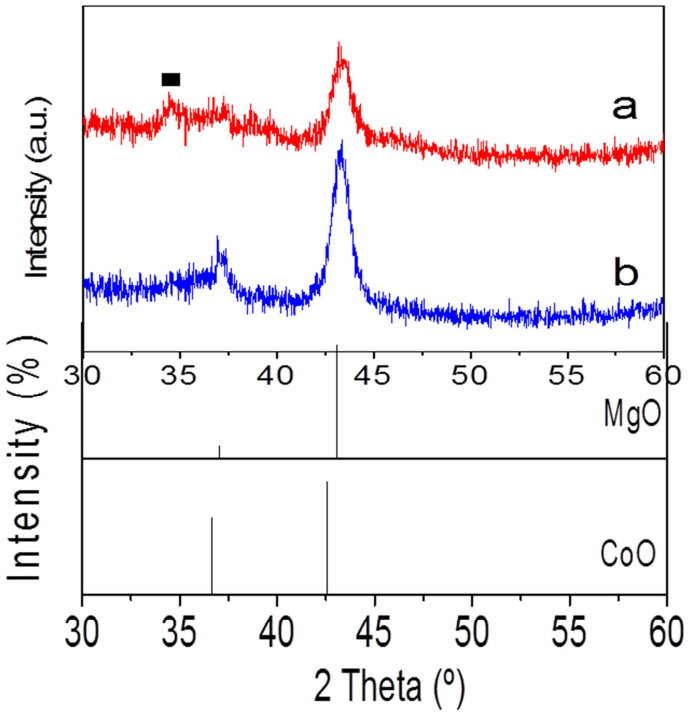

Fig. 4.11 X-ray diffractograms of reacted samples 0K reac (a) and 1K reac (b). (■) Silicon signal from the holder. XRD patterns of several oxide phases are included for comparison.

The reacted samples showed simple XRD profiles, with only two peaks (see Figure 4.11), corresponding to the rock salt type phase, common to MgO and CoO [15, 16] (XRD patterns JCPDS 01-07-1525 and JCPDS 01-075-0533). Any peaks at 47°, 51° neither 53° of 2θ were detected, that would indicate the presence of metallic cobalt. Therefore, the main crystalline phase present in the sample is (Co,Mg)O. Aluminium cations may be highly dispersed in the structure of (Co,Mg)O without the formation of spinel species or, alternatively, be present in an amorphous phase.

XPS analysis shed light on the oxidation state of cobalt atoms at the surface. The spectra of the four samples share the shape and the energy range: there are two main peaks around 781.3 eV and 797.2 eV, which correspond to the $Co2p_{3/2}$ / $Co2p_{1/2}$ spin orbital splitting, and two strong satellites (see spectrum of sample 1K_reac in Figure 4.12, representative of the four samples). The main peaks, as well as the satellites, could be fitted to only one component. The spin orbital splitting is 15.9 eV and the separation between the satellite lines and the photo lines is close to 5 eV, indicating that the present cobalt species is a high spin Co^{2+}, and practically excluding the existence of Co^{3+} ions. We assign these bands to cobalt oxide (Co,Mg)O. Significantly, there are no peaks at 777-778 eV, indicating again the absence of metallic cobalt at the surface of the catalyst. We had already observed the absence of metallic cobalt under ESR reaction conditions with a Co/Mg/Al calcined hydrotalcite in an *in-situ* XPS experiment [10].

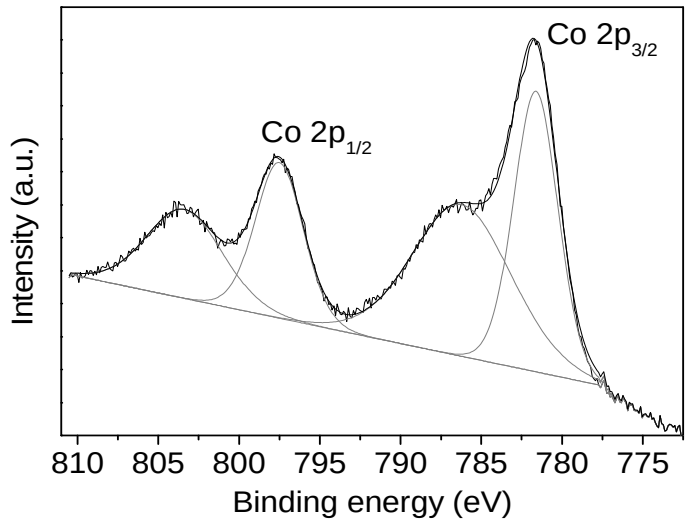

Fig. 4.12 XP spectrum of sample 1K reac, representative of the four reacted samples.

The atomic ratio between carbon and cobalt was compared to the amount of potassium in the sample, before and after reaction. The carbon peak has two components. One is assigned to the presence of carbonate species (around 289 eV) and it is not considered for the current calculation. Only the component around 284 eV, assigned to carbon residues, is considered. The values of the C/Co atomic ratios are listed in Table 4.2. Calcined samples show small C/Co atomic ratio with an average value of 1.4. After reaction, the C/Co atomic ratio increased significantly (one order of magnitude, from 1.1 to 10.8) in sample 0K_reac. On the other hand, the samples doped with potassium do not show such a high C/Co atomic ratio after reaction, reaching values only 4.0 to 5.2. These results indicate, once more, that the presence of potassium in the sample hinders the formation of coke during ethanol steam reforming.

Calcined samples	C/Co (atomic ratio)	Reacted samples	C/Co (atomic ratio)
0K calc	1.1	**0K reac**	10.8
0.5K calc	1.2	**0.5K reac**	5.2
1K calc	0.2	**1K reac**	5.1
2K calc	3.3	**2K reac**	4.0

Table 4.2 Co and C atomic composition at the surface of calcined and reacted samples calculated by XPS.

The magnetic measurements point towards the existence of two magnetic phases after reaction. The main one has a paramagnetic profile, indicated by the linear increase of magnetization at room temperature as the applied magnetic field is intensified. The minor one is related with a slight superparamagnetic shape at 5K, and also by the decrease in magnetization as the temperature increases in the zero field cooled–field cooled experiments (see Figure 4.13). That profile matches with an antiferromagnetic behaviour, for what we assign it to the cobalt oxide phase. The second phase is ferromagnetic, as evidenced by the small hysteresis at low applied magnetic field, both at 5K and at RT. We have assigned this phase to metallic cobalt. Its amount, calculated

as the percentage ratio between the experimental saturation magnetization (5.6 and 6.6 emu/g) and the bulk saturation magnetization (163 emu/g) at room temperature, is only 0.09 wt.% and 0.18 wt.%, for samples 1K_reac and 0K_reac, respectively. It can be argued that the lack of metallic cobalt could be attributed to a reoxidation of the metallic cobalt entities potentially formed during the ESR. However, we had observed in a previous work on cobalt talc nanolayers, that the catalyst after reaction showed clearly ferromagnetic behaviour in the magnetization curves vs. field and vs. temperature. In that case, the sample was kept at normal conditions, indicating that Co^0 entities were stable under these conditions and they were not reoxidized [23].

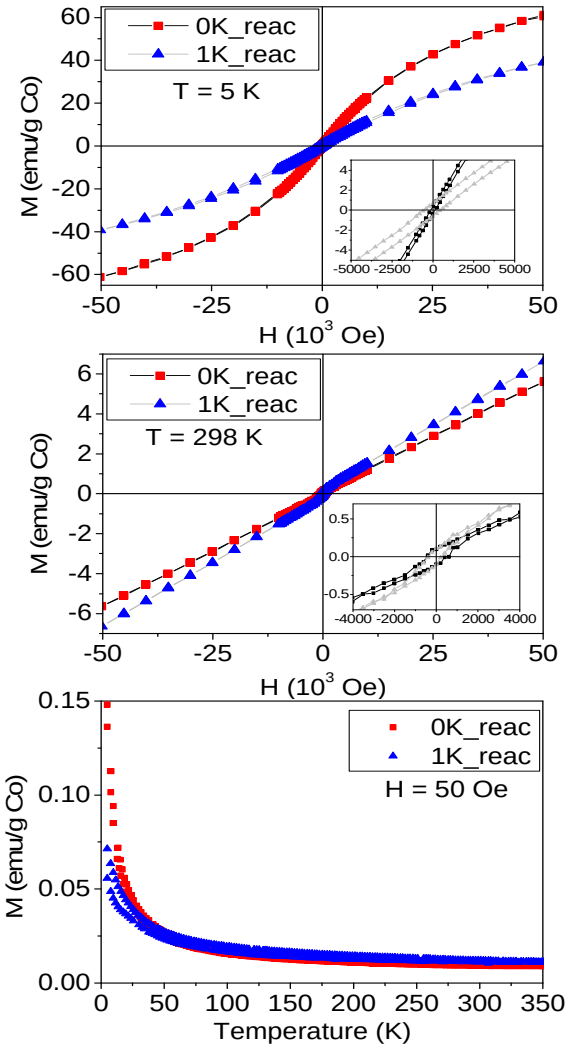

Fig. 4.13 Magnetization curves vs. applied magnetic field (up and centre) and vs. temperature (down, H = 50 Oe) of samples 0K reac and 1K reac.

TPR profiles recorded after ESR reaction show only one peak, centred at 1013 K and 1043 K, for samples 0K_reac and 1K_reac, respectively (see Figure 4.14). These peaks

correspond to the reduction of Co^{2+} to Co^{0}. There is no peak around 700 K, confirming that Co^{3+} species are not present after the reaction, as observed by XRD, XPS and magnetic measurements. This is due to the reduction of Co^{3+} in cobalt spinel by the hydrogen generated during ESR, which was carried out at 823 K (compare the TPR profiles before and after ESR, Figures 5 and 14, respectively). Therefore, only Co^{2+} is present in the sample. The peaks are narrow and well defined, pointing to a homogeneous dispersion of the Co^{2+} species in the material.

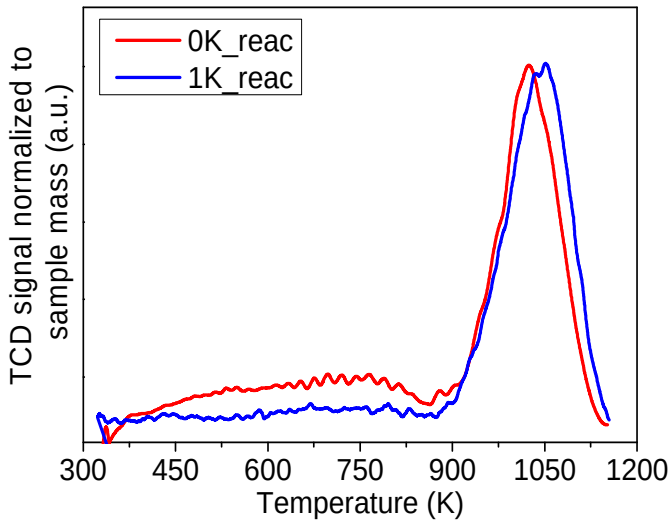

Fig. 4.14 TPR profiles of samples 0K reac and 1K reac.

4.4 Oxidative Steam Reforming (OSR)

Oxidative steam reforming was carried out in the temperature range 723-823 K at atmospheric pressure in a tubular stainless-steel reactor over the as-synthesized honeycombs loaded with the hydrotalcite 1K, without any pretreatment. The reaction was tested with three different oxygen to carbon mixtures of O/C=0.1, 0.2 and 0.3 molar, named 0.1_Ox, 0.2_Ox and 0.3_Ox respectively, the ethanol-water ratio was maintained constant at S/C=3. Figure 4.15 shows product selectivity for ESR and OSR 0.1_Ox at 100 % ethanol conversion.

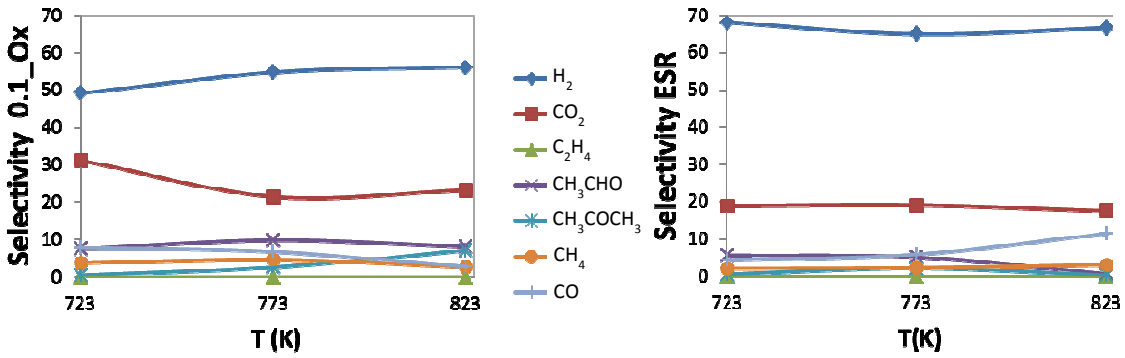

Fig 4.15 ESR and 0.1_Ox OSR selectivity vs Temperature

Hydrogen selectivity is higher for ESR during the whole range of temperature, OSR has lower hydrogen selectivity and acetone starts to raise at 800 K. On the other hand hydrogen selectivity decreases when the amount of oxygen is increased, figure 4.16 shows selectivity for the three O/C molar ratios compared to ESR selectivity. CO_2 and acetaldehyde notably increase when oxygen is added, and acetone is present only in OSR. Figure 4.16 also shows theoretical H_2, ESR shows a H_2 yield close that expected from theoretical H_2. Contrarily OSR results are different than expected; when oxygen is increased the H_2 yield move away from the theoretical value, thus indicating that OSR is not a good choice for Co hydrotalcite-derived catalysis.

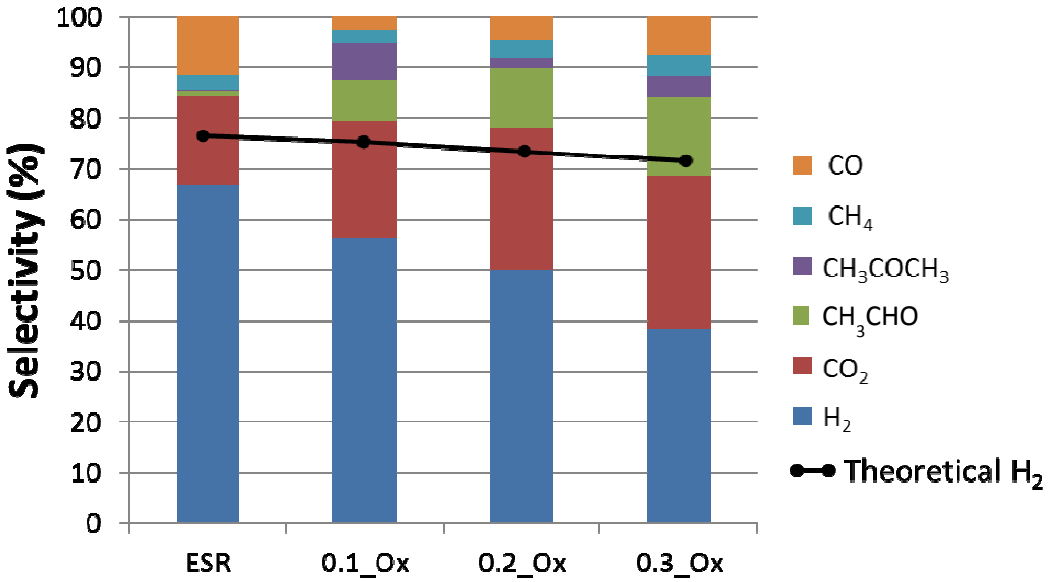

Fig. 4.16 OSR and ESR selectivity at 823 K.

4.5 Conclusions

We have synthesized a new family of robust honeycomb catalysts for bioethanol steam reforming based on calcined Co/Mg/Al hydrotalcites doped with potassium. The addition of potassium to the hydrotalcites reduces the number and strength of acid sites. The catalysts are active for the ESR reaction, where potassium acts as a promoter, being very stable for long-term experiments under high loads of both ethanol and bioethanol and generating scarce amounts of carbon (0.0067 $g_C \cdot g^{-1}_{catalyst} \cdot h^{-1}$). During reaction, cobalt spinel transformed completely into high spin Co^{2+} in cobalt oxide (or in (Co,Mg)O) and only traces of metallic cobalt were identified by magnetometry, <0.1 wt. % Co^0, indicating that oxidized cobalt is an active species in ESR. These catalyst do not perform well under OSR conditions.

4.6 References

[1] H. Idriss, M. Scott, J. Llorca, S. Chan, W. Chiu, P. Sheng, A. Yee, M. Blackford, S. Pas, A. Hill, F. Alamgir, R. Rettew, C. Petersburg, S. Senanayake, M. Barteau, ChemSusChem, 1, (2008), 905-910.

[2] P. Bichon, G. Haugom, H.J. Venvik, A. Holmen, E.A. Blekkan, Topics Catal., 49, (2008), 38-45.

[3] J. Llorca, P.R. de la Piscina, J.A. Dalmon, J. Sales, N. Homs, App. Catal. B: Environ., 43, (2003), 355-369.

[4] J. Llorca, J.A. Dalmon, P.R. de la Piscina, N. Homs, App. Catal. A: General, 243, (2003), 261-269.

[5] J. Llorca, N. Homs, P.R. de la Piscina, J. of Catalysis, 227, (2004), 556-560.

[6] A.M. Karim, Y. Su, M.H. Engelhard, D.L. King, Y. Wang, ACS Catalysis, 1, (2011), 279-286.

[7] A. Casanovas, C. de Leitenburg, A. Trovarelli, J. Llorca, Chem. Engineering Journal, 154, (2009), 267-273.

[8] G. Busca, U. Costantino, T. Montanari, G. Ramis, C. Resini, M. Sisani, Int. J. of Hydrogen Energy, 35, (2010), 5356-5366.

[9] A.M. Karim, Y. Su, J. Sun, C. Yang, J.J. Strohm, D.L. King, Y. Wang, App. Cat. B: Environ., 96, (2010), 441-448.

[10] R. Espinal, E. Taboada, E. Molins, R.J. Chimentao, F. Medina, J. Llorca, RSC Advances, 2, (2012), 2946-2956.

[11] J.F. da Costa-Serra, A. Chica, Int. J. of Hydrogen Energy, 36, (2011), 3862-3869.

[12] F. Cavani, F. Trifiro, A. Vaccari, Cat. Today, 11, (1991), 173-301.

[13] T. Yamanaka, Y. Takeuchi, Zeitschrift Fur Kristallographie, 165, (1983), 65-78.

[14] P.G. Casado, I. Rasines, J. of Solid State Chem., 52, (1984), 187-193.

[15] E. Schiebold, Z. Kristallographie, Kristallgeometrie, Kristallphysik, Kristallchemie, 56, (1921), 430-430.

[16] W.D. Johnston, R.R. Heikes, D. Sestrich, Journal of Physics and Chemistry of Solids, 7, (1958), 1-13.

[17] I. Boz, Cat. Lett., 87, (2003), 187-194.

[18] M. Nagai, K. Koizumi, S. Omi, Cat. Today, 35, (1997), 393-405.

[19] J.Y. Shen, M. Tu, C. Hu, Journal of Solid State Chem., 137, (1998), 295-301.

[20] P. Kustrowski, L. Chmielarz, E. Bozek, M. Sawalha, F. Roessner, Mat. Research Bulletin, 39, (2004), 263-281.

[21] J. Rass-Hansen, R. Johansson, M. Moller, C.H. Christensen, Int. J. of Hydrogen Energy, 33, (2008), 4547-4554.

[22] A.A. Khassin, T.M. Yurieva, V.V. Kaichev, V.I. Bukhtiyarov, A.A. Budneva, E.A. Paukshtis, V.N. Parmon, J. of Molecular Catalysis A: Chemical, 175, (2001), 189-204.

[23] M. Dominguez, E. Taboada, H. Idriss, E. Molins, J. Llorca, J. Mat. Chem., 20, (2010), 4875-4883.

CHAPTER 5

Ethanol steam reforming in a catalytic membrane reactor over cobalt hydrotalcite

"Ethanol steam reforming in a catalytic membrane reactor over cobalt hydrotalcite"

Raúl Espinal, Andres Anzola, Esperanza Adrover, María Roig, Ricardo Chimentao, Francisco Medina, Eduardo López, Daniel Borio, Jordi Llorca.

Summited to:

Catalysis Today

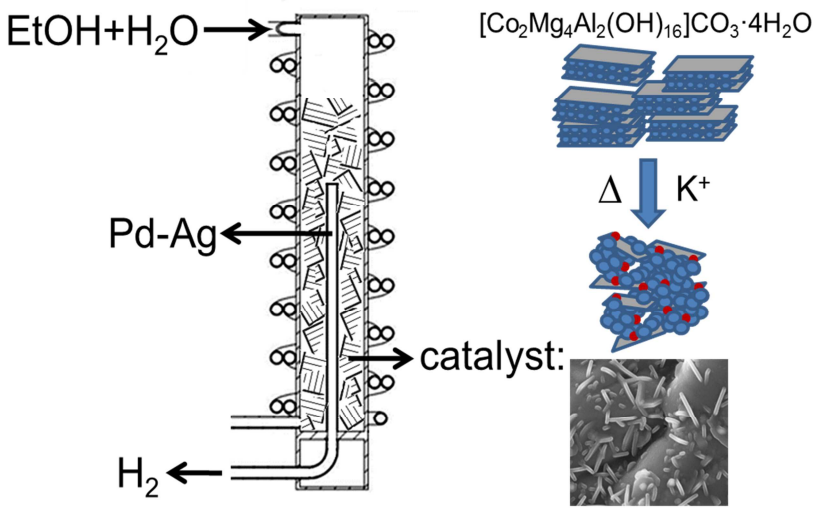

5.1 Introduction

On-site hydrogen generation from various liquid fuels as an alternative to direct hydrogen storage is envisioned as one of the key points for the use of proton exchange membrane fuel cells (PEMFC) for the market of power sources for portable and mobile applications [1,2]. Among liquid fuels that are currently considered, ethanol is advantageous over other conventional substrates because it is readily available, easy to obtain from biomass and to transport, CO_2-neutral and safe to handle [3,4]. In recent years, numerous catalyst formulations have been studied intensively for ethanol steam reforming (ESR) aiming at the generation of hydrogen [5-8]:

$$C_2H_5OH + 3H_2O \leftrightarrows 6H_2 + 2CO_2 \qquad (5.1)$$

An efficient catalyst for hydrogen production from ethanol has to dissociate the C-C bond, maintain a low CO concentration and be stable under catalytic operation. A survey of the literature reveals that noble metal-based catalysts perform well for ESR [9-11]. They are stable and exhibit high activity. However, they are expensive and need high temperatures to be active (923-1023 K). The main reaction mechanism involves the decomposition of ethanol into a mixture of hydrogen, carbon monoxide and methane, followed by the steam reforming of the produced methane. Additionally, the water gas shift reaction balances CO and CO_2 rendering extra hydrogen amounts. Nickel catalysts are inexpensive but under reaction conditions they suffer from sintering and deactivation by carbon deposition.

Cobalt-based catalysts can operate at much lower temperature levels when compared with noble metal-based catalysts, typically at 673-823 K, since they do not yield methane as an intermediate species in the reaction mechanism, which can only be reformed at high temperature [12-43]. Over cobalt-based catalysts, ethanol is first dehydrogenated into a mixture of hydrogen and acetaldehyde (eq. 5.2), and then acetaldehyde reacts with steam to yield mainly hydrogen and carbon oxides (eq. 5.3), which participate in the WGS (eq. 5.4), or decompose into carbon monoxide and methane (eq. 5.5), which in turn undergo steam reforming (eq. 5.6):

$C_2H_5OH \leftrightarrows H_2 + CH_3CHO$ (5.2)

$CH_3CHO + H_2O \leftrightarrows 3\ H_2 + 2\ CO$ (5.3)

$CO + H_2O \leftrightarrows H_2 + CO_2$ (5.4)

$CH_3CHO \leftrightarrows CH_4 + CO$ (5.5)

$CH_4 + H_2O \leftrightarrows 3\ H_2 + CO$ (5.6)

An important advantage of conducting the ESR at lower temperature is that the WGS equilibrium favors the formation of hydrogen and CO_2 at the expense of CO and water (eq. 5.4), thus maximizing the production of H_2 and reducing the volume of the WGS units normally implemented downstream the reformer (or even using a single WGS reactor). The heat transfer management of the fuel processor design is simplified as well. However, in contrast to noble metal-based systems, most cobalt catalysts suffer from severe deactivation during ESR due to extensive carbon deposition, particularly under realistic loads of ethanol. Essential for this matter is the understanding of the role of cobalt oxidation state. Accurate in situ studies have revealed that Co metal particles are formed easily under reaction conditions, which rapidly detach from the catalyst support and originate carbon nanotubes, nanofibers and platelets. At the same time, selectivity to methane and higher hydrocarbons increases at the expense of the reforming products (H_2 and CO_x). Recently, we have reported that catalysts derived from Co/Mg/Al hydrotalcites are active for ESR at 823 K and do not accumulate carbon because no metallic cobalt is formed under reaction conditions [44]. This interesting result allows designing catalysts containing cobalt for ESR without coke deposition (no metallic cobalt) by placing in appropriate environments Co^{2+} active species. Over K^+-doped hydrotalcite-derived cobalt catalysts we have reported stable operation for 300 h under high loads of ethanol and commercial bioethanol [45].

The use of catalytic membrane reactors (CMR), where the generation and separation of hydrogen take place simultaneously, appears as an attractive approach to further simplify on-site/on-demand reformers. In addition, the extraction of hydrogen from the reaction medium that occurs in CMR equipped with H_2-selective membranes leads to an equilibrium shift in the reforming reactions and enables attaining enhanced hydrogen

yields when compared with conventional reactors operating under the same conditions [46]. With respect to a classical configuration consisting of a reactor unit in series with a separation unit, CMR represent a modern configuration in which an integrated reaction/separation unit has many potential advantages: reduced capital costs, improved yields and selectivities and drastically reduced downstream separation costs [47,48].

Among CMRs, palladium-based membrane reactors fulfill the requirements to obtain an ultra-pure hydrogen stream suitable for PEMFC feeding. Via innovative techniques, such as cold-rolling and diffusion welding developed at several laboratories and companies, robust Pd-based thin wall tubes less than 0.05 mm in wall thickness have been produced [49] and their complete hydrogen selectivity and durability have been demonstrated in long term tests [50]. Today, numerous catalytic membrane reactors designs are available for producing high hydrogen throughputs in compact reforming systems [51,52]. In addition, the retentate gas outcoming the membrane reactor can be used as a fuel source for a catalytic combustor to provide a thermally self-sustainable operation [53].

Pd alloy membranes have been used in CMR mainly for WGS and steam reforming reactions of methane and methanol, but their use in the steam reforming of ethanol is relatively new [54-60]. Concerning the use of cobalt-based catalysts for ESR in catalytic membrane reactors, Iulianelli et al. conducted ESR over Co/Al_2O_3 [61,62]. Several operational parameters such as temperature, pressure, sweep-gas flow (SF) and load were evaluated and hydrogen yield and recovery values as high as 60% and 95%, respectively, were reached at 673 K, 3 bar, SF=25.2 (countercurrent flow) and WHSV=0.2 h^{-1}. The same catalyst was tested at 673 K in a porous stainless steel (PSS) supported Pd membrane reactor with the aim of investigating the influence of the membrane characteristics as well as of the reaction pressure from 3 to 8 bar by Basile et al. [63]. Hydrogen recovery of about 50% was reached under complete ethanol conversion. Recently, a Co/Al_2O_3 catalyst has been used in a PSS membrane reactor at 673 and 8-12 bar for simulating bio-ethanol steam reforming by using a mixture of water-ethanol-acetic acid and glycerol with 1:13:0.18:0.04 molar ratio [64]. About 94% of bio-ethanol conversion was obtained at 12 bar and GHSV=800 h^{-1}, with 40% hydrogen yield and 40%

hydrogen recovery. Finally, Domínguez et al. [65] studied the ESR in a CMR over cobalt talc at 598-673 K and 5-15 bar. In addition to an improvement of the hydrogen yield, the CMR showed a rapid response to changes in the ethanol-water mixture load; a constant hydrogen flow was obtained after 2s following variations of ±10%.

Here, we extend our work on hydrotalcite-derived cobalt catalysts by studying their performance in a catalytic membrane reactor equipped with a Pd-Ag membrane to obtain PEM fuel cell-grade hydrogen (1 atm, no sweep gas). Different reactor configurations, temperature (673-873 K), pressure (1-18 bar), ethanol load and steam-to-carbon (S/C=1.8-3) ratios have been tested.

5.2 Experimental

5.2.1. Preparation of catalyst

The Co/Mg/Al hydrotalcite with formula $[Co_2Mg_4Al_2(OH)_{16}]CO_3 \cdot 4H_2O$ was prepared as described elsewhere by co-precipitation from aqueous solutions of $Co(NO_3)_2 \cdot 6H_2O$, $Mg(NO_3)_2 \cdot 6H_2O$ and $Al(NO_3)_3 \cdot 9H_2O$ and 2M NaOH alkaline solution at a constant pH of 10±0.5. The resulting solid was thoroughly washed, dried at 373 K and calcined at 823 K for 12 hours to obtain the hydrotalcite-derived mixed oxide. Potassium addition to the calcined hydrotalcite (1.0 wt. % referred to the nominal cobalt content) was accomplished by impregnation with KOH aqueous solution. The resulting catalyst was dried at 373 K and calcined at 823 K for 4 hours.

The catalyst powder was deposited onto cordierite pieces ($Al_3Mg_2AlSi_5O_{18}$, 400 cells per square inch, Rauschert Company) by washcoating [44,45]. A 5:1 molar mixture of polyvinyl alcohol (PVA) and acetic acid was used as binding agent. The resulting catalytic cordierite pieces were dried at 373 K and calcined at 823 K for 4 hours. The washcoating procedure was repeated until the catalyst loading was ca. 5% with respect to the cordierite support.

5.2.2 Characterization

X-ray diffraction (XRD) patterns were collected between 10 and 90° of 2θ with a step width of 0.02° and a step time of 1 s using a Bruker D8 instrument equipped with Cu Kα incident radiation (λ=1.5404 Å) and a graphite monochromator.

The microstructure, morphology, and composition of the catalyst layer were studied with a Zeiss NEON40 crossbeam scanning electron microscope (SEM) operated at 5 kV and equipped with energy dispersive X-ray analysis (EDX).

Surface characterization was done with X-ray photoelectron spectroscopy (XPS) on a SPECS system equipped with an Al anode XR50 source operating at 150 mW and a Phoibos 150 MCD-9 detector. The pressure in the analysis chamber was below 10^{-7} Pa. The area analyzed was about 2 mm x 2 mm. The pass energy of the hemispherical analyzer was set at 25 eV and the energy step was set at 0.1 eV. Charge stabilization was achieved by using a SPECS Flood Gun FG 15/40. The following sequence of spectra was recorded: survey spectrum, C 1s, Co 2p, Al 2p, Mg 2p and C 1s again to check for charge stability as a function of time and the absence of degradation of the sample during the analyses. Data processing was performed with the CasaXPS program (Casa Software Ltd., UK). The binding energy (BE) values were referred to the C 1s peak at 284.8 eV.

5.2.3 Reaction tests

The functionalized cordierite pieces described above were implemented in a membrane reactor machined in stainless steel measuring 230 mm tall and 22 mm OD (Reb Research & Consulting). A feed evaporation conduit was welded around the reactor. The Pd-Ag membrane (30 m active layer thickness over PSS) was a 76 mm tall, 1/8” diameter, pine-hole free, dead-end tube with a total area of 7.1 cm^2. Two different design configurations were selected for the catalytic membrane reactor as shown in Figure 1. First, the catalytic honeycombs (9 pieces, 1.324 g total catalyst load) were disposed in-series into the reactor followed by the membrane tube, resulting in a staged membrane

reactor (SR) (Figure 5.1a). In the second configuration (Figure 5.1b), a fraction of the same catalytic honeycombs were crushed into small pieces (ca. 0.5 mm) and distributed around the membrane tube, resulting in a membrane reactor (MR) (0.46 g total catalyst load). Occasionally, the membrane outlet was blocked to represent the operation of a conventional fixed bed reactor (CR), i.e., without separation. The liquid feed mixture of ethanol and water was introduced with a Knauer Smartline HPLC pump. The retentate pressure was adjusted by a manually-operated back-pressure regulator. No pressure regulation was implemented on the permeate side (atmospheric pressure). No sweep gas was used, therefore, pure hydrogen was obtained in the permeate stream. The gaseous products of the retentate were analyzed by online gas chromatography (Agilent 3000A MicroGC) using MS 5Å, PlotU and Stabilwax columns, as well as the permeate to verify the selectivity of the membrane separation towards hydrogen. Total volumetric flowrates of both permeate (Bronkhorst EL-FLOW) and dry retentate streams (bubble meter) were measured. By measuring under steady-state conditions and in a precise period of time both the composition and flowrate of the gaseous outlet streams as well as the volume of liquid condensed from the retentate flow we verified the correct closure of the mass balance. Before the reaction, pure gas permeation tests were carried out on the reactor membrane, which showed that the selectivity towards hydrogen was infinite and that both Sievert's and Arrhenius' laws were followed. The apparent activation energy for H_2 permeation was found to be 10.3 $kJ \cdot mol^{-1}$ (±1.5 $kJ \cdot mol^{-1}$ considering the 95% confidence limits), in agreement with values reported through the literature for membranes of similar characteristics [66].

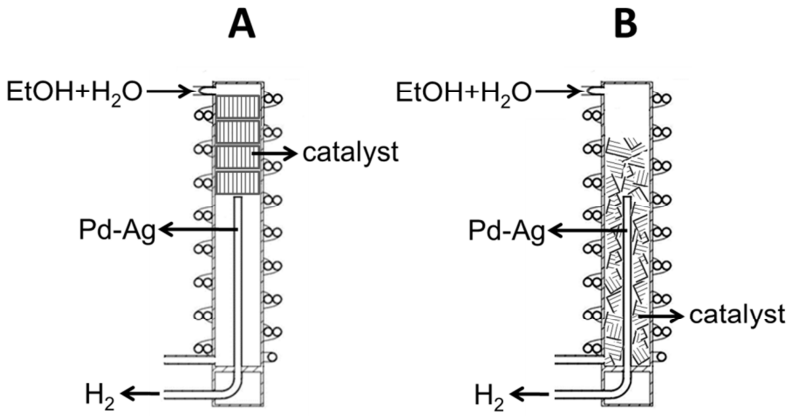

Fig. 5.1 Staged membrane reactor (A) and crushed honeycombs membrane reactor (B).

5.3 Results and discussion

5.3.1 Catalyst characterization

The X-ray diffraction (XRD) profiles of the Co/Mg/Al hydrotalcite and the calcined catalyst doped with potassium (not shown) exhibited the characteristic peaks of the hydrotalcite structure (2θ at ca. 10.8, 22.5, 34.1, 38.4, 45.3, 60.2 and 61.8°) and cobalt spinel (2θ at ca. 18.9, 31.5, 37.0, 44.4, 55.5, 59.2 and 65.0°), respectively, in accordance to previous studies [44,45].

Scanning electron microscopy (SEM) was carried out directly over the cordierite pieces loaded with catalyst as prepared as well as after the ethanol steam reforming tests performed in this study, which accounts for more than 650 h. Figure 5.2a shows a representative SEM image of the fresh catalyst. The sample is comprised mostly by rounded particles of about 20-40 nm in diameter, although several larger platelets are also visible. According to XRD and previous studies [44], the small, rounded particles are ascribed to cobalt spinel, whereas larger particles with platelet morphology likely correspond to mixed oxides coming from hydrotalcite calcination. Figure 5.2b shows a SEM image of the catalyst after ESR for 650 h. Two observations merit to be highlighted; first, the size of spinel particles decrease under ESR conditions, which now measure about 10-20 nm in diameter. Second, the amount of hydrotalcite platelets increases after reaction, which is related to rehydration under steam during ESR conditions, as observed previously [44]. Finally, no carbon deposition has been observed after 650 h of reaction. This is an outstanding result taking into account that low S/C ratios have been selected for approaching real operation (S/C=1.8-3) and also that in a catalytic membrane reactor the partial pressure of hydrogen is lower than that in a conventional reactor due to hydrogen permeation through the membrane.

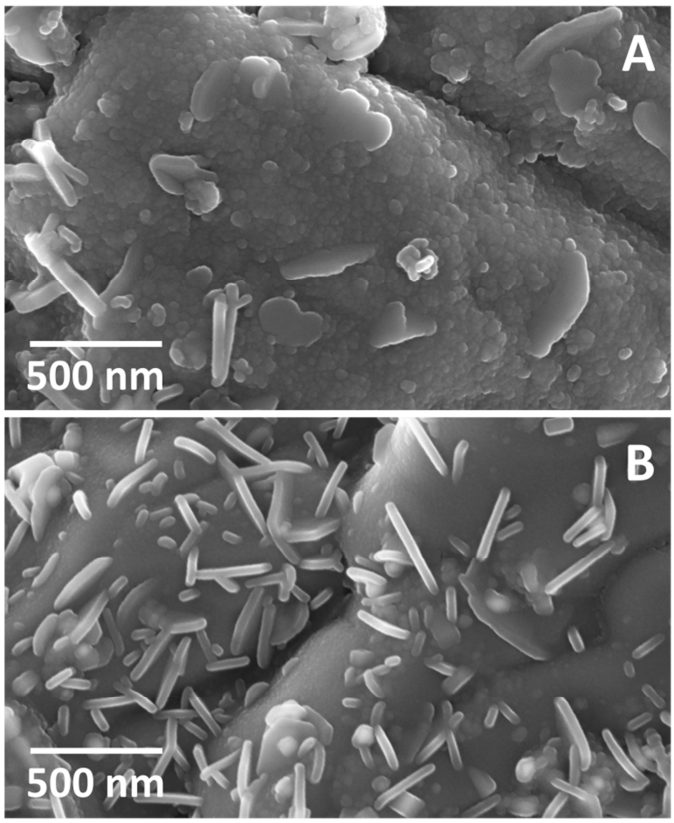

Fig. 5.2 SEM images for fresh catalyst (A) and the catalyst after ESR for 650 h (B).

In order to definitely rule out the presence of carbon deposition onto the catalyst after the ESR tests, we recorded the XP spectra of the surface of both the fresh catalyst and the used one (XPS is a surface sensitive technique and also very sensitive to carbon). The concentration of carbon on the catalysts was virtually identical in both cases (C/Co=0.17 and 0.12, C/(Al+Mg)=0.10 and 0.11 before and after reaction, respectively), thus confirming that no carbon accumulation occurred during ESR operation in the membrane reactor. We have reported previously by in-situ techniques [44] that the absence of metallic cobalt during ESR is responsible for such extraordinary stability. The XPS analysis of the Co 2p region of both the fresh and the used catalysts in our study confirms the absence of metallic cobalt on both of them (Figure 5.3). Bands at 780.0 and 795.5 eV correspond well to the Co $2p_{3/2}$ and Co $2p_{1/2}$ binding energies of Co(II) species, and the satellite lines at 785.3 and 802.1 eV are due to the cobalt hydrotalcite and spinel structures [44]. No bands of metallic Co are visible at about 778 and 793 eV.

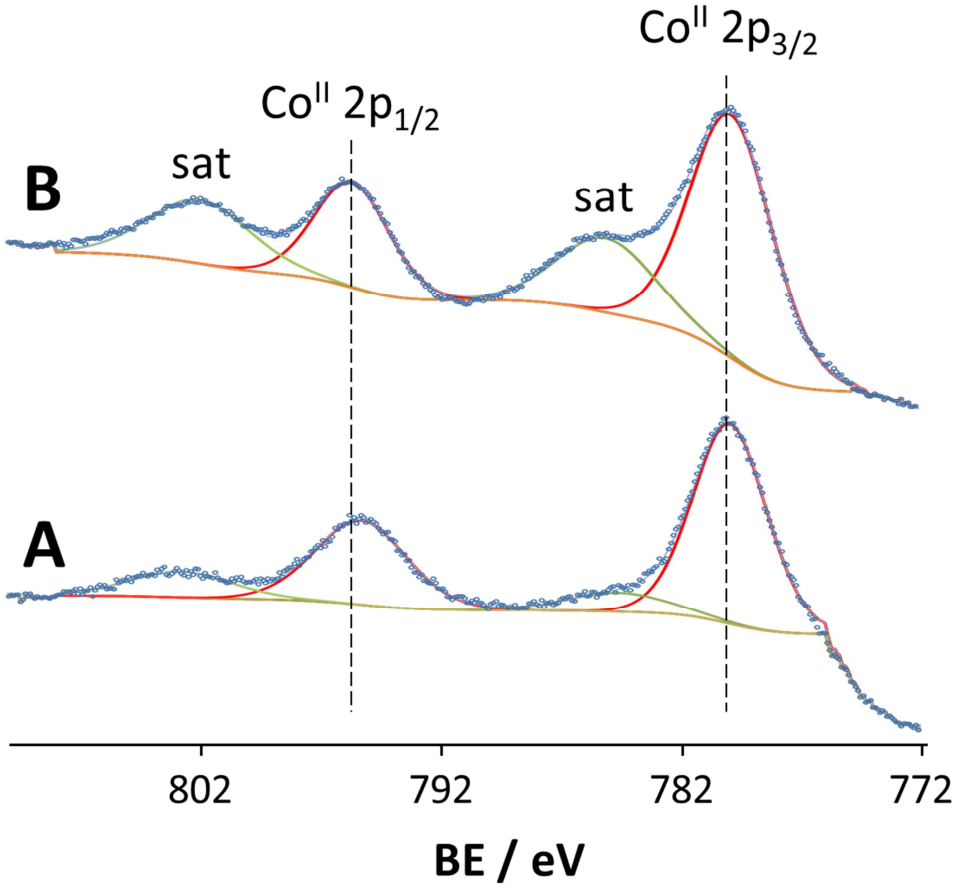

Fig. 5.3 XPS analysis of the Co 2p region of both the fresh (A) and the used catalysts (B).

5.3.2 Staged membrane reactor

As explained in the experimental section, two configurations for the catalyst and the Pd-Ag separation membrane were tested in the same reactor under similar reaction conditions (see Figure 5.1). In all cases, ethanol conversion was complete and the only products detected by gas chromatography were H_2, CH_4, CO and CO_2. No acetaldehyde (the first step in ethanol reforming over Co-based catalysts, equation 5.2), acetone (which is formed via condensation of acetaldehyde) or C_{2+} hydrocarbons were detected. The total amounts of H_2, CO_2, CO and CH_4 obtained in the staged configuration at atmospheric pressure and different reaction conditions were always fairly identical to those obtained previously for catalytic honeycombs loaded with the same catalyst in a fixed bed reactor [45], confirming reproducibility.

The effect of temperature on the distribution of products on a dry basis at 10 bar is shown in Figure 5.4a. The amount of hydrogen increased slightly with temperature at the expense of methane, which is explained in terms of methane steam reforming (equation 5.6). On the other hand, as temperature was increased, the reverse water gas shift reaction was favored and the amount of CO increased progressively at the expense of CO_2, according to the WGS equilibrium (equation 5.4). Pressure had a stronger effect on the distribution of products of the reaction. Figure 5.4b shows the distribution of products on a dry basis obtained at a fixed temperature of 833 K. The selectivity towards methane increased sharply with pressure at the expense of hydrogen, which is explained in terms of the Le Chatelier's principle, since the consumption of moles of H_2 and CO is favored with pressure to yield CH_4 (methanation reaction, see reverse of eq. 5.6).

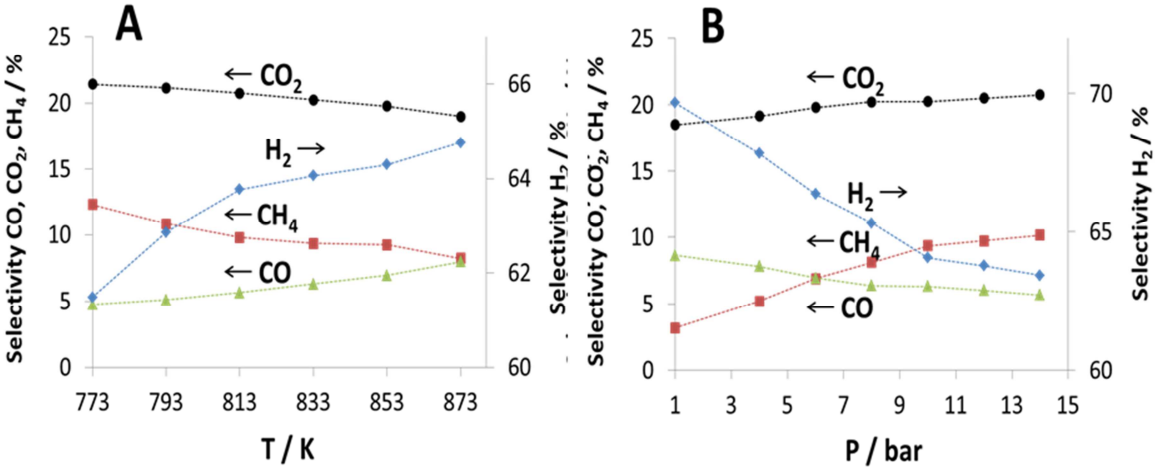

Fig. 5.4 The effect of temperature on the distribution of products on a dry basis at 10 bar (A) and distribution of products on a dry basis obtained at a fixed temperature of 833 K (B).

Figure 5.5 reports the amount of hydrogen permeated as influenced by temperature and pressure in the SR design. As expected, pressure affected strongly the separation of hydrogen at each temperature. The increase of hydrogen flowrate through the membrane is explained in terms of the hydrogen permeation driving force due to the difference in hydrogen pressure at both sides of the membrane, as expected from Sievert's equation. The larger the pressure difference of hydrogen in the retentate and permeate sides, the larger the permeated hydrogen amount per unit membrane area,

this effect clearly dominating up to intermediate pressures (i.e., P<10 bar). However, at higher pressures (10<P<14 bar), the curves of permeated hydrogen tend to attenuate their increments. This is due to the fact that two conflicting effects occurred simultaneously. On the one hand, pressure favored hydrogen permeation through the membrane and, therefore, a higher hydrogen permeating flux. On the other hand, high pressure values resulted in a decrease of the total production of hydrogen ($F_{H2,produced}=F_{H2,retentate}+F_{H2,permeate}$). Thus, as pressure increases, the membrane located downstream the reactor is fed with gaseous mixtures containing lower molar fractions of H_2. This is a direct consequence of the thermodynamics of the reaction since the complete ethanol steam reforming reaction proceeds with a strong increase of the moles number (equation 5.1). The effect of temperature on the permeated hydrogen flowrate is also reported in Figure 5.5. The increase of the operating temperature originates two effects, which both result here in an increase of the total amount of hydrogen permeated. Higher temperatures favor both the total hydrogen production by the reforming reaction and also the permeation through the Pd-Ag membrane as this is a temperature-activated process.

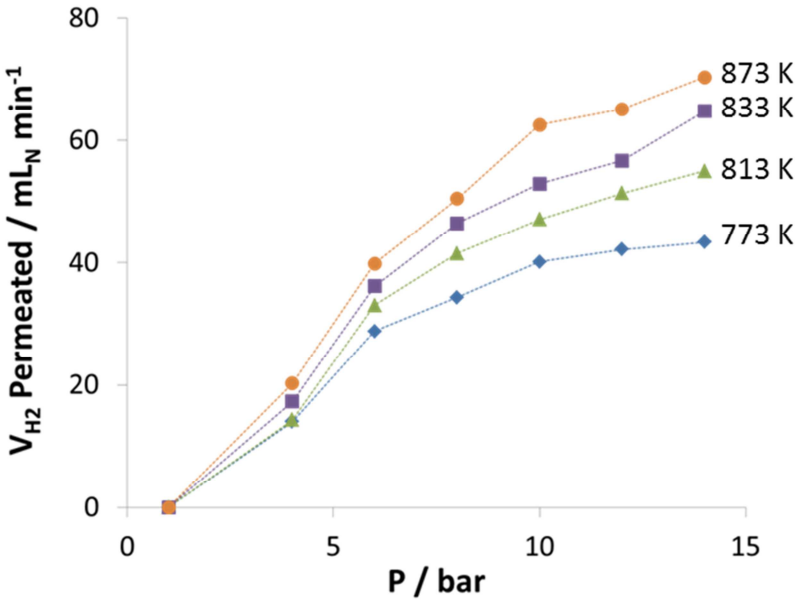

Fig. 5.5 Amount of hydrogen permeated as influenced by temperature and pressure in the SR design

5.3.3. Catalytic membrane reactor

Figure 5.6 shows a comparison of the performance of the two different reactor configurations tested, i.e., SR and MR. Total molar flowrates of produced hydrogen (retentate + permeate) in SR or MR adimensionalized with those obtained without membrane separation (CR) are shown for different pressure values. As expected, the SR configuration showed no influence of the membrane in the production of H_2. Due to the equilibrium shift effect originated by the removal of H_2 through the membrane, a MR configuration proved to be superior, with increases of up to 68% in the H_2 production rate. Higher pressures accentuate the behavior as more hydrogen is permeated.

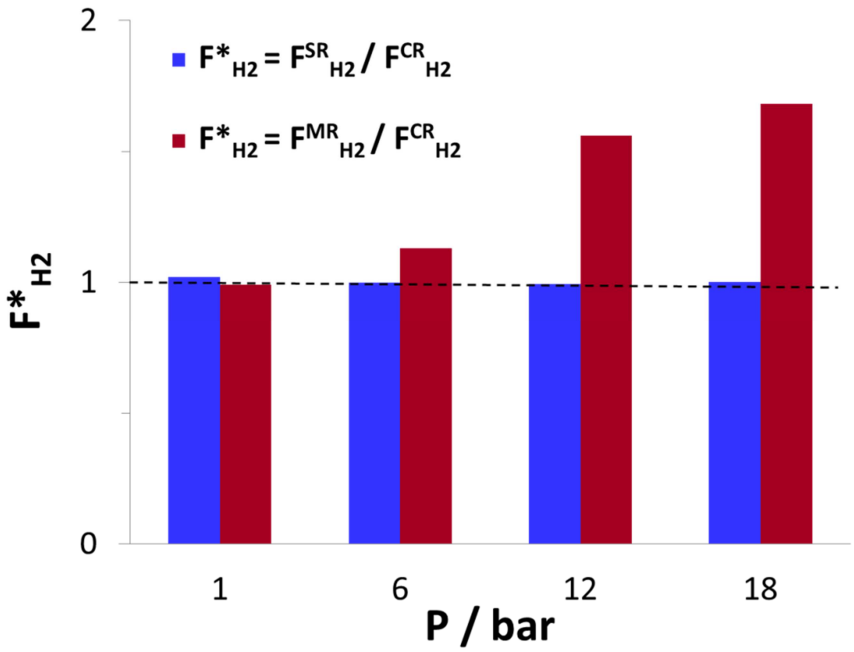

Fig. 5.6 Comparison of the performance of the two different reactor configurations tested, SR and MR.

The influence of pressure and temperature on hydrogen recovery, defined as the amount of hydrogen permeated divided by the total amount of hydrogen produced, is reported in Figure 5.7 for a MR configuration. As expected, hydrogen recovery increases with pressure due to a higher permeation driving force. As permeation is a temperature activated process, recovery is also enhanced at increasing temperature. High hydrogen recovery values of about 80% were achieved in the operating conditions of Figure 5.7.

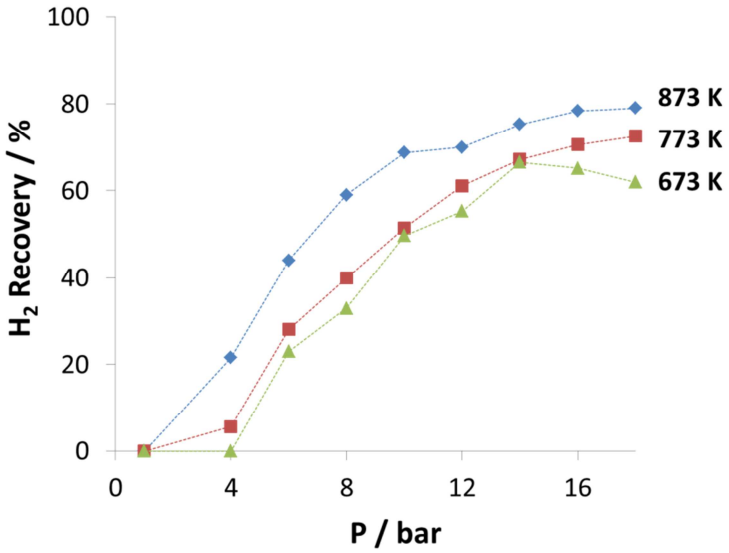

Fig 5.7 Influence of pressure and temperature on hydrogen recovery for MR configuration.

Studies regarding ethanol steam reforming over cobalt hydrotalcites have been reported in a previous work by our group [44,45]. There, it was found that temperatures in the range 773-873 K are optimum for catalytic performance. Figure 5.8a shows a comparison of H_2 yield and hydrogen recovery at these two extreme temperatures for the MR and SR designs and maintaining a fixed value of the load per unit catalyst mass of Q_{liq}/W_{cat} =2.3 ml·g^{-1}·h^{-1} for both configurations (constant contact time based on the catalyst). For both design configurations, an increase of the hydrogen yield with temperature is observed as a result of the equilibrium shift of the endothermic reforming reaction. Moreover, for the MR design the increase in H_2 yield when temperature is increased from 773 to 873 K is higher than the one observed for the SR configuration due to the equilibrium shift effect as hydrogen is permeated through the membrane, operating in the MR in parallel with the reaction. For T=873 K, it should be noted in Figure 5.8a a remarkable value of 5.1 for the hydrogen yield, which means ca. 85% with respect to the maximum stoichiometrically possible of 6 (see equation 5.1). Regarding hydrogen recovery, an enhancement of this variable with temperature is observed for both designs due to both the activation of the membrane and the higher amounts of hydrogen produced by the reaction. Recoveries in the MR design are higher than those corresponding to the SR due to both superior H_2 yields and lower loads selected to compensate a lower catalyst mass in the MR configuration, which

determines a lower total flux per unit membrane area. Remarkable hydrogen recovery values up to 86% of the total amount of hydrogen generated are reported in Figure 5.8a.

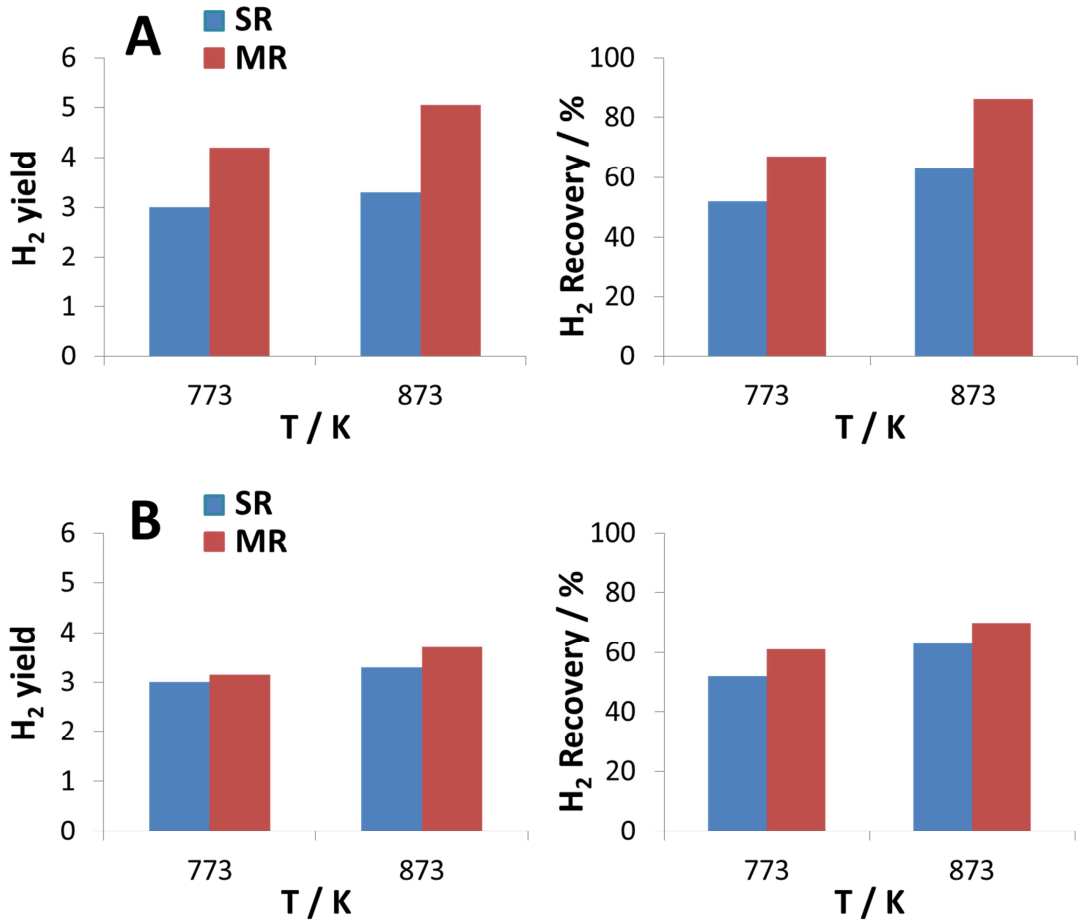

Fig. 5.8 Comparison of H_2 yield and hydrogen recovery at these two extreme temperatures for the MR and SR designs (A) and similar comparison based on a constant feed load per unit membrane area of Q_{liq}/A_{memb}=0.42 ml·cm^{-2}·h^{-1}

Figure 5.8b presents a similar comparison of the performance of both designs (i.e., H_2 yield and recovery vs. T) based on a constant feed load per unit membrane area of Q_{liq}/A_{memb}=0.42 ml·cm^{-2}·h^{-1}. Similar effects than those already discussed above are obtained, that is, an enhancement of hydrogen yield and recovery at increasing temperature due to membrane and reaction kinetic activation. Besides, the effect of the improvement in total hydrogen generation due to the equilibrium shift as hydrogen is permeated from the reaction medium is also easily observed. However, the quantitative differences between performances of MR and SR designs are more moderated on this comparison basis. Since the MR configuration is loaded with a lower catalyst mass, the

diminished contact time (feed flow per unit catalyst mass) affects negatively the hydrogen generation. Nevertheless, this adverse effect is overcompensated by the hydrogen permeation effect. In these terms, the MR design is capable to attain superior performance parameters than the SR even operating with ca. 1/3 the catalyst load.

Finally, the effect of the S/C was tested at 823 K for the MR configuration at a constant space velocity of 6.5 $ml_{liq} \cdot g^{-1} \cdot h^{-1}$ (Figure 5.9). As the S/C ratio increases, the hydrogen yield also increases as higher amounts of water shift the equilibrium to render extra hydrogen, as expected from equations 5.3, 5.4 and 5.6. However, the increase of the S/C ratio also dilutes the system with excess water. This leads to a decrease of the driving force for the permeation through the membrane, which is reflected in the slight drop of the H_2 recovery reported in Figure 5.9. Extrapolation of the S/C values beyond the ones presented in this Figure are expected adverse for the performance, as values nearer to S/C=1.5 are dictated by stoichiometry and S/C values higher than 3 would not apparently improve the reaction performance but for sure would considerably deteriorate the hydrogen separation due to an excessive dilution.

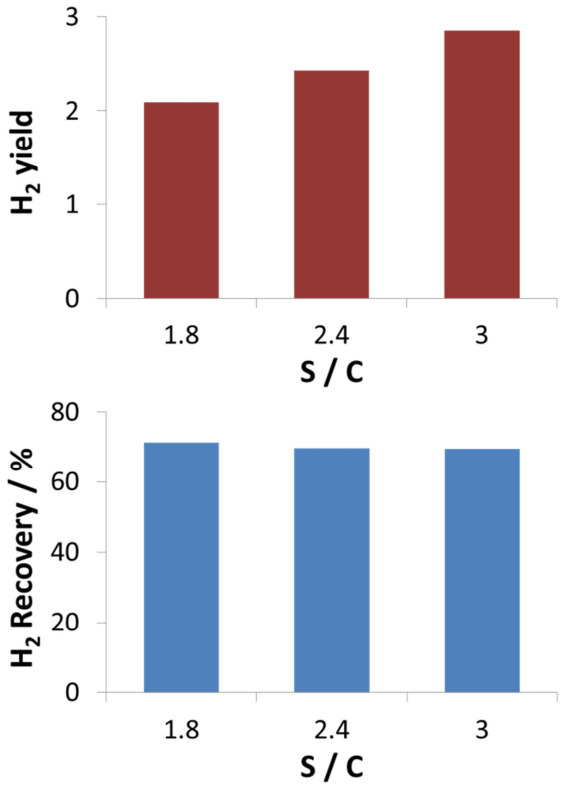

Fig. 5.9 S/C tested at 823 K for the MR configuration at a constant space velocity of 6.5 $ml_{liq} \cdot g^{-1} \cdot h^{-1}$

5.4 Conclusions

Cobalt hydrotalcite $[Co_2Mg_4Al_2(OH)_{16}]CO_3 \cdot 4H_2O$-derived catalyst doped with potassium was supported over cordierite pieces and placed inside a membrane reactor with a single, dead-end Pd-Ag membrane in two configurations. In one configuration, the catalyst pieces were placed in-series with the membrane, forming a staged membrane reactor. In the second configuration, the same catalyst was packed around the membrane, leading to a catalytic membrane reactor. Ethanol steam reforming was carried out in both design configurations at different temperatures, pressures, feed loads and steam-to-carbon values. No sweep gas was used, therefore, pure hydrogen was obtained in the permeate stream, which was maintained at atmospheric pressure. The catalytic membrane reactor configuration showed higher hydrogen yields and hydrogen recoveries than the staged design as resulting from the equilibrium displacement due to the hydrogen removal from the reaction medium. At the conditions tested, the retentate pressure showed a stronger influence on hydrogen yield and recovery than the operating temperature. At 12 bar, 873 K and S/C=3, 3.7 STP $L_{H2,permeate} \cdot mL_{EtOH,liquid}^{-1} \cdot g_{cat}^{-1}$ were measured for the catalytic membrane reactor, ca. three times higher than the values observed for the staged membrane reactor. The cobalt hydrotalcite-derived catalyst used in the reactor, in both design configurations, exhibited a very stable operation and no carbon accumulation occurred under operation for 650 h, as deduced from SEM and XPS analysis.

5.5 References

[1] G. Kolb, Fuel Processing for Fuel Cells; Wiley-VCH: Weinheim, 2008, 1-434.

[2] J. Llorca, in Handbook of sustainable energy, ed. W. H. Lee and V. G. Cho, Nova Publishers, 22, (2010), 693-699..

[3] M. Murdoch, G.I.N. Waterhouse, M.A. Nadeem, J.B. Metson, M.A. Keane, R.F. Howe, J. Llorca, H. Idriss, Nature Chem., 3, (2011), 489-492.

[4] J. Llorca, Contributions to Science, 7, (2011), 57-64.

[5] P.D. Vaidya, A.E. Rodrigues, Chem. Eng. Journal, 117, (2006), 39-44.

[6] A. Haryanto, S. Fernando, N. Murali, S. Adhikari, Energy F., 19, (2005), 2098-2106.

[7] M. Ni, Y.C. Leung, M.K.H. Leung, Int. J. of Hydrogen Energy, 32, (2007), 3238-3247.

[8] J. Llorca, V. Cortés, N.J. Divins, R. Olivera, E. Taboada, Hydrogen from Bioethanol. Renewable Hydrogen Technologies. Ed. L.M. Gandía, G. Arzamendi and P.M. Diéguez. Elsevier, 7, (2013), 135-169.

[9] G.A. Deluga, J.R. Salge, L.D. Schmidt, X.E. Verykios, Science 303, (2004), 993-997.

[10] F. Frusteri, S. Freni, J. of Power Sources, 173, (2007), 200-209.

[11] H. Idriss, M. Scott, J. Llorca, S.C. Chan, W.Chiu, P.Y. Sheng, A. Yee, M.A. Blackford, S.J. Pas, A.J. Hill, F.M. Alamgir, R. Rettew, C. Petersburg, S. Senanayake, M.A. Barteau, ChemSusChem, 1, (2008), 905-910.

[12] F. Haga, T. Nakajima, H. Miya, S. Mishima, Cat. Lett., 48, (1997), 223-227.

[13] J. Llorca, N. Homs, J. Sales, P. Ramírez de la Piscina, J. of Catalysis, 209, (2002), 306-317.

[14] J. Llorca, P. Ramírez de la Piscina, J.A. Dalmon, J. Sales, N. Homs, App. Cat.: B, 43, (2003), 355-369.

[15] J. Llorca, J.A. Dalmon, P. Ramírez de la Piscina, N. Homs, App. Cat.: A, 243, (2003), 261-269.

[16] S. Freni, S. Cavallaro, N. Mondello, L. Spadaro, F. Frustreri, Cat. Commun., 4, (2003), 259-268.

[17] F. Mariño, G. Baronetti, M. Jobbagy, M. Laborde, App. Cat.: A, 238, (2003), 41-54.

[18] J. Llorca, N. Homs, J. Sales, J.L.G. Fierro, P. Ramírez de la Piscina, J. of Catalysis, 222, (2004), 470-480.

[19] J. Llorca, P. Ramírez de la Piscina, J.A. Dalmon, N. Homs, Chem. Mat., 16, (2004), 3573-3578.

[20] J. Llorca, N. Homs, P. Ramírez de la Piscina, J. of Catalysis, 227, (2004), 556-560.

[21] M.S. Batista, R.K.S. Santos, E.M. Assaf, J.M. Assaf, E.A. Ticianelli, J. of Power Sources, 134, (2004), 27-32.

[22] A. Kaddouri, C. Mazzocchia, Cat. Commun., 5, (2004), 339-345.

[23] H. Song, L. Zhang, R.B. Watson, D. Braden, U. Ozkan, Cat. Today, 129, (2007), 346-354.

[24] J.A. Torres, J. Llorca, A. Casanovas, M. Domínguez, J. Salvadó, D. Montané, J. of Power Sources, 169, (2007), 158-166.

[25] M. Benito, R. Padilla, L. Rodríguez, J.L. Sanz, L. Daza, J. of Power Sources, 169, (2007), 167-176.

[26] S. Tutti, F. Pepe, Cat. Lett., 122, (2008), 196-203.

[27] H. Song, U. Ozkan, J. of Catalysis, 261, (2009), 66-74.

[28] A. Casanovas, C, de Leitenburg, A. Trovarelli, J. Llorca, Cat. Today, 138, (2008), 187-192.

[29] A. Casanovas, M. Saint-Gerons, F. Griffon, J. Llorca, Int. J. of Hydrogen Energy, 33, (2008), 1827-1833.

[30] J. Llorca, A. Casanovas, T. Trifonov, A. Rodríguez, R. Alcubilla, J. of Catalysis, 255, (2008), 228-233.

[31] H. Wang, J.L. Ye, Y. Liu, Y.D. Li, Y.N. Qin, Cat. Today, 129, (2007), 305-312.

[32] J. Sun, X-P. Qiu, F. Wu, W-T. Zhu, Int. J. of Hydrogen Energy, 30, (2005), 437-445.

[33] A.E. Galetti, M.F. Gomez, L.A. Arrua, A.J. Marchi, M.C. Abello, Cat. Commun., 9, (2008), 1201-1208.

[34] J.C. Vargas, S. Libs, A.C. Roger, A. Kiennemann, Cat. Today, 107, (2005), 417-425.

[35] A. Casanovas, M. Domínguez, C. Ledesma, E. López, J. Llorca, Cat. Today, 143, (2009), 32-37.

[36] R. Nedyalkova, A. Casanovas, J. Llorca, D. Montané, Int. J. of Hydrogen Energy, 34, (2009), 2591-2599.

[37] A. Casanovas, C. de Leitenburg, A. Trovarelli, J. Llorca, Chem. Eng. J., 154, (2009), 267-273.

[38] E. López, A. Irigoyen, T. Trifonov, A. Rodríguez, J. Llorca, Int. J. of Hydrogen Energy, 35, (2010), 3472-3479.

[39] A. Casanovas, M. Roig, C. de Leitenburg, A. Trovarelli, J. Llorca, Int. J. of Hydrogen Energy, 35, (2010), 7690-7698.

[40] P. Bichon, G. Haugom, H.J. Venvik, A. Colmen, E.A. Blekkan, Topics in Catal., 49, (2008), 38-45.

[41] M. Domínguez, E. Taboada, E. Molins, J. Llorca, Cat. Today, 138, (2008), 193-197.

[42]M. Domínguez, G. Cristiano, E. López, J. Llorca, Chem. Eng. J., 138, (2011), 176-177

[43] M. Domínguez, E. Taboada, H. Idriss, E. Molins, J. Llorca, J. Mat. Chem., 20, (2010), 4875-4883.

[44] R. Espinal, E. Taboada, E. Molins, R.J. Chimentao, F. Medina, J. Llorca, RSC Advances, 2, (2012), 2946-2956.

[45] R. Espinal, E. Taboada, E. Molins, R.J. Chimentao, F. Medina, J. Llorca, App. Cat. B: Environ., 127, (2012), 59-67.

[46] F. Gallucci, A. Basile, Int. J. of Hydrogen Energy, 33, (2008), 1671-1687.

[47] A. Basile, Topics in Cat., 51, (2008), 107-112.

[48] D. Mendes, S. Tosti, F. Borgognoni, A. Mendes, L.M. Madeira, Cat. Today, 156, (2010), 107-117.

[49] S. Tosti, L. Bettinali, J. Mat. Science, 39, (2004), 3041-3046.

[50] S. Tosti, A. Basile, F. Bettinali, F. Borgognoni, F. Chiaravalloti, F. Gallucci, J. of Membrane Science, 284, (2006), 393-397.

[51] S. Tosti, A. Basile, L. Bettinali, F. Borgognoni, F. Gallucci, C. Rizzello, Int. J. of Hydrogen Energy, 33, (2008), 5098-5105.

[52] G.S. Burkhanov, N.B. Gorina, N.B. Kolchugina, N.R. Roshan, Plat. Metals Review, 55, (2011), 3-12.

[53] D. Montané, E. Bolshak, S. Abelló, Chem. Eng. J., 175, (2011), 519-533.

[54] F. Gallucci, A. Basile, S. Tosti, A. Iulianelli, E. Drioli, Int. J. of Hydrogen Energy, 32, (2007), 1201-1210.

[55] S. Tosti, A. Basile, F. Borgognoni, V. Capaldo, S. Cordiner, S. Di Cave, F. Gallucci, C. Rizzello, A. Santucci, E. Traversa, J. Mem. Science, 308, (2008), 50-257.

[56] S. Tosti, A. Basile, F. Borgognoni, V. Capaldo, S. Cordiner, S. Di Cave, F. Gallucci, C. Rizzello, A. Santucci, E. Traversa, J. Mem. Science, 308, (2008), 258-263.

[57] S. Tosti, A. Basile, R. Borelli, F. Borgognoni, S. Castelli, M. Fabbricino, F. Gallucci, C. Licusati, Int. J. of Hydrogen Energy, 34, (2009), 4747-4754.

[58] S. Tosti, M. Fabbricino, A. Moriani, G. Agatiello, C. Scudieri, F. Borgognoni, A. Santucci, J. Mem. Science, 377, (2011), 65-74.

[59] D. Papadias, D. Lee, H.D. Sheldon, M. Ferrandon, S. Ahmed, Int. J. of Hydrogen Energy, 35, (2010), 2004-2012.

[60] E. López, N.J. Divins, J. Llorca, Cat. Today, 193, (2012), 145-150.

[61] A. Iulianelli, A. Basile, International Journal of Hydrogen Energy, 2010, 35, 3170-3177.

[62] A. Iulianelli, S. Liguori, T. Longo, S. Tosti, P. Pinacci, A. Basile, Int. J. of Hydrogen Energy, 35, (2010), 3159-3164.

[63] A. Basile, P. Pinacci, A. Iulianelli, M. Broglia, F. Drago, S. Liguori, T. Longo, V. Calabrò, Int. J. of Hydrogen Energy, 36, (2011), 2029-2037.

[64] P.K. Seelam, S. Liguori, A. Iulianelli, P. Pinacci, V. Calabrà, M. Huuhtanen, R. Keiski, V. Piemonte, S. Tosti, M. de Falco, A. Basile, Cat. Today, 193, (2012), 42-48.

[65] M. Domínguez, E. Taboada, E. Molins, J. Llorca, Cat. Today, 193, (2012), 101-106.

[66] R. Sanz, J.A. Calles, D. Alique, L. Furones, S. Ordóñez, P. Marín, P. Corengia, E. Fernandez, Int. J. of Hydrogen Energy, 36, (2011), 15783-15793.

CHAPTER 6

General conclusions

Hydrogen production from bioethanol using cobalt hydrotalcites

6.1 General conclusions

- Cobalt-based catalysts derived from Co/Mg/Al hydrotalcites are highly active and selective towards hydrogen (69.5 % on a dry basis) at moderate temperature (773 K) for ethanol steam reforming (ESR). The catalyst derived from Co/Mg/Al=1/2/1 (molar) hydrotalcite shows the best catalytic performance.
- A detailed characterization of the catalyst with several physico-chemical techniques has evidenced that the catalyst derived from Co/Mg/Al=1/2/1 hydrotalcite contains CoAl spinel particles as well as CoO strongly interacting with MgO. However, CoAl spinel prepared separately and mixed with MgO is less active and stable for ESR than the hydrotalcite-derived material.
- Unlike previously reported cobalt catalysts for ESR, no metallic cobalt has been detected in our material under ESR with in situ experiments (XPS). Therefore, adequate cobalt-based catalysts for ethanol steam reforming can be designed by placing in appropriate environments Co^{2+} active species.
- Hydrotalcite-derived cobalt catalysts promoted with noble metals Pt and Rh are very active for ethanol steam reforming at moderate temperature. However, metallic cobalt nanoparticles of about 10-15 nm in size evolve under reaction conditions because Pt and Rh strongly promote the reduction of cobalt by spillover of H_2 generated during the reaction.
- These metallic cobalt nanoparticles cause a rapid accumulation of carbon (carbon nanotubes) on the catalyst surface, rendering a practical application unviable.
- Cobalt catalysts derived from Co/Mg/Al hydrotalcites doped with potassium have less number and strength of acid sites, being very stable for long-term experiments under high loads of both ethanol and commercial bioethanol and generating scarce amounts of carbon (0.0067 $g_C \cdot g^{-1}_{catalyst} \cdot h^{-1}$).
- Catalysts derived from Co/Mg/Al hydrotalcites do not perform well under oxidative steam reforming (OSR) conditions.
- Catalytic membrane reactors show higher hydrogen yields and hydrogen recoveries than conventional reactors or staged designs with reactors and separation membranes placed in series. This is due to equilibrium displacement

due to the hydrogen removal from the reaction medium through the membrane. By using Pd-Ag metallic membranes a pure stream of H_2 is obtained, which can be directly used to feed a low-temperature fuel cell. Stable operation with no deactivation and no carbon accumulation has been demonstrated in a catalytic membrane reactor for 650 h.